



THE HONG KONG
POLYTECHNIC UNIVERSITY

香港理工大學

Pao Yue-kong Library

包玉剛圖書館

Copyright Undertaking

This thesis is protected by copyright, with all rights reserved.

By reading and using the thesis, the reader understands and agrees to the following terms:

1. The reader will abide by the rules and legal ordinances governing copyright regarding the use of the thesis.
2. The reader will use the thesis for the purpose of research or private study only and not for distribution or further reproduction or any other purpose.
3. The reader agrees to indemnify and hold the University harmless from and against any loss, damage, cost, liability or expenses arising from copyright infringement or unauthorized usage.

IMPORTANT

If you have reasons to believe that any materials in this thesis are deemed not suitable to be distributed in this form, or a copyright owner having difficulty with the material being included in our database, please contact lbsys@polyu.edu.hk providing details. The Library will look into your claim and consider taking remedial action upon receipt of the written requests.

**OXYGEN AND HYDROGEN SENSING EFFECTS OF
SUPERSONIC CLUSTER BEAM DEPOSITED ZINC OXIDE
FILMS**

LAU KA SENG

MPhil

The Hong Kong Polytechnic University

2019

The Hong Kong Polytechnic University

Department of Applied Physics

**OXYGEN AND HYDROGEN SENSING EFFECTS OF
SUPERSONIC CLUSTER BEAM DEPOSITED ZINC OXIDE
FILMS**

LAU KA SENG

**A thesis submitted in partial fulfilment of the
requirements for the Degree of master of Philosophy**

July 2018

Certificate of originality

I hereby declare that this thesis is my own work and that, to the best of my knowledge and belief, it reproduces no material previously published or written nor material which has been accepted for the award of any other degree or diploma, except where due acknowledgement has been made in the text.

_____ (Signature)

LAU KA SENG (Name of candidate)



Abstract

This project was carried out for investigating the gas sensing properties of nanocluster-assembled highly porous zinc oxide (ZnO) films prepared using the Supersonic Cluster Beam Deposition (SCBD) technique. The study has two main parts. They are focused on investigating the oxygen (O₂) and hydrogen (H₂) sensing properties of the material and the devices made of it.

For thin film fabrication, SCBD method is a physical vapor deposition (PVD) technique which is quite distinctive from many other PVD techniques. An SCBD process starts from generating micro-plasma pulses on the surface of a metal rod target. The target is placed in a discharge chamber at reduced pressure. Atoms ablated from the metal target re-condense to form nanoclusters. The nanoclusters are concurrently carried by an argon gas flow to move towards the exit of the discharge chamber. The gas is extracted from the exit to enter an expansion chamber, where the gas experiences an expansion. Streamlines are formed and collimated with a set of aerodynamic lenses. The nanoclusters in the streamlines are forced to concentrate close to the axis of the gas flow. They finally enter a deposition chamber pumped to reach a high vacuum condition. In this chamber, the nanoclusters are deposited on a substrate to form a coating. Due to the low kinetic energy of the nanoclusters, the impact on the substrate is so light that the structural features of the nanoclusters are retained and diffusion of atoms does not happen. This facilitates the formation of a nanocluster-assembled highly porous coating on the substrate. Furthermore, the clusters size could be controlled with some techniques, and the film



thickness can be adjusted according to the deposition time. For producing an oxide film, some amount of oxygen gas can be mixed into the carrier gas. Post-oxidation process at elevated temperature is often required to improve the crystallization of the nanoclusters and the linkage among them, and also to enrich the oxygen content in the deposits.

In the first part of the study for investigating the oxygen sensing properties of SCBD ZnO-based sensors, all the tests were conducted at ambient temperature. The measurement was done in a way that a film sensor was first put to be stabilized in an environment containing a certain amount of oxygen content. A light source was then turned on to generate above-bandgap photons to illuminate the sensor. The real-time change of the electrical resistance of the sensor was monitored over a specific duration of time. The light source was then turned off and the real-time resistance was continued to be recorded. The time dependence of the current collected throughout the process was analyzed and correlated to the oxygen concentration in the detected region.

Moreover, measurements based on different combinations of sensor structure and the condition of detected region were employed. The purposes are to reveal the influences of the sensor structure on the sensor output, and to assess the applicability of the measurement schemes in environments close to actual circumstances. The combinations covered in the study include:

- (i) flow of dry inert gas like argon (Ar) or nitrogen (N₂) containing a certain amount of detected gas, namely oxygen (O₂) in the study;



- (ii) flow of dry inert gas containing O_2 with the film sensor covered with a water-proof superhydrophobic polymer coating, made of a commercial spray cylinder product called NeverWet (Rust-Oleum).
- (iii) above 90%-humidity O_2 -containing gaseous environment detected with the polymer-coated film sensor,
- (iv) in water containing a broad range of dissolved oxygen detected using a sensor made of the polymer-coated ZnO film with the light source and all electrical parts enclosed in a cavity.

Results of measurements show that in all cases the sensors can generate detectable signals at room temperature if the sensors are illuminated with photons of energy above the bandgap of zinc oxide. The sensor response drops with increasing oxygen content in the detected region. Addition of a polymer coating on the film surface reduces the sensor response. The best post-oxidation condition for obtaining the best compromise between sensing properties and stability is found. The real-time dependence of the light-induced current response exhibit rather systematic trends associated with the change of oxygen concentration. It can be correlated with the oxygen concentration in the detected region in accordance with the magnitude of the sensor response, response time and recovery time.

A model was proposed to give more fundamental interpretation of the observed trends. The model is based on photo-assisted electrical effect, redox reactions among oxygen, detected gas species and the ZnO film. The model incorporates the contributions from photo generation and recombination of electron-hole pairs,



surface sorption of oxygen species, trapping and release of conduction electrons through interaction with the surface sorbed oxygen species, and transport via the defect states in the porous oxide material structure. The study associated with the measurements in water may lead to further develop of an immersion-type dissolved oxygen sensor. A practical method for quantitative determination of oxygen concentration based on the fitting parameters to the real-time resistive response and expected asymptote was proposed and tested, instead of going through long-time measurement to reach real equilibrium.

In the second part of the study for investigating the H₂ sensing properties of SCBD ZnO film sensors, the as-deposited ns-ZnO film is composed of nanoclusters of an average diameter ~5 nm embedded in an amorphous matrix. The post-oxidation condition leading to optimum gas sensing properties was determined to be 500°C for 1 h. With this condition, the nanocluster size increases to 13 nm. They are loosely connected to give a high porosity of 73%. To specify this extraordinary high porosity and roughness, we name the material as ZnO “nanosponge (ns-ZnO)”. Furthermore, the ns-ZnO film was decorated with a palladium (Pd) coating to enhance the capability of catalytic dissociation of hydrogen so as to enhance the sensor response to the gas [58]. The overall sensor structure is thereby denoted as Pd/ns-ZnO.

Measurements of resistive response of the Pd/ns-ZnO film sensor versus H₂ concentration contained in an inert carrier gas like Ar or N₂ was carried out at two different temperatures, namely 20°C and 80°C, respectively. For each temperature, the sample was also set to be under or without UV illumination.



The effect of operation temperature can be illustrated using an example. For 2% H₂ in the sample gas, the sensor response and response time detected at 20°C are 82 and 1 s, respectively. On the other hand, at a higher operation of 80°C, the sensor response increases by 43 times, whereas the response and recovery times are considerably shortened to 0.3 s and 18 s. A moderate operation like 80°C is thereby preferred to use, because the sensor behaves better, and less moisture can stay on the film surface such that the change in surrounding humidity affects much less on the sensor's output. Also, the temperature is low to prevent from significant post-annealing effect leading to instability material structure and subsequent drift of the gas sensing signal.

Compared with published data, the H₂ sensing properties of our sensors are superior to most others made of metal oxide nanomaterials operating at temperatures > 200°C in terms of showing higher sensor response and shorter response time. The effect of applying UV illumination is to improve the stability of the output in cyclic tests.

A theoretical model based on the mechanisms introduced in the previous model for O₂ sensing was used to interpret the H₂ sensing properties in a more fundamental manner. The influences of increasing the operation temperature and UV illumination are discussed.



Publication list

Journal Articles:

1. Wong M.H., Ng N.H., Zhao M., Lau K.S., Man H.C., Cheung J.T. and Ong C.W., "Room-temperature polymer-coated supersonic cluster beam deposited ZnO film for O₂ gas and dissolved O₂ sensing", *Sensor Actuat. B-Chem.* **251**, 1068 (2017).
2. Lau K.S., Ng N.H., Wong M.H. and Ong C.W., "Thermal stability and structure of magnetron sputtered SnSe₂ films annealed in O₂ and Ar", European Materials Research Society, Strasburg, spring 2018, France.



Acknowledgements

I would like to express my sincere gratitude towards my chief supervisor, Dr C.W. Ong, for his inspiration, suggestions, and guidance in various aspects of the project, and for his tireless and unfailing support and encouragement throughout my MPhil programme.

My gratitude also goes to Mr. Wong Man Hon and Mr. Ng Ngai Hang, members of our research group, for stimulating discussion, sharing experiences, and assistance. I am also indebted to Dr Hardy Lui for his support in laboratory management.

I would like to acknowledge the support from the infrastructure of the Hong Kong Polytechnic University, especially from the Department of Applied Physics.

Last but not least, special thanks are due to my girlfriend, who encourages and supports me to pursue a higher degree.



Table of content

Abstract	i
Publication list	vi
Acknowledgements	vii
Table of content.....	viii
List of figure captions	xiii
List of table captions	xviii
Chapter 1 Introduction.....	1
1.1 Background on oxygen sensing research	1
1.2 Background on hydrogen sensing research	2
1.3 Motivation of the present project.....	3
1.3.1 Inspiration from the operating temperature of conventional semiconductor-based gas sensors.....	3
1.3.2 Expected improvements associated with the use of UV light assist	5
1.3.3 Expected improvement associated with the use of highly porous oxide sensor materials	6
1.4 Aims and objectives of the present project	7
Chapter 2 Background of Gas Sensors Technology.....	9
2.1 Performance indexes of a gas sensor	9
2.2 Review of O ₂ gas sensors	12



The Hong Kong Polytechnic University

2.2.1	Metal oxide semiconductor (MO _x) O ₂ gas sensors.....	12
2.2.2	Non-dispersive infra-red (NDIR) O ₂ gas sensors.....	13
2.3	Review of dissolved oxygen sensors	15
2.3.1	Optical dissolved oxygen sensors.....	16
2.3.2	Polarographic dissolved Oxygen Sensors (electrochemical).....	17
2.3.3	Galvanic dissolved oxygen sensors (electrochemical)	18
2.4	Review of popular H ₂ gas sensors	20
2.4.1	Pd-based resistive-type H ₂ gas sensor	20
2.4.2	MO _x type H ₂ gas sensor.....	22
2.4.3	Electrochemical-type H ₂ gas sensor.....	23
2.4.4	Catalytic combustion-type H ₂ gas sensor.....	23
2.4.5	Thermal conductivity-type H ₂ sensor.....	24
2.5	Detailed description of the working principle of MO _x sensors.....	29
2.6	Recent attempts for improving MO _x gas sensors and related phenomena	32
2.6.1	Use of nanomaterials --- grain size effect	33
2.6.2	Use of photo assist with photons of above-bandgap energy ...	33
2.6.3	Photoconductivity phenomenon	34
2.7	Defect induced persistent photoconductivity phenomenon.....	38
Chapter 3	Experimental methods.....	40
3.1	Fabrication of highly porous nanoclustered ZnO films	40
3.1.1	Supersonic Cluster Beam Deposition (SCBD)	40
3.1.2	Post annealing.....	45



3.1.3	Substrate material selection and cleaning procedure	46
3.2	Structure and composition analyses	47
3.2.1	Raman spectroscopy	47
3.2.2	X-ray diffractometry (XRD)	47
3.2.3	Scanning electron microscopy (SEM) and Transmission electron microscopy (TEM) analyses	47
3.3	O ₂ gas sensing properties measurements.....	48
3.3.1	General description of the system	48
3.3.2	Two operation modes for gas sensing measurements.....	51
3.3.3	The gas sensor performance indexes to be examined	53
3.4	Dissolved oxygen sensing properties measurements	55
3.4.1	General description of the system	55
3.4.2	Adjustment of dissolved oxygen content in water	56
3.5	Measurements of O ₂ gas and dissolved oxygen sensing properties ..	57
3.6	H ₂ gas sensing properties measurements	61
Chapter 4	Results and Discussions for Oxygen Gas and Dissolved Oxygen Detection	63
4.1	Structural characterization of SCBD ZnO films	63
4.1.1	SEM images and estimation of porosity.....	63
4.1.2	XRD diffraction and crystallization	66
4.1.3	Raman scattering analysis	68
4.1.4	Cross section structure of TEM	69
4.2	Selection of optimum post-oxidizing condition for making O ₂ sensors	



	71
4.2.1	Dark electrical conductivity of SCBD ZnO films post-oxidized at different temperatures..... 71
4.2.2	UV-assisted electrical conductivity of SCBD films post-oxidized at different temperatures..... 73
4.2.3	Determination of optimum post-oxidation temperature based on stability tests 79
4.3	Oxygen sensing effect of uncoated 500°C-post-oxidized SCBD ZnO films in dry gaseous environment..... 81
4.4	Oxygen sensing effect of polymer-coated 500°C-post-oxidized SCBD ZnO films in dry gaseous environment 84
4.5	Oxygen gas sensing effect of polymer-coated 500°C-post-oxidized SCBD ZnO films in humid gaseous environment..... 88
4.6	Dissolved oxygen sensing properties of the sensors made of polymer-coated 500°C-post-oxidized SCBD ZnO films..... 91
4.7	Modeling of oxygen concentration dependence of photo assisted electrical conductivity of SCBD ZnO films and its potential applications 96
Chapter 5	Results and Discussions for H ₂ Gas Detection.....101
5.1	About the palladium-coated SCBD ZnO films for the study of H ₂ sensing 101
5.2	Basic features of H ₂ sensing properties of Pd-coated ns-ZnO films. 101
5.3	Influence of relative humidity on the H ₂ sensing properties of Pd-coated ns-ZnO films..... 104



5.4	H ₂ concentration dependence of the sensor response.....	107
5.5	Effect of using UV assist on H ₂ sensing properties.....	108
5.6	Comparison of H ₂ sensing properties of our sensors with the published results	113
5.7	Modelling of H ₂ sensing process for MO _x -based gas sensor	115
Chapter 6	Conclusions.....	119
6.1	Summary of findings	119
6.2	Further work.....	123
6.2.1	Mechanism of gas adsorption to photoconductivity	123
6.2.2	Effect of defects in MO _x materials on photo assisted gas sensing response	124
6.2.3	Influence of material selection.....	125
6.2.4	Effect of excitation source in photo-assisted gas sensing performance.....	125
6.2.5	Design of new gas sensors	126
References	128



List of figure captions

Figure 2.1 Cross-section of an optical dissolved oxygen sensor. [91]	16
Figure 2.2 Cross-section of a polarographic dissolved oxygen sensor [91]	18
Figure 2.3 Cross-section of a galvanic dissolved oxygen sensor. [91]	19
Figure 2.4 Gas sensing process realized by a semiconductor-type gas sensor.	30
Figure 2.5 Illustration describing a redox reaction in a reducing gas or an oxidizing gas.	31
Figure 2.6 Physical principle of gas sensing effect of a polycrystalline oxide semiconductor.....	32
Figure 2.7 Schematic diagram of electron transition in a direct band gap semiconductor.....	35
Figure 2.8 a Tauc plot of $(hv)^{1/2}$ against hv . The extrapolation of the linear part of the curve cut the hv -axis at a point which is good estimate of the bandgap energy E_g of a disordered semiconductor.	36
Figure 2.9 The influence of photo generated electron-hole pairs on adsorption- detachment of oxygen.	38
Figure 3.1 Schematic diagram of the configuration of a Supersonic Cluster Beam Deposition (SCBD) system.	42
Figure 3.2 Bombardment of the target by accelerated Ar ions	44
Figure 3.3 AFM image of nanocluster SCBD Zn film prepared at a discharge voltage of -800V.....	44
Figure 3.4 Schematic diagram of the configuration of the furnace used for post-	



	annealing process.....	46
Figure 3.5	Schematic diagram showing the system used for measuring the gas sensing properties of our samples [69].....	50
Figure 3.6	Structure of the measurement chamber used for investigating the dissolved oxygen sensing properties of the samples.	56
Figure 3.7	The structure of the immersion dissolved oxygen sensor prototype made of a 500°C post-oxidized SCBD ZnO film.....	60
Figure 4.1	SEM images of (a) an as-deposited SCBD Zn metal film and (b) the same film after post-oxidized at 500°C for 30 min. The surface roughness is 15.0 nm and 13.6 nm for the two cases.....	65
Figure 4.2	XRD spectra of the as-deposited SCBD ZnO film and the film after post-oxidized at 450, 500, 550 and 600°C.	67
Figure 4.3	Raman spectra of quartz, as-deposited SCBD ZnO film and the film after post-oxidized at 450, 500, 550 and 600°C.....	68
Figure 4.4	Cross sectional TEM images of 500°C annealed SCBD ZnO film.	70
Figure 4.5	Room-temperature dark electrical conductivity of SCBD ZnO films post-oxidized at 450°C to 600°C in 0-18% O ₂ -N ₂ and vacuum.	72
Figure 4.6	Room-temperature photo-assisted electrical conductivity of SCBD ZnO films post-oxidized at 450, 500, 550 and 600°C measured in vacuum. .	75
Figure 4.7	Room-temperature photo-assisted electrical conductivity of SCBD ZnO films post-oxidized at 450, 500, 550 and 600°C measured in air.	78
Figure 4.8	Room-temperature photo assisted electrical conductivity of 450°C- and 500°C-post oxidized SCBD ZnO films measured in cyclic tests in air.	80



- Figure 4.9 Real-time dependence of room-temperature photo assisted electrical conductivity and photocurrent of a 500°C-post oxidized SCBD ZnO film measured at O₂ concentration varied over a range from 0.1 to 18% (balanced in dry N₂).....83
- Figure 4.10 Room-temperature real-time dependence of photo assisted electrical conductivity of 500°C post-oxidized SCBD ZnO film with a superhydrophobic polymer coating in dry gas of O₂ content varied over a range from 0 to 18%.....87
- Figure 4.11 Real-time room-temperature photo-assisted electrical conductivity of an 500°C post-oxidized SCBD ZnO film covered with a superhydrophobic polymer layer measured in 95%-humid gaseous environment with O₂ concentration varied over a range of 0 to 18% balanced in N₂.90
- Figure 4.12 Immersion dissolved oxygen sensor prototype made of a 500°C post-oxidized SCBD ZnO film. Left and right bottom: pictures of well and poorly protected immersion sensor taken after measurements in water.93
- Figure 4.13 Real-time room-temperature photo assisted electrical conductivity of a 500°C post-oxidized SCBD ZnO films covered with a superhydrophobic polymer layer measured at various dissolved oxygen concentrations from 0% and 100%.95
- Figure 4.14 Three relationships correlating the O₂ concentration in the detected area and a fitting parameter to the time dependence of photocurrent using a 500°C-post oxidized SCBD ZnO film. (a) I_{sat} of an uncoated film sensor versus O₂ concentration in dry O₂-N₂ mixture; (b) I_{sat} of a polymer-coated



The Hong Kong Polytechnic University

- film sensor versus O₂ concentration in 95% humid O₂-N₂ mixture; and (c) decay time of current after turning off UV light versus dissolved oxygen content in water.....100
- Figure 5.1 (a) Resistive response of Pd-coated ns-ZnO film to 2% H₂ balanced in air. (b) Comparison of results obtained at 20°C and 80°C.....103
- Figure 5.2 Real-time dependence of resistive response of a Pd-coated ns-ZnO film to 2% H₂ in air measured at 0, 50% and 90% relative humidity at an operation temperature of 80°C.....106
- Figure 5.3 Real-time dependence of resistive response of Pd-coated ns-ZnO film to 0.1–2% H₂ in air measured at 80°C.107
- Figure 5.4 Comparison of time dependence of resistive response of Pd-coated ns-ZnO film to 2% H₂ in air with and without using UV irradiation measured at (a) 80 and (b) 20°C.109
- Figure 5.5 Cyclic stability tests of the resistive response of a Pd-coated ns-ZnO film exposed alternatively to 2% H₂ in air and dry air at 80°C (a) without using and (b) using UV illumination. The power density of light is 10 mW/cm².112
- Figure 5.6 Comparison of (a) S and (b) t_{res} of a Pd-coated ns-ZnO film measured at 80°C with the published data of various H₂ sensors composed of MO_x nanoclusters (solid symbols) and 1-dimensional MO_x nano particles (hollow symbols) measured at temperatures > 200°C.....114
- Figure 5.7 Simplified model for explaining the photo assisted H₂ sensing process of a Pd-coated ns-ZnO film. Reaction ①: chemisorption of oxygen and



The Hong Kong Polytechnic University

formation of O_2^- ion, Reaction ②: photogeneration of e^-h^+ pairs, Reaction ③: band-to-band recombination, Reaction ④: recombination at deep traps, Reaction ⑤: recombination at shallow hole traps, Reaction ⑥: reaction of h^+ with chemisorbed O_2^- ions, Reaction ⑦: extraction and release of free electrons by surface e^- traps, Reaction ⑧: catalytic dissociation of H_2 at Pd surface, Reaction ⑨: reaction of dissociated H atom with chemisorbed O_2^- ions, and Reaction ⑩: release of free e^- produced by Reaction ⑨ to conduction band.118



List of table captions

Table 2.1	Summary of important performance indexes of a gas sensor.	9
Table 2.2	Summary of the advantages and disadvantages of MO _x -type and NDIR-type oxygen gas sensors.	14
Table 2.3	Comparison of three common types of dissolved oxygen sensors.	20
Table 2.4	A summary of the advantages and disadvantages of popular H ₂ gas sensors.	26
Table 5.1	Comparison of sensing parameters measured at 20°C and 80 °C, with and without UV assist respectively.	104



Chapter 1 Introduction

1.1 Background on oxygen sensing research

Oxygen sensing technology has wide applications in daily life and industries in the circumstances where monitoring of oxygen concentration [O₂] in a gas or liquid is crucially important. Some typical examples are as follows. Monitoring of the O₂ concentration in a workplace like a mining pit [1] is highly desired to ensure that environment is safe and suitable for workers to stay and work. In flow soldering process or metal heat treatment, O₂ concentration in a controlled environment is required to detect for the need of maintaining the O₂ concentration at a low enough level to prevent the molten solder from being oxidized significantly [2]. In food and medication production, the O₂ content in the production line must be monitored and controlled to optimize the fabrication and storage conditions [3]. The level of O₂ used in oxygen therapy must be accurately adjusted in order to maximize the effect of a treatment [4]. With increasing concern about air pollution, O₂ content in air is an important indicator reflecting air quality in offices, households and some public locations in urban areas etc. [5]. A particular class of activities requires detecting oxygen concentration in liquids, most usually water. The measurement is referred to as the detection of dissolved oxygen (DO) content in the liquid. One important occasion is the activity associated with aquaculture and aquarium, where the level of DO has to be known and used for auto controlled via some feedback loop in order to maintain a proper level of O₂ in water for ensuring the health of fishes and water fowls [6,7]. Another example is the production line in a brewery, where the O₂



concentration must be kept at a specific level to achieve the desired quality of the product [8]. Moreover, detection of DO is needed in wastewater treatment [9, 10]. In an aerobic process, an oxygen-rich condition is required for activating bacteria to dissociate organic contaminants; while in an anaerobic process, an O₂-deficient condition is needed for microorganisms to be digested via fermentation, and converted into methane. Detection of DO is also needed in diving and marine activities, where the results of measurements help to check the working condition of breathing facilities [11].

1.2 Background on hydrogen sensing research

Detection of hydrogen is also important in many circumstances, while in most of the cases, measurements are required to be conducted in a gas phase. The reason is that H₂ is an important future fuel expected to provide clean and intensive energy. Concomitantly, it is highly explosive and is potentially dangerous to the human beings [12, 13]. Monitoring of hydrogen level and generation of warning signal in case of accidental leakage of the gas are crucially important to ensure the safety when any H₂-containing fuels are used. The requirement of the performance of hydrogen sensors is anticipated to become more and more stringent associated with the foreseeable popularization of this attractive renewable energy medium. In particular, new generation H₂ sensors are required to have higher detection sensitivity to improve the safety level of leakage detection for matching with the ordinances announced by related government departments and professional bodies of different countries, like the US Department of energy and manufacturers of H₂ powered



vehicles [14-17]. New sensors are also required to have faster response time to a level shorter than 1 s. This is in fact a very stringent requirement and has not been reached by many existing commercialized H₂ sensor products [14]. On the other hand, the advancement of sensor material research creates new rooms for further improvement of sensor's performance and hence the related R&D activities are still very active nowadays.

Development work on new H₂ sensors covers the improvement of many performance indexes. The targets of research are to further broaden the detection range which has already covered a range from ppm level to 100% of the gases. A high sensitivity is still pursued to achieve a lower detection limit. More targets to be attempted include better durability; faster response and recovery time; lower operation temperature preferably to be closer to the ambient level; better selectivity to prevent interference from other unwanted gases or interferants; better batch-to-batch reproducibility; lower power consumption; ease of miniaturization and lower production cost possibly leading to mass production.

1.3 Motivation of the present project

This study was motivated by referring to the abovementioned deficiencies of the present status of the field.

1.3.1 Inspiration from the operating temperature of conventional semiconductor-based gas sensors

A conventional semiconductor-based gas sensor usually uses a large-bandgap



semiconducting element, such as a metal oxide, for generating signal to respond to a gas. The reason is as follows. At room temperature, the material only contains a small amount of conduction charge carriers (electrons and/or holes) due to the large bandgap energy relative to the thermal energy available from the environment. Its electrical resistivity is thereby very high and hence the resistance is hardly measured in practice. As a consequence, the electrons are captured by a small amount of oxygen molecules from the environment which are consequently adsorbed on the sensor's surface. The resistance is reduced a little bit though it is still hardly detected. When an oxidizing or reducing target gas appears, it interacts with the adsorbed oxygen (for a reducing target gas) or conduction electrons (for an oxidizing target gas) through a redox reaction. The subsequent change of the sensor's resistance is still very small. The device is thereby not functioning quite well. For this reason, the sensor is usually heated up to a few hundred °C to increase the population of conduction charge carriers. One of the consequences is that the sensor material may continue to crystallize and the atoms in it may further diffuse or oxidized throughout the course of use. The structure, phase and even composition of the sensing material may change gradually. The gas sensing performance of the device is also changed as time proceeds. These mechanisms are usually accompanied with degradation of the sensing properties.

Second, the temperature of the sensor element may experience certain degree of fluctuation. A feedback control loop is usually required to stabilize sensor's temperature and subsequently the output performance. This remedy would inevitably result in additional cost of production.



Third, the sensor element itself is a hot spot and may have potential risk of igniting an explosive component contained in the detected gas. Hence an explosive arrester is usually added to prevent direct interaction between the sensor and the surrounding substances. This approach would enlarge the size of the device such that miniaturization is significantly hindered. They are difficult to be integrated to quite a large group of products requiring the accessories to have small sizes.

All the above problems could be greatly alleviated if some method can be implemented to effectively lower the operation temperature of the sensor. In practice, a temperature slightly above the ambient one is preferred because at this condition moisture is more difficult to be condensed on the sensor's surface such that the influence from the change of relative humidity in the detected area can be suppressed.

1.3.2 Expected improvements associated with the use of UV light assist

One popular way employed nowadays for lowering the operation temperature of semiconductor-based gas sensors is to illuminate the sensor's surface with light of photo energy above the electron bandgap. The wavelength of the light used for this purpose usually falls in the ultraviolet range. The popularity of this approach is directly related to the widespread of availability of low cost UV light emitting diode (LED).

The main effect of the method is to increase the population of electron-hole pairs such that the gas detection reactions can take place at a temperature much lower than the one for a conventional semiconductor type gas sensor to work effectively. Basically, gas sensing signal is already achievable at room temperature. A



simple heater could be added to rise the operation temperature slightly for suppressing the influence of moisture. Most of the abovementioned drawbacks could be prevented as a consequence.

1.3.3 Expected improvement associated with the use of highly porous oxide sensor materials

Another strategy becoming more popular is to use highly porous nano-structured metal oxide films to make gas sensors for improving the performance. The materials could be made to have pores embedded in a structure, or be constructed by assembling nanoclusters together to leave gap spaces in between. In all cases, the materials are characteristic of having a high porosity and roughness. They are well specified by a characteristic dimension, which can be referred to the average pore size or cluster size. In particular, it usually falls in the nanometer range. The popularity of this approach is initiated from the widespread use of nanomaterials in the field of sensor technology. Some reasons are as follows.

- (i) Gas sensing response is generated by the surface reaction between the sensing material and the detected gas. Since nanomaterials commonly have a large effective surface area compared to that of a bulk one, one expects that the gas sensing signal should also be stronger.
- (ii) The resistive change of a semiconductor gas sensor is generated according to the variation of the thickness of the depletion layer. This layer initially appears at the surface of the material. It has a maximum depth when the sensor is at equilibrium with the background oxygen before the presence of the detected gas (reducing for example). It becomes thinner until the target gas concentration reaches the



upper bound of the gas detection range. The range of the resistance change is determined in accordance to this process. It is made to be the largest if the initial thickness of the depletion layer is close to the average cluster size, and the latter is as thin as possible at highest gas concentration to be detected. The variation of the depletion layer of a semiconductor is usually in the range of a few nanometers, hence a nanomaterial with a similar characteristic dimension is considered to be suitable candidate for the use of making good sensors.

- (iii) The gap spaces in a porous material may connect to form some channels for gas molecules to pass through. The migration speed could be made to be fast compared to that of a dense structure of the same material. Hence, the detected gas molecules can reach and react with the nanoclusters located deeper in the sensor within a shorter time compared to that achieved with a bulk one. A faster reaction rate could thus be obtained. Based the same reason, during loading the detached molecules also migrate through the structure and return to the environment with a short recovery time.

1.4 Aims and objectives of the present project

Based on the present status of the field as summarized above, this project was carried out with the following objectives.

- (i) We synthesized highly porous ZnO films using a Super Cluster Beam Deposition technique (SCBD) method for making samples for investigating their gas sensing properties. SCBD ZnO films produced with this technique are composed of nanoclusters and hence are expected to have a large effective surface area to



- facilitate obtaining a stronger sensor response.
- (ii) We also aimed at characterizing the phase and structure of the film samples. Experiments employed in this part of study include the X-ray diffraction, infrared absorption, Raman scattering and porosity etc.
 - (iii) The next is to investigate the electrical conductivity with and without UV light illumination, and at different temperatures, i.e. 20°C and 80°C. The output was measured against the concentration of the detected substances. The first is oxygen. Measurements were conducted in different environments, including dry gas phase with bared film sensor; dry gas phase with NeverWet coated film sensor; humid gas phase with NeverWet coated film sensor; and water with a specially designed device based on a NeverWet coated film sensor. Real-time variation of the resistive response is recorded and correlated with the oxygen content. In particular, the tests in water were done to aim at assessing the potential of developing a dissolved oxygen sensor using the SCBD ZnO films. The next to be detected is hydrogen. All the tests were conducted in gas phase. The film samples are decorated with a palladium film for introducing catalytic assist.
 - (iv) The last part is to analyze the correlation of the real-time dependence of the resistive response to the concentration of the detected substances. Models based on some physiochemical mechanisms, like surface sorption, photogeneration of excess charge carriers etc., are introduced. Curve fitting were carried out to extract characteristic parameters like response time and recovery time to help interpreting and getting deep insights of the gas sensing process.



Chapter 2 Background of Gas Sensors Technology

2.1 Performance indexes of a gas sensor

A gas sensor is a device working for reflecting the health condition of the atmosphere, workplaces and households etc. Therefore, a number of performance indexes of a gas sensor are defined to reflect its capability for this purpose. The parameters of most concerns are summarized in Table 2.1.

Table 2.1 Summary of important performance indexes of a gas sensor.

Parameter	Symbol	Definition
Sensor response	S	Fractional change of a physical property of a sensor when a sensor reacts with a gas. The physical property could be selected as the resistance, electrical conductivity, optical transmittance or reflectivity etc. The magnitude of the change is expected to change with the variation of the concentration of the target gas present in the detected area. For example, if electrical conductivity σ is used, its value in the background environment is σ_b and that detected upon the presence of the detected gas is σ_{gas} , the sensor response is



		<p>obtained as</p> $S \equiv \sigma_b - \sigma_{\text{gas}} / \sigma_{\text{gas}}, \text{ when } \sigma_b > \sigma_{\text{gas}} \text{ (the sensor is less conducting in the presence of the target gas), or}$ $S \equiv \sigma_b - \sigma_{\text{gas}} / \sigma_b, \text{ when } \sigma_{\text{gas}} > \sigma_b \text{ (the sensor is more conducting in the presence of the target gas).}$ <p>Another example usually used in published studies and also this study is the use of the resistance of the sensor R, where S is</p> $S \equiv R_b - R_{\text{gas}} / R_{\text{gas}}, \text{ when } R_b > R_{\text{gas}}, \text{ or}$ $S \equiv R_b - R_{\text{gas}} / R_b, \text{ when } R_{\text{gas}} > R_b$
Selectivity		Capability of the sensor to selectively respond to the target gas only. This is usually assessed by measuring the output of the sensor to the target gas and potential interferants, and then compare their relative magnitudes.
Stability/ Repeatability		Capability of the sensor to give stable and repeatable response over a long time of use or a large number of loading-unloading cycles.
Sensitivity	$\delta S / \delta C$	Differential change of sensor response associated with a differential change of the



		target gas concentration, C.
Response time	T_{res}	Time required for the sensor response to reach 80% of the total change of the response associated with a specific target gas concentration.
Recovery time	T_{rec}	The time required for the sensor response to recover by 80% of the total change of the response for a specific target gas concentration.
Linearity		Linearity between sensor response and target gas concentration.
Operating temperature	$T_{operate}$	The temperature of the sensor during operation.
Upper detection limit		Maximum target gas concentration just before the sensor output becomes saturated and insensitive to further increase of the gas concentration.
Lower detection limit		Minimum detected gas concentration below which no any change of sensor output can be detected.
Resolution		Minimum change of target gas concentration detectable according to the change of the



		sensor output.
--	--	----------------

2.2 Review of O₂ gas sensors

A variety of oxygen gas sensors is available and chosen according to the specific requirements of use. However, each type of gas sensors is found to have respective advantages and shortcomings.

2.2.1 Metal oxide semiconductor (MO_x) O₂ gas sensors

A sensor of this type has a semiconductor sensing element for producing a signal to respond to the target gas. It is usually a metal oxide (MO_x), like zinc oxide, titanium oxide or tungsten oxide. They all have large bandgap energies above a few eV. The main advantages of MO_x gas sensors are the simplicity of their structures, low cost and the ease of integration to many portable appliances. A MO_x sensor could be designed to give resistive or capacitive response when interacting with a target gas through some physicochemical reactions.

An MO_x gas sensor is generally required to work at an elevated temperature. This is because the bandgap of a metal oxide is in general much larger than the thermal energy available from the environment at room temperature. As a consequence, the charge carrier population is small and the material is rather resistive. Therefore, the base resistance as well as the resistive change caused by presence of a target gas at an ordinary level of concentration are hardly detected. A high operation temperature is therefore applied for generating a large enough electron-hole population, such that the base resistance of the sensor is properly lowered, and the resistance change



caused by the redox reactions between the surface sorbed oxygen species and the target gas becomes discernable. The thermal drift of the sensor response may be rather significant due to the thermal fluctuation of the sensor and continuous annealing of the sensor material. Persistent oxidation and atomic diffusion also can alter the phase structure or composition and influence the output characteristics, rendering the sensor's performance to become unstable and unrepeatable. Even worse, the change of the physical parameter used for correlating with the target gas concentration may need a long time to recover or in some cases the change is irreversible. Practically, typical range of the error due to thermal effect could be as larger as +/-20%.

2.2.2 Non-dispersive infra-red (NDIR) O₂ gas sensors

Another popular oxygen gas sensor is non-dispersive infra-red (NDIR) gas sensors. A sensor of this type does not have a sensing material to directly react with the target gas. No instability is caused by the change of the chemical state of a sensing material in the device. Alternatively, the operation of an NDIR sensor is based on the detection of absorption spectrum of the detected gas molecules in the infrared (IR) range. In particular, a typical design of an NDIR sensor has two optical paths, which each ends up with a photodetector. They work concurrently. One collects the absorption spectrum of the background, usually contains air, moisture, CO₂ etc. The other one collects the absorption spectrum combining that of the background and the film sample. This operation principle is expected to compensate any unwanted interference so as to obtain the net IR absorption spectrum of the film material and



to eliminate random fluctuation. However, an NDIR gas sensor requires a higher power consumption for maintaining the operation of the IR light source. If a battery is used, it requires to be recharged rather frequently. The volume of the sensor is also too large to be integrated to many portable appliances. According to the many practical tests, notable drift of output is also unavoidable. The reason is still unknown. We suspect that it may be from the mechanical instability of some optical components inside the device, or be due to uncontrolled condensation of moisture on these components such that the conditions along the reference light path and sample light path are not identical.

The abovementioned advantages and disadvantages of the two sensor types are summarized in Table 2.1.

Table 2.2 Summary of the advantages and disadvantages of MO_x -type and NDIR-type oxygen gas sensors.

Sensor type	MO_x	NDIR
Working principle	Physiochemical reactions between a semiconductor metal oxide and the target gas	Detection of the characteristic IR absorption spectrum of the target gas
Detected variable	Mostly resistive or capacitive change of the sensor element	IR absorption at the wavelengths of the spectral line(s) of the target gas



		molecules
Advantages	Low cost and ease of integration to manyh portable appliances	Improved suppression of background interference, and less influence caused by the change of the chemical stage of a sensing material
Drawbacks	Error due to thermal drift up to +/- 20%; significant thermal drift; poor reproducibility; slow recovery rate	Higher power consumption; incoherent drift of reference and measurement arms

2.3 Review of dissolved oxygen sensors

Dissolved oxygen detection is concerned in this study. We describe three widely used dissolved oxygen sensors in the following. They are mostly used in water. Practically, a dissolved oxygen sensor is usually mounted to a meterstick. It is then placed at a position where the oxygen content is needed to know. The sensor is also often equipped with a data logger for real-time monitoring or with a transmitter to send data to a control unit. The data is useful for real-time feedback for auto control of some process, and hence is particularly important in quality control in a production flow.

2.3.1 Optical dissolved oxygen sensors

The first DO sensor type to be introduced is optical dissolved oxygen sensor. The structure is depicted schematically in Figure 2.1. Its active component is made to contain a certain luminescent dye. The dye was illuminated by a blue excitation light beam from a light source. Electrons in the dye gain energy, and tend to return to the ground state by emitting photons [18]. When dissolved oxygen is present, the emitted photon energy is lowered (longer wavelength) because some energy losses due to interaction with oxygen molecules. The intensity of the emitted light is also altered with the concentration of the DO concentration [19]. In addition, the lifetime of the luminescence is also affected and useable for indicating the oxygen content in the medium [20].

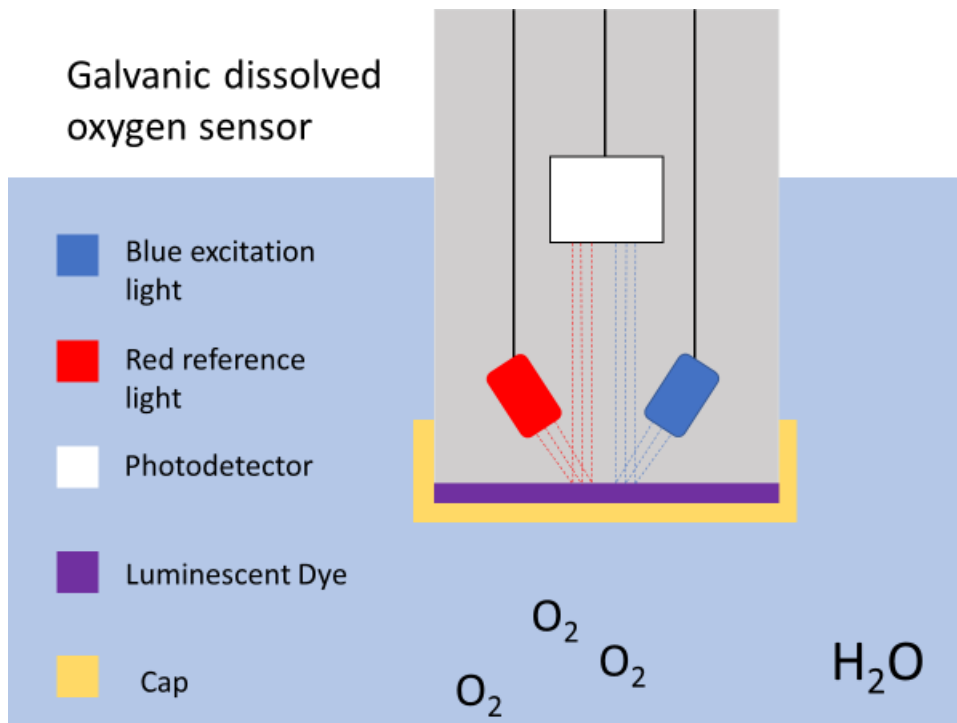


Figure 2.1 Cross-section of an optical dissolved oxygen sensor. [91]



2.3.2 Polarographic dissolved Oxygen Sensors (electrochemical)

Another type of widely used DO sensors is based on electrochemical reaction. The structure is depicted schematically in Figure 2.2. A sensor based on electrochemical reaction is commonly referred to as amperometric or Clark-type sensors.

A polarographic DO sensor, or an electrochemical DO sensor, consists of a silver anode and a noble metal (such as gold, platinum or infrequently, silver) cathode immersed in a potassium chloride (KCl) solution [21]. After the device is powered, it requires 5 to 60 minutes to warm up. Meanwhile, the electrodes are polarized. A voltage of around 0.4 to 1.2 V is then applied to polarize the electrodes [21]. The applied electric field drives electrons to move towards the cathode. The anode is set at a higher potential, namely being more positively polarized relatively to the cathode [22]. An internal electric close loop is established [23]. When oxygen molecules in the medium diffuse across a membrane, they are reduced at the cathode, an electrical signal in the form of a current is detected [24]. If the polarizing potential is held constant, the change of the current flow in the sensor can be correlated to the reduction rate of oxygen and hence can be correlated to the concentration of dissolved oxygen concentration in the detected medium [24]. In other words, more oxygen passing through the embrace to enter the device, more oxygen molecules are reduced and a greater electrical current signal is displayed by the polarographic DO sensor.

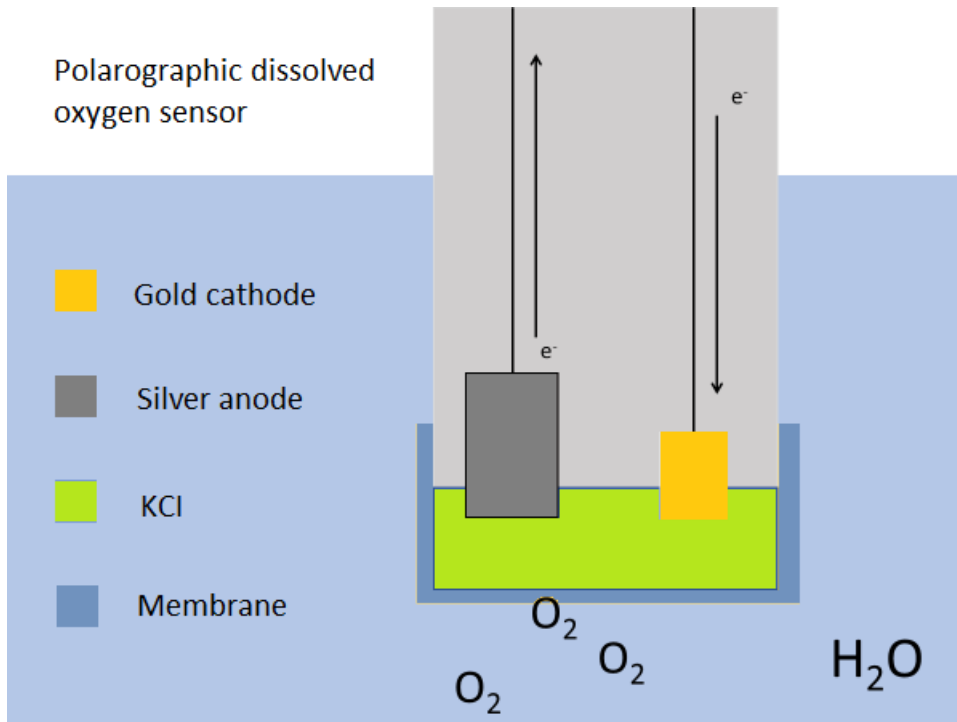


Figure 2.2 Cross-section of a polarographic dissolved oxygen sensor [91]

2.3.3 Galvanic dissolved oxygen sensors (electrochemical)

A galvanic DO sensor is also an electrochemical type sensor. The structure is depicted schematically in Figure 2.3. Its electrodes are made of two different metals having different electron affinity (the tendency of attracting electrons) [25]. When they are placed in an electrolyte solution, self-polarization between the two metals is built up automatically to result in a potential difference between them [26]. The self-polarization evolves very fast as if no warm-up time is required. Hence the response time is rather short. The condition for the sensor to be workable is that the self-polarization voltage should not be less than 0.5 volts for reduction of oxygen to become feasible [26].

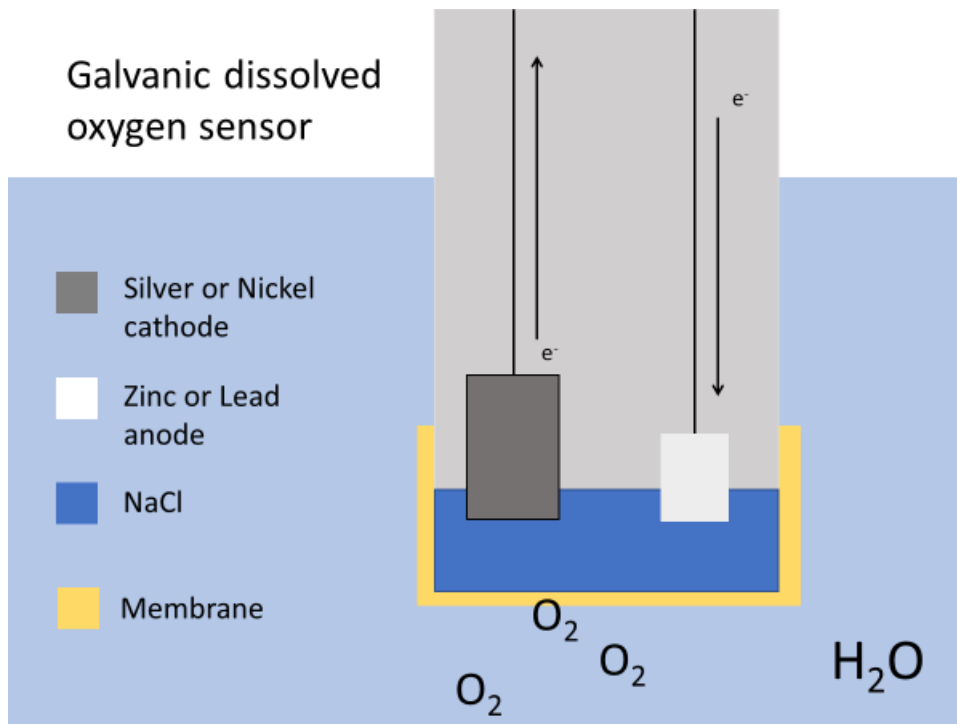


Figure 2.3 Cross-section of a galvanic dissolved oxygen sensor. [91]

We further note that the anode in a galvanic dissolved oxygen sensor is usually zinc, lead or any one of the active metals, while the cathode could be silver or one of the noble metals [27]. The electrolyte solution can be sodium hydroxide, sodium chloride, or another inert electrolyte [21, 29]. The electrochemical reaction in galvanic DO sensors is very similar to that conducted in a polarographic DO sensors, but no external applied potential is needed. The electrodes can self-polarize, with the electrons traveling internally from the anode to the cathode [24]. The cathode remains unreactive but serves as a path for electrons to pass through. It does not participate in the reaction [61]. Thus, the anode is oxidized and oxygen is reduced at the surface of the cathode.

Each type of gas sensor has its own advantages and shortcomings. We give a



comparison among the features of the three sensors in

Table 2.3. Some information on the general limitations of commercial dissolved oxygen sensors is also shown.

Table 2.3 Comparison of three common types of dissolved oxygen sensors.

Sensor type	Optical	Polarographic	Galvanic
Advantages	Stable Short warm up time No stirring required	Fast response time	Fast response time Not need to replace electrolyte No warm-up period
Limitations	Dependent on temperature Higher power consumption Lower accuracy	Warm-up period required Frequent replacement of electrolytes Stirring required	Short life-time Stirring required

2.4 Review of popular H₂ gas sensors

This section presents the features of some popular types of H₂ sensors.

2.4.1 Pd-based resistive-type H₂ gas sensor

The study of the H-Pd system was initiated from the year of 1866. It was found that hydrogen can permeate into Pd [30]. At the same time, the metal is hydridated and accompanied by a substantial change of the electrical resistivity. It was thereby inspired that the H-induced response could be utilized for detection of hydrogen, with



the resistive change as an indicator for correlating with the variation of surrounding hydrogen concentration. A sensor of this type is thereby referred to as a Pd-based H₂ sensor.

In more detail, a piece of Pd-based component is a catalyst which accelerates dissociation of H₂ molecules into H atoms on its surface. The total volume of hydrogen gas dissolved in a piece of Pd can be over 800 times of its own. When H atoms diffuse to enter the lattice of Pd, they are located interstitially. At this stage, a Pd hydride, denoted as α -phase, is formed. The H content can be increased to 2.5% without affecting the lattice structure [31], namely an FCC lattice. However, a little expansion of lattice constant from 0.388 to 0.39 nm is detected in accordance with the increase in H content [32]. If more H atoms are incorporated to the solid, a transformation from the α -phase to a β -phase occurs. The β -phase structure also has an FCC lattice. H atoms in the solid are still located at interstitial sites. However, the lattice constants exhibit larger expansion to by 3%, namely to a magnitude of 0.401 nm. Upon completion of the transition, a bit more H can still be able to enter the solid, and the lattice constant further increases slightly.

In connection to the two hydridation processes, the resistivity ρ of the Pd-based sensor increases monotonically with increasing H content. In the α -phase, ρ increases by a factor of 1.05 when H content increases to 2.5%. [33, 34]. In the α -to- β transition, H content increases to reach 40%, whereas ρ increases by 1.8 times.

Pd-based resistive-type H₂ sensors are less sensitive to many interferants. It is also insensitivity to the change of the pressure of the environment and relative humidity RH. It works well at a low operation temperature T_{operate} close to the room



temperature. The reproducibility of production is fairly good. It can be made in the form of a thin film sensor and held is convenient to be miniaturized and fabricated with mass production process. However, the sensor response is rather low (e.g. $\sim 7.6 \times 10^{-7}$ /ppm at 2% H₂) [35]. The response time is also too long (e.g. ~ 60 s) to satisfy the requirements of many applications. The output depends on the surrounding environmental temperature and hence exhibits thermal drift. The power consumption is high and the raw material is expensive.

2.4.2 MO_x type H₂ gas sensor

Many metal oxide semiconductors can respond to H₂. Some of them have been used to make commercial H₂ sensors. The structure is the same as that of an MO_x-type O₂ sensor, except that it is operated in an air or a background of stable oxygen concentration. Under this condition, H₂ plays the role of the target gas and its concentration is expected to be small. The working principle will be further elucidated in Section 2.5.

An MO_x H₂ sensor is advantageous of having a high sensor response, e.g. ~ 0.15 /ppm at 2% H₂ [51]. The response time is short, e.g. 5 – 10 s. However, the selectivity against other reducing gases is poor. The output may shift with the change of surrounding pressure T_{environ} and RH [36-53]. Furthermore, it needs to work at an elevated operation temperature T_{operate} , and hence the thermal instability of the output is constantly a problem. Since an explosion arrester is needed, miniaturization is hindered. The power consumption is also high, usually at a level of ~ 500 mW. Hence, the sensors are not suitable to be integrated to many battery-powered portable



appliances. A circuit may be added to stabilize the operation temperature, but the production cost is risen as a consequence [62-66]. It is also very often that the sensor components are fabricated using thick film technology, like screen printing technique. The properties of thick materials made with this technique are not easily controlled accurately, and the quality and reproducibility of the performance of the products are hardly maintained accurately and consistently.

2.4.3 Electrochemical-type H₂ gas sensor

The structure of an electrochemical-type H₂ sensor is similar to that of an electrochemical-type O₂ sensor [64-66, 54-56], except that H₂ molecules are dissociated into H atoms. H atoms are generated in the electrolyte between the electrodes. An amperometric [54-56] or a potentiometric signal [55] is generated as a result.

The advantage is that the output is insensitive to the variations of surrounding pressure, temperature and relative humidity (RH). An electrochemical-type H₂ sensor can work at a temperature close to the ambient one, and does not need to have a heater as well as a temperature controlling circuit. However, its sensor response is low, e.g. ~ 0.002/ppm at 1.15% H₂ [55]. The output is readily interfered by other reducing gases. Batch-to-batch reproducibility is not satisfactory. Miniaturization is not easily realized, and the production cost is also high.

2.4.4 Catalytic combustion-type H₂ gas sensor

A catalytic combustion-type H₂ gas sensor is made to contain a catalyst which



could be one of the elemental components forming the sensor material. It can be added on the surface as a decorative coating. The catalyst is added for altering the selectivity of the sensor for targeting at a specific detected gas and suppressing the response to other unwanted interferants.

During operation, the sensor is heated up to an operation temperature $T_{\text{operation}}$. Molecules of a combustion gas like H_2 are oxidized to emit heat, causing the temperature of the sensor to rise. The change is detected by a platinum (Pt) thermometer and becomes the output signal.

A catalytic-type sensor is insensitive to atmospheric pressure, environment temperature and relative humidity RH. The production process is highly reproducible. However, sensors of the type have some disadvantage. First, the sensor response is low, typically below 5.3×10^{-4} /ppm at 1% H_2 . [57] Second, the operation temperature is as high as a few hundreds of °C. Third, even though a carefully selected catalyst is used, it cannot completely eliminate the interference from some other combustion gases, and the signals from them are not differentiable. The size of the device is also difficult to be miniaturized. Power consumption is high, typically above 500 mW.

2.4.5 Thermal conductivity-type H_2 sensor

The thermal conductivity of H_2 is the largest among all gases. A thermal conductivity-type H_2 gas detected the change of the thermal conductivity of a gas sample. It is particularly sensitive to the presence of H_2 .

The advantages of a sensor of this type are similar to those of a Pd-based resistivity-type one. The disadvantage is that the sensor response is low, namely ~



2.5×10^{-6} /ppm at 10% H₂ [60]. The signal also exhibits strong dependence on surrounding temperature. Furthermore, the response time is around 30–60 s, which is not fast enough in many applications like detection of H₂ leakage in a vehicle. The life time of use is about the shortest among most types of H₂ sensors. Miniaturization is difficult. Power consumption is also high, e.g. > 500 mW.

**Table 2.4 A summary of the advantages and disadvantages of popular H₂ gas sensors.**

Sensor type	Pd-based resistive-type	MO _x -type	Electrochemical-type	catalytic combustion-type	Thermal conduction-type
Working principle	Hydrogenation of a Pd-based material	Surface sorption of background oxygen and redox reactions between surface sorbed oxygen species and H ₂	Dissociation of H ₂ in an electrochemical cell and generation of a voltage output	Combustion of a flammable gas causing temperature of the sensor to rise	Change of thermal conductivity due to the presence of the target gas
Detected variable	Resistive change of the Pd-based material	Resistive change of the MO _x material	Amperometric or potentiometric signal	Rise in temperature of the sensor	The change of thermal conductivity at the presence of



					H ₂
Advantages	Resistant to the presence of most interferants; Insensitive to ambient pressure and RH.	Large sensor response; Fast response.	Insensitive to the change of ambient pressure, temperature and RH; Low operation temperature; No heater and temperature controlling circuit.	Insensitive to the change of ambient pressure, temperature and RH; Highly reproducible in production.	The same as those of a Pd-based resistivity-type H ₂ sensor.
Disadvantages	Low sensor response; Long recovery time; Affected by ambient temperature;	Poor selectivity; Affected by ambient pressure and RH; High operation	Low sensor response; Poor selectivity; Poor reproducibility in	Low sensor response; High operation temperature; Poor selectivity	Low sensor response; Strong dependence



	High cost.	temperature; Poor stability; High power consumption; Not miniaturizable; High cost; Poor reproducibility.	production; Not miniaturizable; High production cost.	among combustion gases; Not miniaturizable; High power consumption; High production cost.	on temperature; Long response time; Short life time; Not miniaturizable; High power consumption; High cost.
--	------------	---	---	--	---



2.5 Detailed description of the working principle of MO_x sensors

When a MO_x sensor interacts with oxygen molecules, oxygen species can be adsorbed on the surface due to two major mechanisms. One is referred to as the physisorption originating from weak Van der Waals interaction. No net charge is transferred in this case and hence no strong chemical bond is formed. The next is referred to as chemisorption, where stronger transfer or sharing of electrons occurs, leading to the formation of chemical bond, and hence the energy involved in the interaction is much larger. In both cases, a depletion layer is formed at the surface associated with the drop of electron concentration of conduction electrons near the grain surface. A rise of overall electrical resistivity would be detected, first because of the rise of resistance at the grain surfaces, and second because of the presence of inter-granular potential barriers across the contact region between adjacent grains.

When a reducing gas enters the detected region, the molecules react with some of the surface sorbed oxygen molecules. The product of the reaction is usually volatile and readily detach from the surface. The electrons originally trapped by the surface sorbed oxygen are released and return to the MO_x . The depletion layer becomes thinner, and the resistance of the MO_x drops as a consequence. The resistance change can be correlated to the change of the target gas concentration. We emphasize that the reaction is a dynamical process lasting over a period specified by the reaction time, and the real-time change of the sensor response and the rate of the change are closely related to the details of the physiochemical processes, which include a number of complicated processes like diffusion, adsorption and desorption of the

species involved (Figure 2.4).

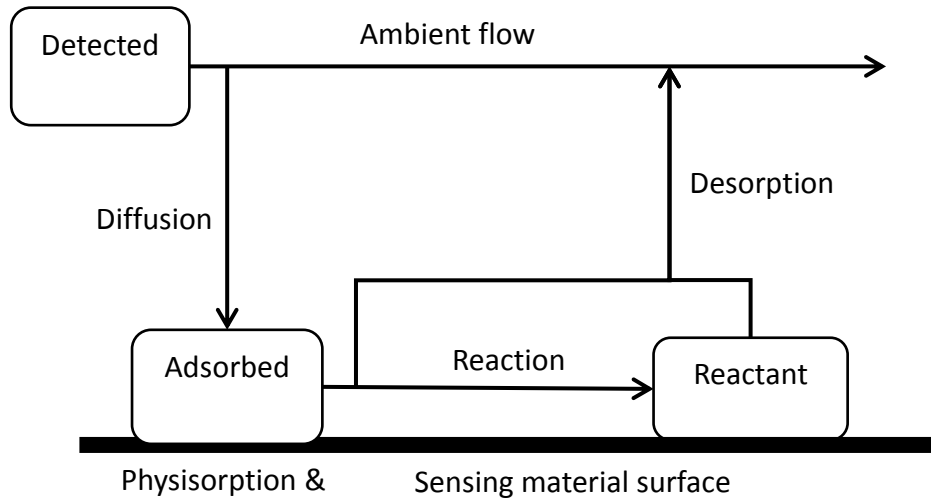
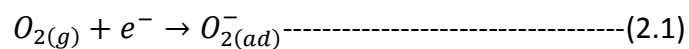
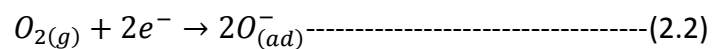


Figure 2.4 Gas sensing process realized by a semiconductor-type gas sensor.

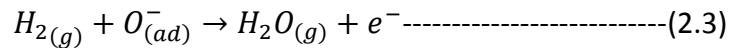
The physiochemical reaction is further elucidated using Figure 2.5. Adsorption of O_2 molecules on the MO_x surface involves trapping of conduction electrons and formation of negatively charged ions. The reaction is



At a higher temperature environment or with higher energy external excitation, the adsorbed oxygen ions could be further dissociated into atomic species,



When a reducing gas is present, the molecules interact with the surface sorbed oxygen ions, such that the electrons are released and return to the sensor. If the reducing gas is H_2 , the reaction is denoted as



The water molecule is volatile and readily leaves the surface. A conduction electron is generated in the process and returns to the oxide. The electron concentration in the sensor is increased and the depletion layer of the grains' surface becomes thinner. The electrical conductivity rises as a consequence.

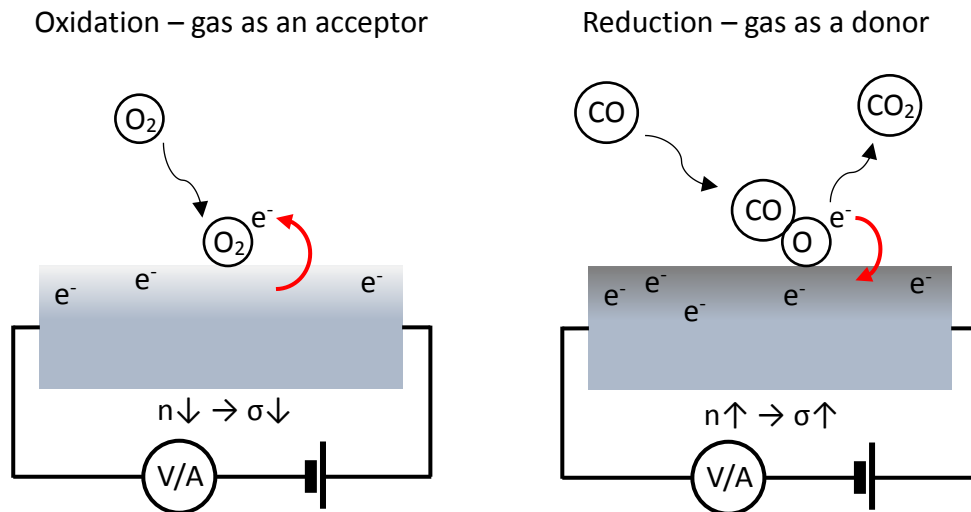


Figure 2.5 Illustration describing a redox reaction in a reducing gas or an oxidizing gas.

Another mechanism affecting the overall electrical conductivity of the MO_x is associated with the potential barrier formed at the grain boundaries. When depletion layer at the grain boundary is formed, a potential barrier across the grains is established. Electrons need to overcome the potential barrier when crossing the two grains. This scenario is presented schematically in Figure 2.6.

The presence of a reducing gas removes some of the adsorbed oxygen. This

causes the depletion layer at the grain boundary to become thinner. The height of the potential barrier drops. The electrical conductivity increases as a consequence and exhibits a dependence of the concentration of the reducing gas.

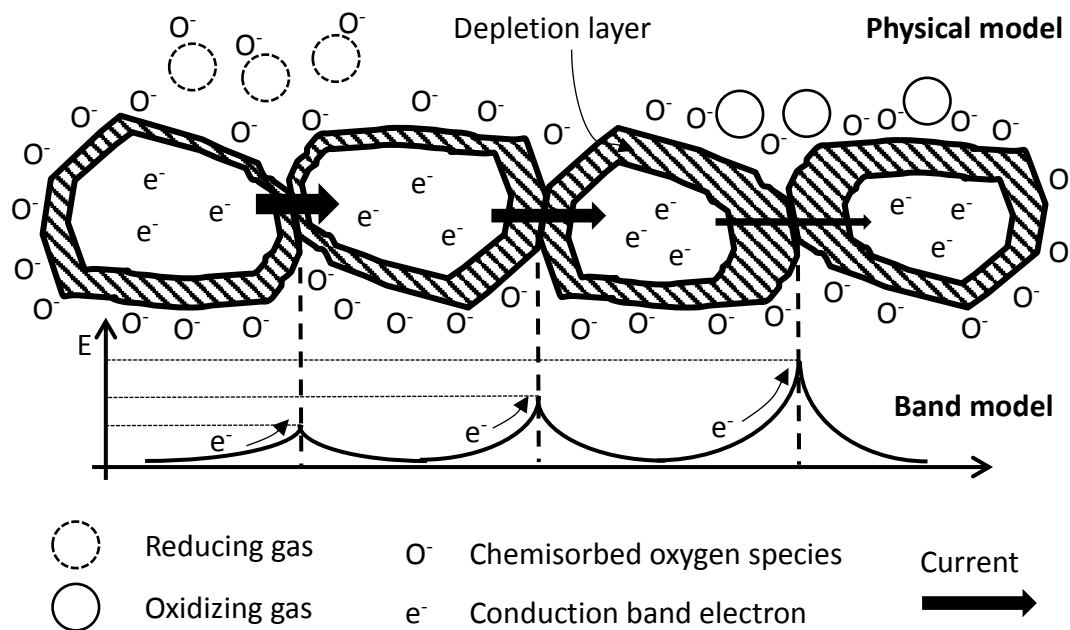


Figure 2.6 Physical principle of gas sensing effect of a polycrystalline oxide semiconductor.

2.6 Recent attempts for improving MO_x gas sensors and related phenomena

Referring to the potential of MO_x materials in making commercial gas sensors, some recent attempts have been employed for seeking improvement of the gas sensing properties of MO_x -type gas sensors. The related physical phenomena are also described in this section.



2.6.1 Use of nanomaterials --- grain size effect

The first approach is to apply nanomaterials to make sensing elements. This is an effective way to increase the area-to-volume ratio for increasing the effective interfacial area between the target gas and sensors. If the nanoclusters are so small that they are almost completely depleted by surface sorbed oxygen species from the background at equilibrium state, the overall resistance of the sensor is the maximum. If the depletion layer becomes negligibly thin when the concentration of the detected gas (reducing) reaches the upper bound of the target detection range, the dynamic range of the resistive response of the sensor is expected to the maximum. This is the most ideal operation condition of the sensor for it to provide the greatest range of sensor response in a specific application.

In addition, the gap space inside the nanostructure of the material greatly facilitates the migration of gas molecules such that the responding rate should be much faster than that of a bulk one.

This latest move of advancement inspires us to select a highly porous MO_x material for our study. We therefore selected the highly porous ZnO thin film material made by using a very special physical vapor deposition technique, which would be further described in Chapter 3.

2.6.2 Use of photo assist with photons of above-bandgap energy

For increasing the electrons and holes concentrations in an MO_x sensor for it to give reasonably strong sensor response at a temperature close to the ambient one instead of operating the sensor at a high temperature, more co-workers attempt to



illuminate a semiconductor MO_x of a direct bandgap with light of photon energy larger than the bandgap energy. This technique starts to widespread since low-cost UV-LEDs become popular and easily available. The base electrical conductivity of the substance under light illumination is greatly lowered from that detected in dark. The photogenerated electrons and holes would actively participate in the gas sensing process and considerably affect the gas sensing performance of the sensor.

2.6.3 Photoconductivity phenomenon

This section gives a brief review of photoconductivity phenomenon of a direct-bandgap semiconductor. If the maximum energy of the valance band and the minimum one in the conduction band have the same crystal momentum k , as shown in Figure 2.7. Transition of an electron across the bandgap only needs to obey the condition of conservation of energy

$$h\nu = E_f - E_i, \text{-----(2.4)}$$

whereas the condition of conservation of the crystal momentum, namely

$$\hbar k_i = \hbar k_f, \text{-----(2.5)}$$

is readily satisfied without requiring generation or annihilation of a phonon.

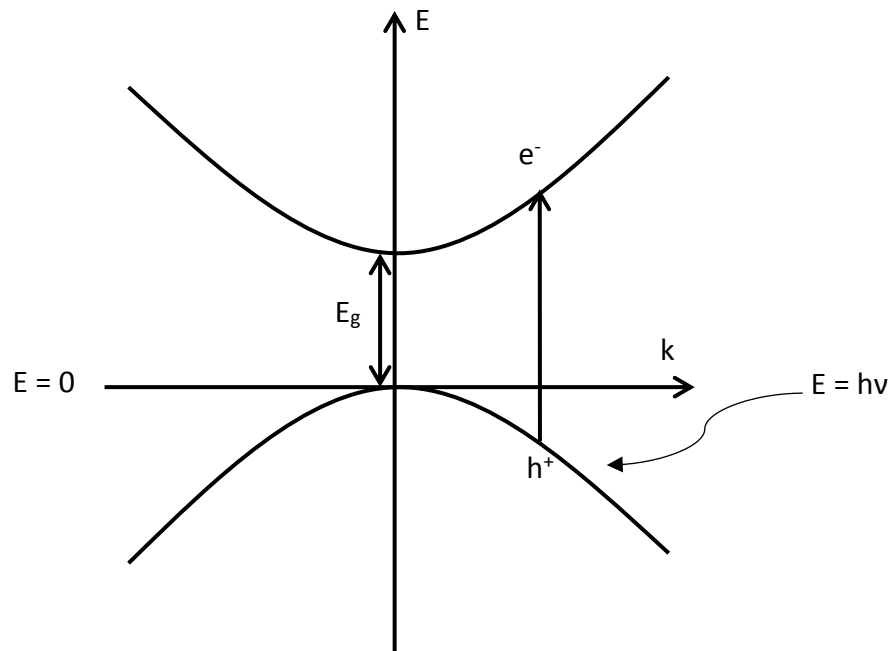


Figure 2.7 Schematic diagram of electron transition in a direct band gap semiconductor.

The relationship between the optical absorption coefficient, α , of a direct bandgap semiconductor against incident photon energy can be described by using the formula

$$\alpha = \text{constant} (h\nu - E_g)^{1/2} \text{-----}(2.6)$$

It shows a linear dependence of the square of α on photon energy $h\nu$ in the above-bandgap region. A cutoff occurs at the point of a photon energy equal to the direct bandgap E_g .

The wavelength dependence of α can be determined experimentally by measuring the transmittance of light through a specimen of a thickness t . Transmittance is defined as I/I_0 , with I and I_0 being the intensity of incident and



transmitting light, which are related as

$$I = I_0 e^{-\alpha t} \text{-----(2.7)}$$

Rearranging the equation, α is obtained as

$$\alpha = \frac{1}{t} \ln\left(\frac{I_0}{I}\right) \text{-----(2.8)}$$

Another formula applicable to disordered semiconductor is the Tauc plot [28], which states that $(\alpha h\nu)^{1/2}$ varies linearly with $h\nu$. The linear part of the plot can be extrapolated to determine the intercept at the $h\nu$ -axis (Figure 2.8), which is shown to be a good estimate of the bandgap energy E_g of the semiconductor.

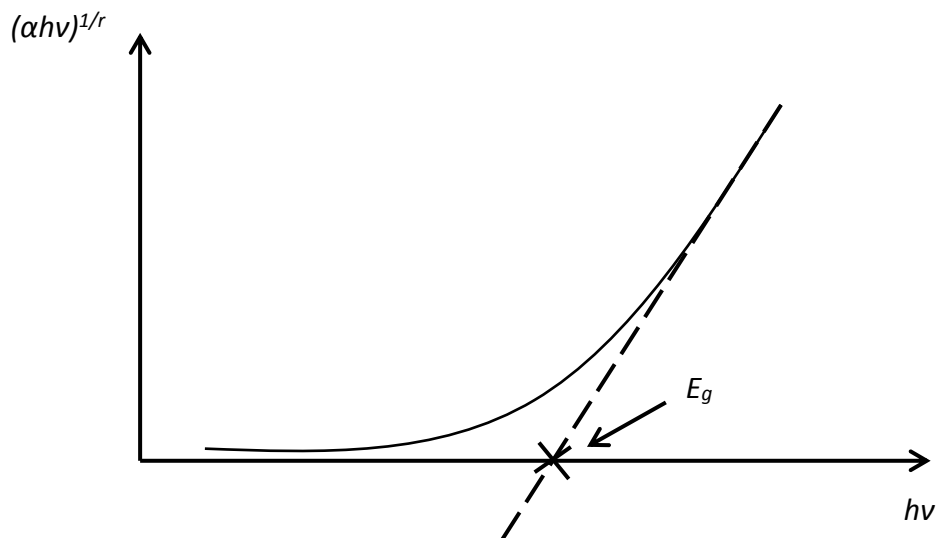


Figure 2.8a Tauc plot of $(h\nu)^{1/2}$ against $h\nu$. The extrapolation of the linear part of the curve cut the $h\nu$ -axis at a point which is good estimate of the bandgap energy E_g of a disordered semiconductor.



Upon generation of electron-hole pairs by UV illumination, the electrical conductivity of the semiconductor is changed to

$$\sigma = e(n + \Delta n)\mu_e + e(p + \Delta p)\mu_h \text{-----(2.9)}$$

where e is the electron charge; n and p are the electron and hole concentrations in dark; Δn and Δp are the increments of the electron and hole concentrations generated by the light; μ_e and μ_h are their drift mobilities. Photoconductivity is defined as the increase of electrical conductivity

$$\begin{aligned} \Delta\sigma_{\text{photo}} &= e(n + \Delta n)\mu_e + e(p + \Delta p)\mu_h - en\mu_e + ep\mu_h \\ &= e\Delta n\mu_e + e\Delta p\mu_h \text{-----(2.10)} \end{aligned}$$

Photo-induced conduction lowers the resistance of the semiconductor. The resistance is therefore more easily measured. Furthermore, as illustrated in Figure 2.9, the photo generated carriers interact actively with the surface sorbed oxygen species. For example, photo-induced holes can diffuse through path 1 to approach the MO_x surface, where they recombine with the trapped electrons to result in detachment of surface sorbed oxygen species. Photo-induced electrons can migrate through path 2 or 3 to reach the MO_x surface, where they are trapped by oxygen molecules. At the same time, oxygen species are adsorbed on the surface. These processes conduct with a low threshold energy compared to that required in dark. As a consequence, the surface sorption-desorption of oxygen molecules proceeds with a much faster frequency, and a new equilibrium is reached. This scenario facilitates the reducing target gas to alter the equilibrium state to result in a stronger sensor response and a faster response rate for using the resistive change as the gas sensing signal.

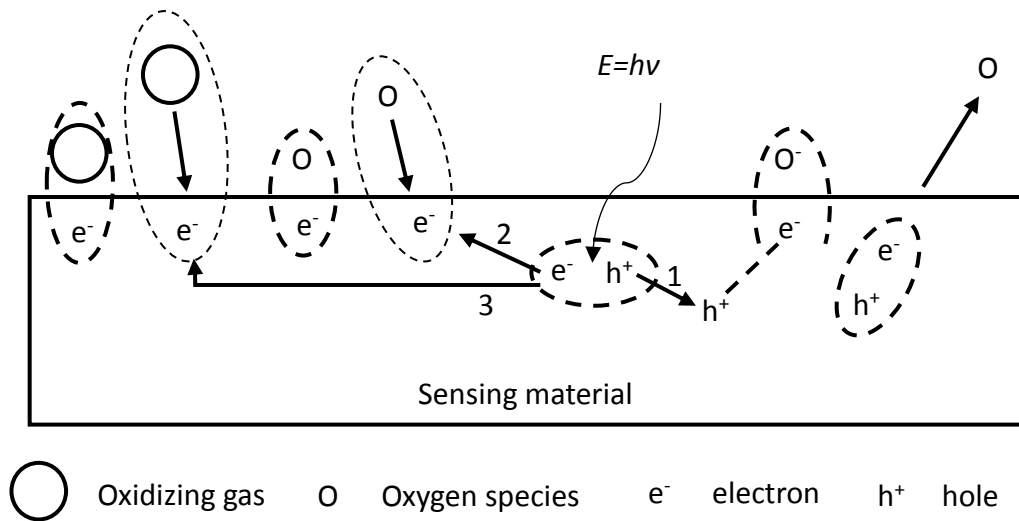


Figure 2.9 The influence of photo generated electron-hole pairs on adsorption-detachment of oxygen.

2.7 Defect induced persistent photoconductivity phenomenon

The surface of a porous material is in general different from a well crystallized one for having a considerable amount of defects and trap states. Charge carriers can be trapped by the released from the surface trap states, and contribute to electrical transport and increase the electrical conductivity.

When the material thin, the influence of surface transport process is more significant. The density and properties of the surface trap states would have more significant influence on the gas sensing properties. The way that they affect the sensing response is to allow more trapped charge carriers to transport via the surface trap states. This mechanism could prolong the time for the photocurrent to reach equilibrium. The recovery time of the material resistance after turning off the



excitation light source to the dark level is also very long due to the much longer lifetime of the trapped charge carriers. The relationship between these phenomena and the gas sensing process of an MO_x are little investigated so far. More detailed studies are needed for giving a better explanation of the real-time dependence of the light assist electrical gas sensing response of a nanostructured MO_x semiconductor material which is believed intrinsically to have quite a large amount of surface defects.



Chapter 3 Experimental methods

3.1 Fabrication of highly porous nanoclustered ZnO films

3.1.1 Supersonic Cluster Beam Deposition (SCBD)

Supersonic cluster beam deposition (SCBD) is basically a physical vapor deposition (PVD) method. It is different from many other PVD techniques for relying on a very specific process. The material produced from this process is found to be in the form of an assemble of nanoclusters. It is very porous and rough. According to the review presented in the previous chapters, these features appear to be ideal for the material to show good gas sensing properties.

Our SCBD system consist of three main parts, namely a discharge chamber, an expansion chamber and a deposition chamber.

An SCBD process (Figure 3.1) starts from generating micro-plasmas on a 2-mm Zn rod target by means of a Pulsed Microplasma Cluster Source (PMCS) unit. The process is conducted in the discharged chamber maintained at a reduced pressure by means of a differential pumping system. Gas pulses composed of 1% O₂ balanced in the rest of argon (Ar) are jetted on the target surface at a frequency of 4 Hz. Meanwhile, electrical pulses of negative peak voltage in the range of 800 – 1000 V with are applied to the target with the same frequency as that of the gas pulses. The width of the electric pulses is 70 μs. The electric pulses are made to have a 650-μs delay relative to the gas pulses. During the process, the rod target is being rotated to ensure the micro-plasmas can be generated evenly on its surface. Zn atoms are ablated from the metal target. Some of these atoms re-condense to form nano-sized



clusters.

The nanoclusters are carried to move by the gas. At the region close to an exit, the gas and the nanoclusters are extracted to leave the chamber and enter the expansion chamber. The expansion chamber is pumped down to rough vacuum at a pressure of around 300 mTorr by means of a booster pump backed with a mechanical pump of a large pumping rate. The carrier gas experiences a notable pressure drop and goes through an expansion. It is then re-contracted to converge towards the axis of a set of aerodynamic lenses. A narrow streamline is formed. The nanoclusters are carried to move forward in the same direction. They are further entrained to become a fine beam of nanoclusters. The aerodynamic lenses also have a function of filtering out the nanoclusters of similar masses and hence their sizes are controlled to fall into a narrow range.

The nanoclusters finally leave the expansion chamber and enter a deposition chamber. This chamber is pumped down with a turbomolecular pump to reach a base pressure of 2×10^{-6} Torr. The nanoclusters are deposited on a (100) single crystal silicon wafer or Corning 7059 glass substrate. The substrate is cut to have a dimension of 10mm x 5mm x 1mm. The nanoclusters move with a very low kinetic energy, which is far below the thermal energy, such that the shape of the nanoclusters is retained after reaching the substrate. The substrate is at ambient temperature, so that no significant diffusion of atoms is incurred. As a consequence, the deposits are found to constructed of nanoclusters with the shape as they land. The film sample thus has a specific highly porous structure with a very rough surface. The effective surface area of the film is considered to be very large and serves to be the gas-solid interface for

the gas sensing reaction to occur.

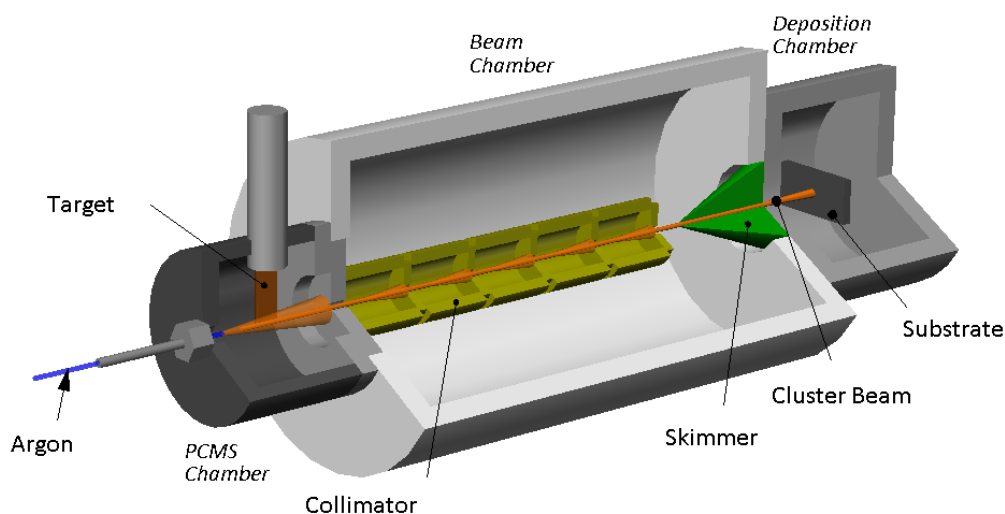


Figure 3.1 Schematic diagram of the configuration of a Supersonic Cluster Beam Deposition (SCBD) system.

The average size of nanoclusters is considered to be one of the most important parameters affecting the gas sensing properties, and hence is particularly concerned in this project. The nanocluster size produced in SCBD process varies with the settings of processing parameters. The formation of the nanoclusters in SCBD is based on the bombardments of Ar ions in the microplasma pulses on the cathode target. The energy and momentum transfer of the Ar ions bombarding on the target is expected to affect the size of the nanoclusters. Its dependence on the setting of the power used in maintaining the microplasma was investigated.

Figure 3.2 illustrates the physical process of ion bombards on the target surface.



When a particle bombards on the target surface, based on the principle of conservation of energy, the total energy and momentum in the process remain unchanged. The average kinetic energy gained by argon ions, ΔE_{Ar} , is the sum of kinetic energy of the gas and electrical potential energy due to the attraction by the cathode:

$$\Delta E_{Ar} = \frac{3PV}{2n} + qV_E \text{-----(3.1)}$$

where P , V and n are pressure, volume and number concentration of particles in space. This formula predicts that the average kinetic energy of sputtered nanoclusters would decrease if the pressure and voltage drop. Hence, pressure P is required to keep at a high level to ensure that the nanoclusters are fast enough to realize the supersonic expansion process. The allowed variable range of P is narrow. Only the applied voltage V_E can be used to adjust the size of nanoclusters. Figure 3.3 shows the AFM images of as-deposited Zn nanoclusters produced with applied peak voltage of -800 V. The average size of nanoclusters achieved is found to be 76 nm.

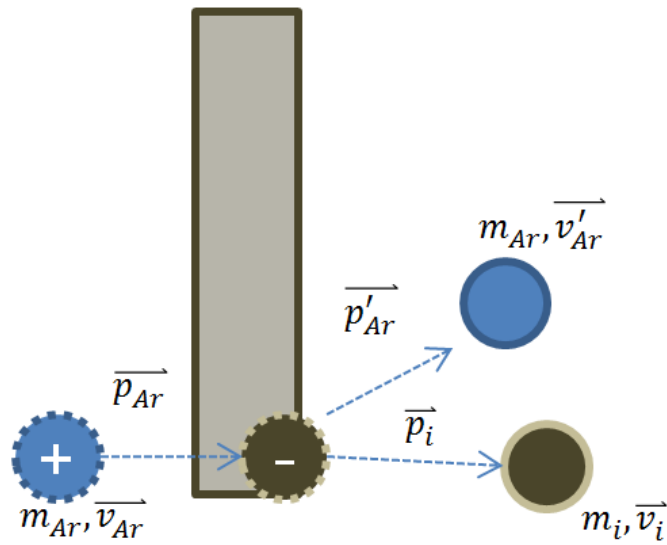


Figure 3.2 Bombardment of the target by accelerated Ar ions

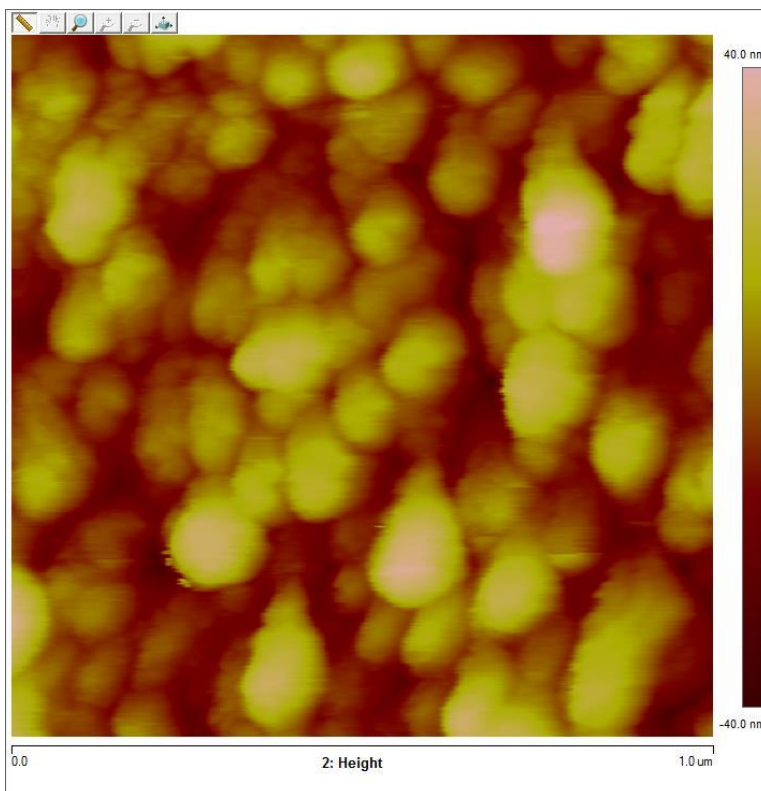


Figure 3.3 AFM image of nanocluster SCBD Zn film prepared at a discharge voltage of -800V.



3.1.2 Post annealing

Since SCBD is a low energy and low temperature deposition process, the nanoclusters are loosely connected. Their contact points mainly involve weak van der Waals force. The crystallization of individual clusters are poor. Post-annealing of metal-oxide films is thereby necessary to improve the crystallinity of the nanoclusters and the junctions. This may help to improve the robustness of the film structure and may also help to improve the gas sensing properties of the film. In this study, the photo-assisted gas sensing response is most concerned. Only a semiconductor oxide with some degree of crystallization can exhibit notable photoconduction effect.

The typical configuration of the facility used for post-annealing the metal films is shown in Figure 3.4. The sample was placed in a tube furnace which is O-ring sealed on both sides. A continuous flow of 200 sccm O₂ gas was admitted into the tube through an inlet. The flow rate was controlled using a mass flow controller. The pressure in the quartz tube was maintained at atmospheric pressure. Annealing temperatures of 450, 500, 550 and 600°C were used in the tests. The duration of the process was set at 30 min. The optimum post-oxidation temperature was identified to be the one leading to the best gas sensing properties.

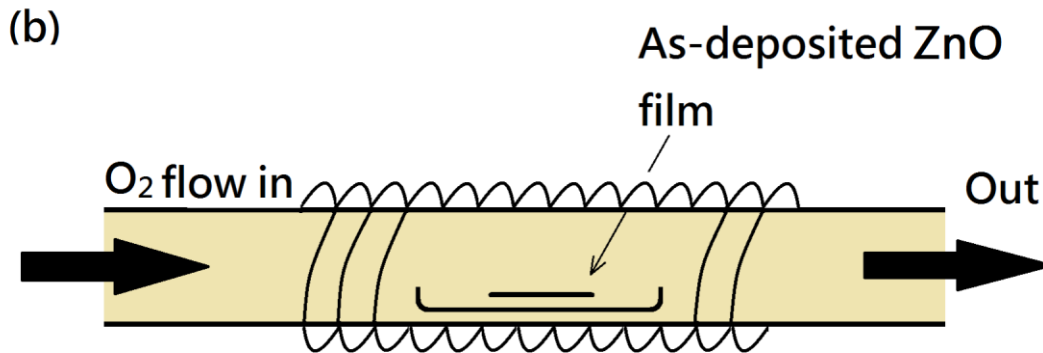


Figure 3.4 Schematic diagram of the configuration of the furnace used for post-annealing process.

3.1.3 Substrate material selection and cleaning procedure

Different substrate materials were selected for carrying out different characterization experiments and measurements. Three substrate materials can be used in our study, i.e. fused quartz, Corning 7059 glass and n-type doped (100) single crystal silicon wafer.

Insulating substrates like Corning 7059 glass slice or fused quartz plate were used for optical transmission measurements and electrical conductivity measurements. Semiconducting substrates like Si were more suitable to be used for scanning electron microscopy (SEM) analysis, X-ray diffraction (XRD) and Raman scattering experiments to prevent the interference caused by charge-up effect and background noise.

Before each run of deposition, substrates were cleaned according to the following procedures:

1. Ultrasonic cleaning in acetone for 15 min.



2. Ultrasonic cleaning in ethanol for 15 min.
3. Blow the substrate surface with pressurized dry Ar flow.

3.2 Structure and composition analyses

3.2.1 Raman spectroscopy

A micro Raman spectrometer (HORIBA Jobin Yvon HR800) was used to carry out Raman scattering experiments. It is equipped with a 50mW 488-nm diode laser. A neutral density filter of 0.6 optical density (OD) was selected for all of the tests. The detected range of Raman shift was set to be 75 - 700 cm^{-1} . A 1800 lines/mm grating was used. The system was calibrated before the start of each test by referring to the well-known characteristic Raman peak of single crystal silicon at 520.2 cm^{-1} .

3.2.2 X-ray diffractometry (XRD)

We used a 9-kW (45 kV, 200 mA) rotating target X-ray diffractometer (Rigaku SmartLab) for XRD analyses. The system is equipped with a Cu $K_{\alpha 1}$ radiation source, a parallel optics configuration. The diffracted x-ray path passed through a 0.5° parallel slit analyzer (PSA) and is detected by a NaI scintillation counter. Both theta-2 theta (θ - 2θ) scan with 2θ from 10° to 65° and glancing-angle scan were employed. The speed of scan was set at 2°/min, with a step size of 0.02°. Prior optical alignment were done before the start for each experiment.

3.2.3 Scanning electron microscopy (SEM) and Transmission electron microscopy



(TEM) analyses

Scanning electron microscope (JEOL JSM-6490) was used to examine the surface morphology of the film samples. The image gives the information related to the roughness of the film surface. Transmission electron microscopy (FEI, Tecnai G2F20) was used to investigate the granular structure of the film samples. It also provides a means for estimating the size of the nanoclusters.

3.3 O₂ gas sensing properties measurements

3.3.1 General description of the system

Photo and gas sensing response were measured using a home-made system [69] as shown in Figure 3.5. It is composed of two parts. The first one is for supplying gas flow and gas mixing. The second one is the electronic part for control and automatic collection of data.

The flow rate of the sample gas was controlled using a MKS mass flow controller (MFC) system. The pipelines of individual gases, including the carrier gas and detected gas (oxygen and hydrogen), are connected to a mixing chamber and have their own inlets. The gas flow can also direct to pass through a water chamber for altering the relative humidity of the gas. The sample gas flow is made to end up at a measurement chamber in which the sensor is located for detection. The gas flow was turned on or off using electromagnetic valves (purchased from SMC, denoted as V in Figure 3.5) and pneumatic valves (purchased from Swagelog). The system is designed to have specific ports for the use of pumping, venting and rapid purging. It is also equipped with barometers and hygrometers in some of the chambers to monitor the pressure



and relative humidity of the sample gas. In the measurement chamber, there are a sample holder equipped with a resistive heater, thermocouple for measuring the temperature of the sample, an LED light source for generating UV light to illuminate the sample and relative humidity sensor. Electrical conductivity of the sample is measured at different environmental condition. The electrical signals are passed to the electronic data acquisition system and automatically recorded with a computer.

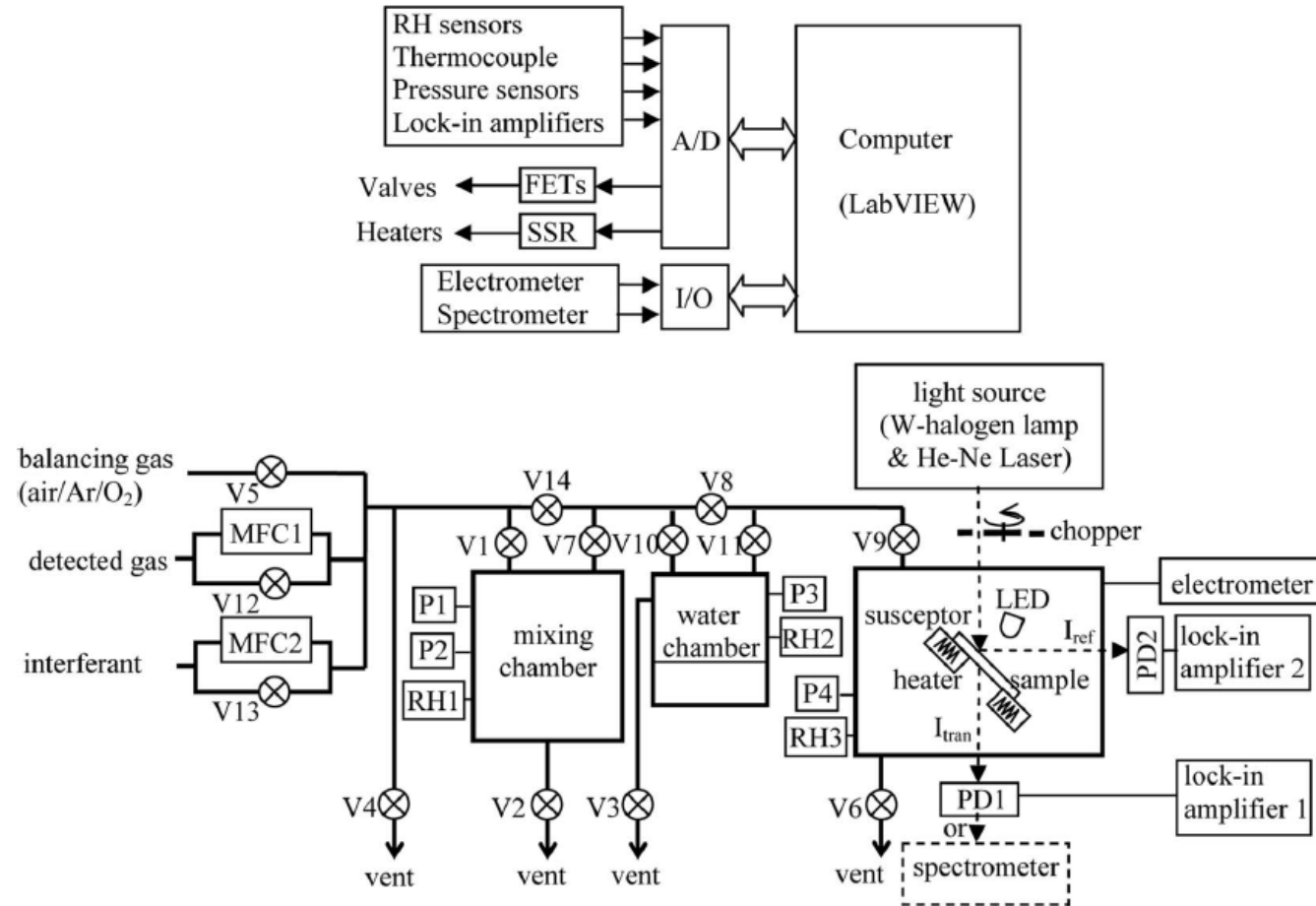


Figure 3.5 Schematic diagram showing the system used for measuring the gas sensing properties of our samples [69].



The control system is also designed to operate the valves, mass flow controllers, pressure sensors, relative humidity sensors, sample stage heater, LED and a Keithley 6517A electrometer. The central part of the control system is a computer equipped with standard interfacing devices to receive the signals from the sensors and transmit the commands to activate the above components. National Instruments Universal Serial Bus (USB) multifunctional data acquisition (DAQ) devices and General Purpose Interface Bus (GPIB) are selected to be the interfacing components. A LabVIEW program was edited for realizing the flow of all the above signals.

3.3.2 Two operation modes for gas sensing measurements

Two modes of measurements were employed for testing the gas sensing properties of the samples. They are referred to as the continuous-flow mode and gas-exchanging mode. Both of them can be conducted by using the same system.

In the continuous-flow mode, the carrier gas and the target gas are admitted into the measurement chamber with the flow rates in a ratio consistent with the target compositions in the mixture. The gas mixture flows steadily over the sample throughout the process of the test, and is released to the atmosphere through an exit. No pumping facility is used. The sample is basically at the atmospheric pressure condition. The target gas concentration can be varied from 0.1 % in a carrier gas to 100% by merely using two mass flow controllers. If even lower target gas concentration is needed, we can use a gas cylinder in which the detected has been pre-diluted to a rather low concentration. The final target gas concentration can be



lowered to reach ppb level.

In the gas-exchange mode, the measurement chamber was pumped down to vacuum first. At this stage, the valve between the measurement chamber and mixing chamber is closed. On the other hand, the balance gas and target gas are released into the mixing chamber one by one. The number of moles of each gas component is determined by respective settings of the flow rate and duration of the flow, such that the two gases are mixed with an expected molar ratio to form a sample gas. The molar ratio of the gas components is cross checked according to the partial pressures of the components measured in the mixing process by making use of a set of pressure gauges connected to the mixing chamber. Upon completion of the mixing process, the mixing chamber is slightly higher than one atmospheric pressure. The excess of pressure is adjusted to a level such that in the next step when the mixing chamber and measurement chamber are connected together, the ultimate pressure can finally be balanced at one atmospheric pressure. The next is to close the vacuum valve of the measurement chamber to cease pumping. The valve between the measurement chamber and mixing chamber is then opened. The gas in the measurement chamber is released to enter the measurement chamber. The total pressure in the enclosed volume drops to one atmospheric pressure at the end. The sensor starts to react with the target gas and generates a signal for gas detection. New testing cycle commences and measurements are repeated with the same or a new target gas concentration. Compared to the continuous-flow mode, the main advantage of the gas-exchange mode is the low consumption of the reactant gas. This advantage is particularly spectacular if some of the gas components used in the measurements are expensive.



It also helps to reduce the gas consumption when doing a prolong gas sensing experiment, like the one for examining the stability of the output signal over a long period time, or the one for checking the cyclic repeatability of the output of a sensor.

Another important advantage of this mode is that the gaseous environment in the measurement chamber can be switched from one to the other very quickly with the aid of the pumping system. The reaction between the detected gas and the sensing material can thus be switched on and off without relying on the diffusion of the gas. The changing rate of the signal can thus reflect better the real response time and recovery time of the gas sensor.

3.3.3 The gas sensor performance indexes to be examined

Sensor response is the basic performance index of a gas sensor. In this study, it is defined as the fractional change of the electrical conductivity, σ , observed during the test. we use the expression

$$S \equiv |\sigma_b - \sigma_{\text{gas}}| / \sigma_b, \text{-----(3.2)}$$

for describing the sensor response. σ_b is the value of σ measured at the background, namely air of 20.9 % of O_2 . σ_{gas} is the value of σ measured at lower oxygen concentration. It is constantly larger than σ_b . Hence, the definition ensures that S increases all the way with the drop of oxygen content, and eventually approaches to trend of $\sigma_{\text{gas}}/\sigma_b$.

The time dependence of the galvanometric response or the derived sensor response S was recorded after the sensor starts to react with the target gas. The response time T_{res} was derived from the shape of the curve. By definition, it is the



time required for the sensor to go through 80% of the total resistance change. It is not uncommon that equilibrium has not been reached within the time of the test. In such a case, curve fitting is applied to get an estimate of T_{res} . Furthermore, the saturated S is assumed to be the asymptotic limit of the fitting.

Similarly, the time dependence of S after removal of the detected gas is also recorded to calculate the recovery time T_{rec} . It is defined as the time requires for the sensor to recover 80% of the total resistance change. In particular, T_{rec} is always larger than T_{res} . Curve fitting technique is applied in the analysis to derive T_{rec} .

The stability and repeatability of the output of the sensor samples for O_2 detection were examined. Cyclic tests were most frequently used, in which the response curves detected in successive cycles are compared to check the consistency. The test requires a long running time with the aid of the automatic control and data acquisition system.

Resistance of the sensor against the interference of moisture was investigated. This is a well-known challenging problem in the field for a long time, and is considered to be one of the bottle neck problems of the development. We are only not concerned on how the sensor is affected by the presence of water vapor, but we also examined how the sensor can be protected by a super hydrophobic coating added on its surface.

We also investigated how photo assist affects the gas sensing properties of the sensor samples. In particular, we attempted to confirm whether the use of above-bandgap light illumination on the sensor can make it to work effectively at a lower temperature around the ambient one. In practice, the UV LED was used as the light source.



All the above performance indexes are functions of O_2 concentrations. The most important one is the O_2 concentration dependence of sensor response. It directly reflects how sensitive the sensor is against the change of the target gas concentration. The detection range of the sensors is also examined.

3.4 Dissolved oxygen sensing properties measurements

3.4.1 General description of the system

For examining the ability of our sensors to detect dissolved oxygen in water, we built up a system as shown in Figure 3.6 for the tests. It consists of a measurement chamber, an air intake pipe, an air outlet pipe, a polarographic dissolved oxygen sensors and a commercial immersion-type dissolved oxygen sensor. Distilled water was poured into the measurement chamber used as the electrolyte. Pure water was used to prevent the presence of any impurities to affect the result.

The procedures of the test are as follows. The first step is to open valves of the air inlet and outlet pipes. Pure O_2 gas is forced to pass through the air inlet pipe and bubbled through the distilled water. Step 2 is to wait for more than 20 minutes for the O_2 to be dissolved in the water for dissolved oxygen content to reach the saturation level. Step 3 is to close the valves of the air inlet pipe and air outlet pipe. This step takes 2 hours to ensure complete dissolution of oxygen. The polarographic dissolved oxygen sensors indicated that the composition of dissolved oxygen level in the water has reached 100%.

3.4.2 Adjustment of dissolved oxygen content in water

Further, the dissolved oxygen content can be adjusted broadly with simple procedures as follows. This function of the system is necessary for measuring the sensor response as a function of dissolved oxygen concentration. By bubbling pure N_2 gas through the water, the N_2 gas can carry some of the dissolved oxygen away from it. The amount of oxygen removed from the water is determined by the time for maintaining the flow. With this procedure, the content of dissolved oxygen can be reduced step-wise from the saturated level to approach 0, and directly read out with the Polarographic Dissolved Oxygen Sensors. The response of the sensor sample immersed in the water is recorded and analyzed. Note that more than 30 minutes should be waited every time after the dissolved oxygen level is changed.

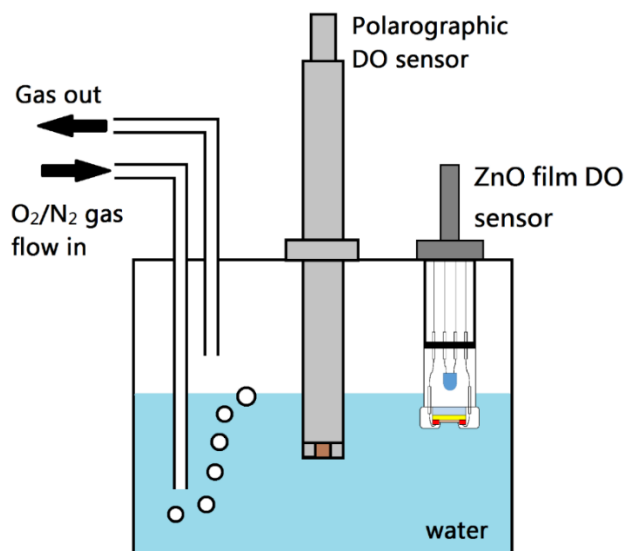


Figure 3.6 Structure of the measurement chamber used for investigating the dissolved oxygen sensing properties of the samples.



3.5 Measurements of O₂ gas and dissolved oxygen sensing properties

The Galvanometric response for O₂ gas of the sensor samples was measured using the system described in Section 3.3, and that for dissolved oxygen in water was measured using the system described in Section 4.4. More details are presented in the following.

For O₂ gas sensing measurements, the sample was placed in a stainless-steel measurement chamber at room temperature. A potential of 15 V was applied across two electrodes made on the sample surface. The electrodes were separated by a distance of ≈ 3 mm. A 365-nm and 40-mW ultraviolet (UV) LED was located on the uncoated side of the transparent Corning 7059 glass substrate. Above-bandgap light from the UV LED passed through the uncoated-side of the glass substrate to enter the film from the film-substrate interface. Photocurrent was generated in the nanostructured ZnO material, and extinguished when the light source was turned off. The real-time dynamic change of the photocurrent was recorded using the Keithley 6517A electrometer. The study went through the following stages.

- (i) SCBD ZnO film samples post-oxidized at different temperatures of 450, 500, 550 and 600°C were prepared. Their room-temperature dark electrical conductivity was measured in vacuum and in dry O₂-N₂ mixture with the O₂ concentration varying from 0 to 18%. One expects that the response of the samples at this temperature without UV assist (dark condition) is very weak.
- (ii) Room-temperature electrical conductivity of the film samples post-oxidized at above temperatures under UV assist was measured in vacuum and dry air. One



expects that a prominent photocurrent can be detected. It can be treated as the response to O_2 available at room temperature.

- (iii) The film sample exhibiting the best gas sensing properties would then be used in the following parts of the study. The corresponding post-oxidation temperature was selected for preparing other new samples. It was eventually identified to be 500°C . The study on these samples will be extended to the measurements involving the variation of O_2 gas concentration over a broad range from 0 to 18% at room-temperature. During measurement, the sample was first settled in dark until the dark current is stabilized. We then turned on the UV light and maintained the illumination on the sample for a predetermined period, and then turned it off. The real-time dynamic change of the photocurrent was recorded in the course.
- (iv) In this stage, a superhydrophobic polymer coating was fabricated on the surface of the selected film sample. This coating material is assumed to allow some oxygen molecules to pass through, denoted as being oxygen-permeable. It was fabricated using a commercial spraying cylinder, named NeverWet supplied by Rust-Oleum Corp. The product comes with two compressed spray bottles. One of them was first used to spray a polypropylene coating on the oxide film. The second one was then used to add a layer of organic solvent (containing acetone, silicones and siloxanes) on top. With the above experimental arrangement, the real-time dynamic change of the photocurrent of the film as a function of O_2 gas concentration varying from 0 – 18% in dry O_2 - N_2 mixture was detected.



- (v) In this stage, the O_2 gas sensing properties of film sensors were measured in humid gas environment. O_2 - N_2 gas mixture was bubbled through a tank containing water. The sample gas became very humid. It was then admitted into the measurement chamber. The humidity in the measurement chamber was determined to be 95%. The actual value could be even higher as the accuracy of humidity measurement was limited by the quality of the humidity sensor that we selected. The real-time dynamic change of the photocurrent in the polymer-coated SCBD ZnO film was detected again. The O_2 concentration was scanned over a range of 0 – 18%.
- (vi) For studying the dissolved oxygen sensing properties of our film samples, we designed and fabricated an immersion oxygen sensor prototype with a structure as presented in Figure 3.7. We selected the film material post-oxidized as the optimum temperature. A plastic bottle was used as the body of the sensor structure. It was made to have a hole at the bottom. The uncoated side of the Corning glass substrate was arranged to face to the hole, with the peripheral hermitically sealed with epoxy. Water was prevented from entering inside the bottle when it was immersed in water for performing measurements. UV light generated by a UV LED located inside the bottle first reached the uncoated side of the glass substrate, and then passed through it to shine on the film-substrate interface. The light continued to propagate into the oxide film. The ZnO film was directly in contact with water for reacting with the oxygen molecules. Fine copper wire feedthroughs were used to complete the electric circuit. The wires were also protected with epoxy coating. To perform

a measurement, the whole sensor was immersed into water. The oxygen content in water was varied according to the procedures described in Section 3.4.2. We also applied the method of settling the sample in dark for a long time until the dark current was stabilized. The UV light was then turned on to excite photocurrent. The real-time dynamic change of the photocurrent over a predetermined period, and that after turning off the UV light were recorded for analysis.

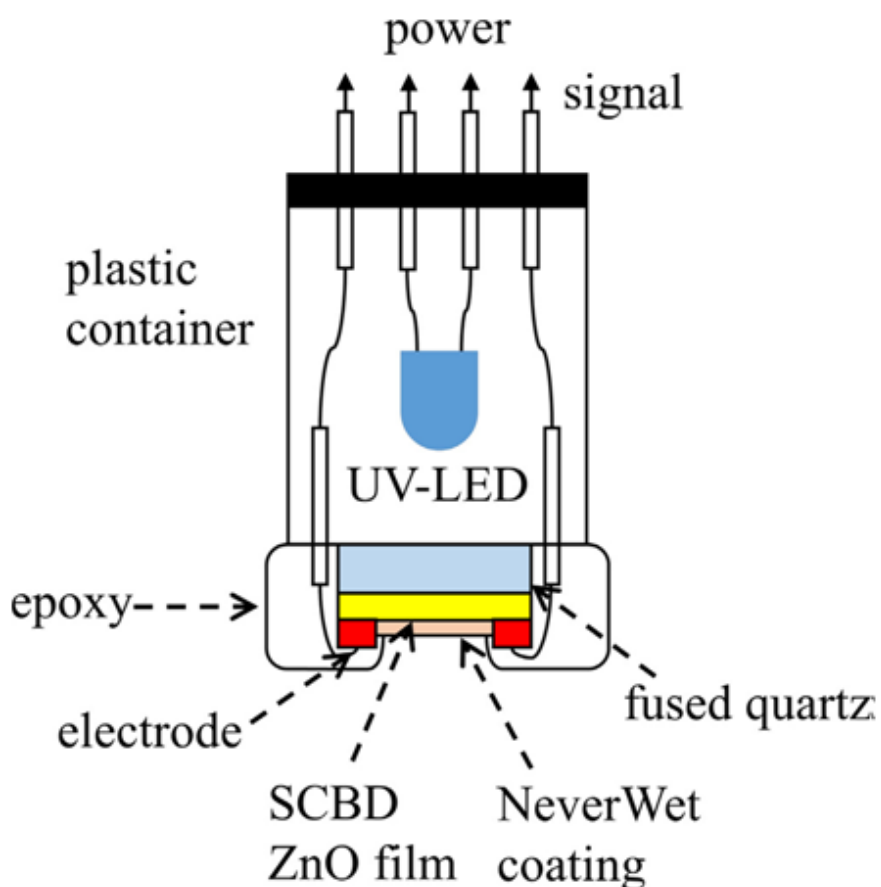


Figure 3.7 The structure of the immersion dissolved oxygen sensor prototype made of a 500°C post-oxidized SCBD ZnO film.



3.6 H₂ gas sensing properties measurements

The H₂ gas sensing properties of the film samples were measured using the system described in Section 3.3. The measurements were done at two temperatures, namely 20°C and 80°C, with and without UV light illumination, respectively. The conditions were as follows. A potential of 15 V was applied across two electrodes made on the sample surface. The electrodes were separated by a distance of ≈3 mm. A UV LED specified at giving light emission of 365 nm with a power rate of 40 mW was used as the light source. The real-time dynamic change of the resistance was recorded using a Keithley 6517A electrometer. The study was designed to have the following stages.

- (i) SCBD ZnO film samples post-oxidized at different temperatures from 450 to 600°C were prepared. Their sensor response was measured at 20°C and 80°C and at a specific H₂ concentration of 2% in air. The purpose was to find out the condition of post-oxidization with which the H₂ gas sensing properties of the film sample can be optimized. The best post-oxidizing temperature was identified to be 500°C, which was the same as that determined for O₂ sensing.
- (ii) The film samples post oxidized at 500°C were used for performing more other tests. The measurement temperature was set to be 20 and 80°C, respectively. The sensor response was recorded with H₂ concentration varying from 0.1% to 2% in air.
- (iii) The influence of relative humidity in the sample gas on the sensor response was investigated. For this purpose, the sample gas containing 2% H₂ in air was bubbled through a tank filled with water before being admitted into the



measurement chamber. The humidity was set at 0, 50 and 90% in the measurements. The difference of the results were compared and analyzed.

- (iv) The influence of UV assist on the sensor response at 2 % H₂ in air was investigated. Measurements were done with or without UV illumination, and at 20 and 80°C, respectively. Resulted obtained at these conditions were compared.
- (v) Cyclic stability of the sensor response of the film sensor at 80°C were assessed by carrying out repeated measurement cycles using 2% H₂ in air. Measurements with and without UV illumination were done for comparison.



Chapter 4 Results and Discussions for Oxygen Gas and Dissolved Oxygen Detection

Dissolved Oxygen Detection

This chapter describes the results of using SBCD ZnO film samples for oxygen detection. The change of electrical conductivity under light illumination was used as the signal of detection. The film samples without a water-proof polymer coating were used in dry air. The film samples with a water-proof polymer coating were used in dry air, humid air and water. The last case was applied for detecting the content of dissolved oxygen in water.

4.1 Structural characterization of SCBD ZnO films

4.1.1 SEM images and estimation of porosity

Figure 4.1 (a) shows the SEM image of an as-deposited SCBD ZnO film sample. It shows that the film surface is very rough. After post-oxidized at 500°C for 30 min, the film surface remains very rough as shown in Figure 4.1 (b). No appearance difference is discerned from the pictures. However, statistical analysis of the atomic force microscopy data shows that the roughness of the film drops slightly from 15.0 nm of the as-deposited state to 13.6 nm after post-oxidization.

To give a quantitative estimate of the film's porosity, we first measured the mass of the as-deposited film, m_{Zn} , with a quartz monitor installed in the deposition chamber. The film obtained at this stage is a porous metal Zn film. m_{Zn} is related to the mass thickness, τ_{m-Zn} , namely the thickness of a dense metal Zn film formed by the deposited atoms as



$$m_{Zn} = d_{Zn} \cdot (t_{m-Zn} \cdot A) \text{-----}(4.1)$$

In this formula, d_{Zn} is the density of metal zinc and A is the substrate surface area. From the measured result of m_{Zn} , the value of t_{m-Zn} was determined to be 21.2 nm. On the other hand, the actual film thickness, t_{zn} , measured using a surface profile was found to be 126 nm, which is considerably large. The porosity of the as-deposited metal film is thereby estimated to be as high as 83%.

The next is to consider the ZnO film obtained after post-oxidization. The mass of the fully oxidized film becomes

$$m_{ZnO} = m_{Zn} \cdot \frac{W_{Zn}+W_O}{W_{Zn}} = d_{Zn} \cdot (t_{m-Zn} \cdot A) \cdot \frac{W_{Zn}+W_O}{W_{Zn}} \text{-----}(4.2)$$

where W_{Zn} and W_O are the atomic mass of Zn and O atoms, respectively. The mass thickness of the ZnO film, t_{m-ZnO} , satisfies the relation

$$t_{m-ZnO} \cdot A = \frac{d_{Zn}}{d_{ZnO}} (t_{m-Zn} \cdot A) \cdot \frac{W_{Zn}+W_O}{W_{Zn}} \text{-----}(4.3)$$

$$\text{or} \quad t_{m-ZnO} = \frac{d_{Zn}}{d_{ZnO}} \cdot t_{m-Zn} \cdot \frac{W_{Zn}+W_O}{W_{Zn}} \text{-----}(4.4)$$

By putting $d_{Zn} = 7.14 \text{ g cm}^{-3}$, $d_{ZnO} = 5.605 \text{ g cm}^{-3}$, $t_{m-Zn} = 21.2 \text{ nm}$, $W_{Zn} = 65.38$ and $W_O = 16$, the value of t_{m-ZnO} is estimated to be 33.6 nm. Compared with the actual SCBD ZnO film thickness $t_{znO} = 85 \text{ nm}$ measured with a surface profiler, the porosity of the film is estimated to be 60%.

The high porosity of the SCBD ZnO is an important structural characteristic of an assemble of ZnO nanoclusters. It is further expected to give a large effective gas-solid reaction interface. This result confirms that the SCBD technique is good choice for the present study aiming at finding a material exhibiting good gas sensing effect [70,71].

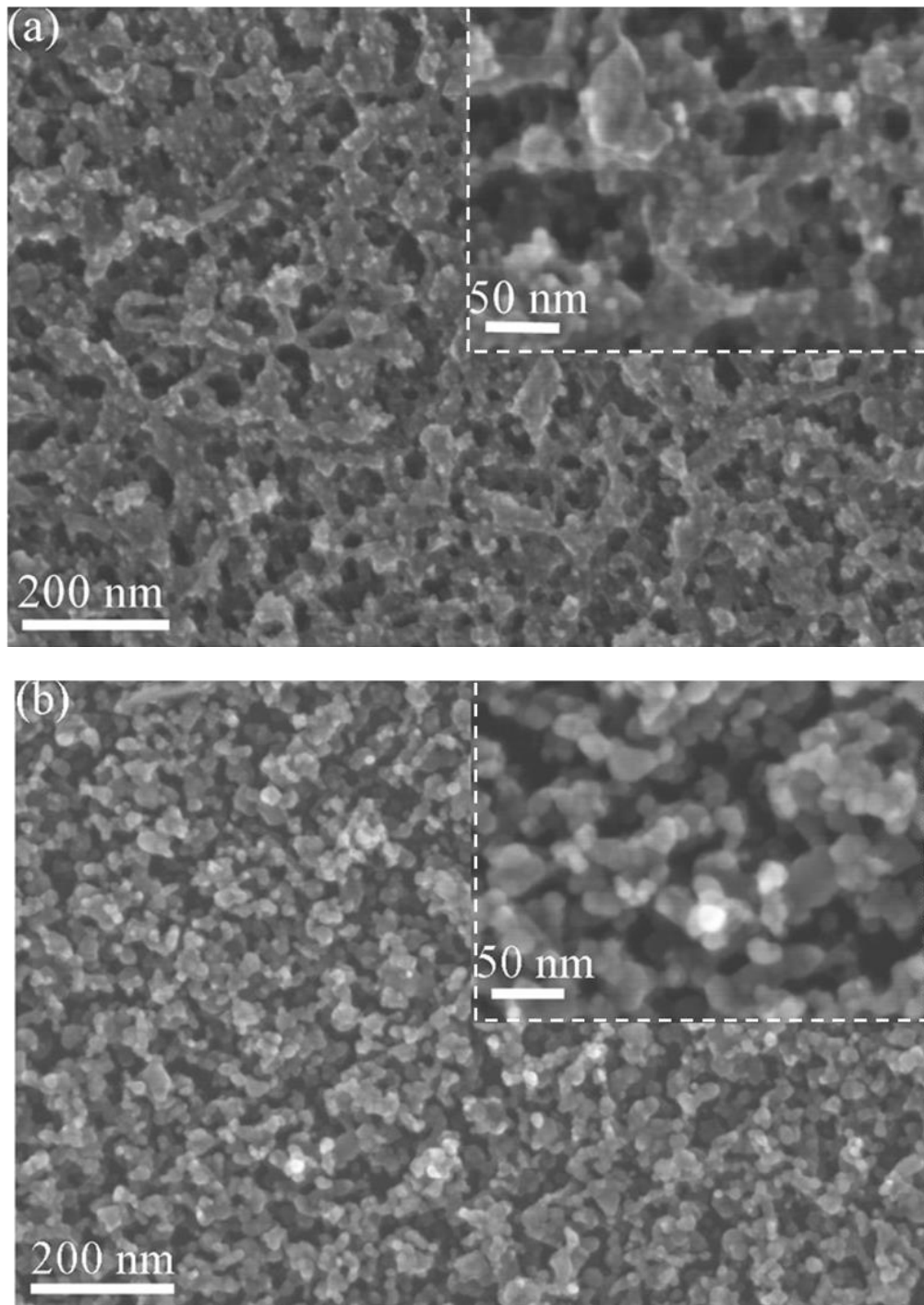


Figure 4.1 SEM images of (a) an as-deposited SCBD Zn metal film and (b) the same film after post-oxidized at 500°C for 30 min. The surface roughness is 15.0 nm and 13.6 nm for the two cases.



4.1.2 XRD diffraction and crystallization

Figure 4.2 summarizes the XRD spectra of the as-deposited ZnO film and the same film post-oxidized at different T_s ranging from 450°C to 600 °C. The 2θ scanning mode was adopted in the experiments.

First, the XRD spectrum of the as-deposited film does not contain any diffraction peaks associated with the characteristic peaks of both metal Zn and ZnO. Hence, the as-deposited material should be in amorphous state. It is known that the material is mainly metal Zn in nanocluster shape, this observation suggests that the Zn clusters are not crystallized.

On the other hand, the spectra of all samples post-oxidized at temperatures at or above 450°C show peaks. They match quite well with the peak positions of the (100), (002) (101), (110), (103), (200) and (112) planes of crystalline ZnO, suggesting that ZnO phase is formed. The intensity increases most significantly in the temperature range from 450 to 550°C, and then further increases mildly at higher temperatures, showing the grains are formed and grow mainly in this temperature range. The connection between adjacent nanoclusters is thereby enhanced. The drift mobility of the charge carriers increases such that they can transport more readily in the solid. The overall electrical conductivity is increased as a consequence.

It is noted that a small peak appears at $2\theta \approx 52^\circ$. It does not match with any characteristic peak of Zn and ZnO. To identify its origin, an XRD experiment was done on a bare Si(100) substrate using the same glancing angle. We found that when the orientation of the Si substrate about the axis normal to sample stage, specified with angle ϕ , was set to fall into a specific range with a width of $\pm 1.5^\circ$, a small peak would



appear at that position in the spectrum. It diminishes when ϕ is set to leave this range. According to the powder diffraction data, we suggest that the peak should originate from the (321) and (311) planes of Si or unknown defects. It is neither related to the lattice structure of Zn nor that of ZnO.

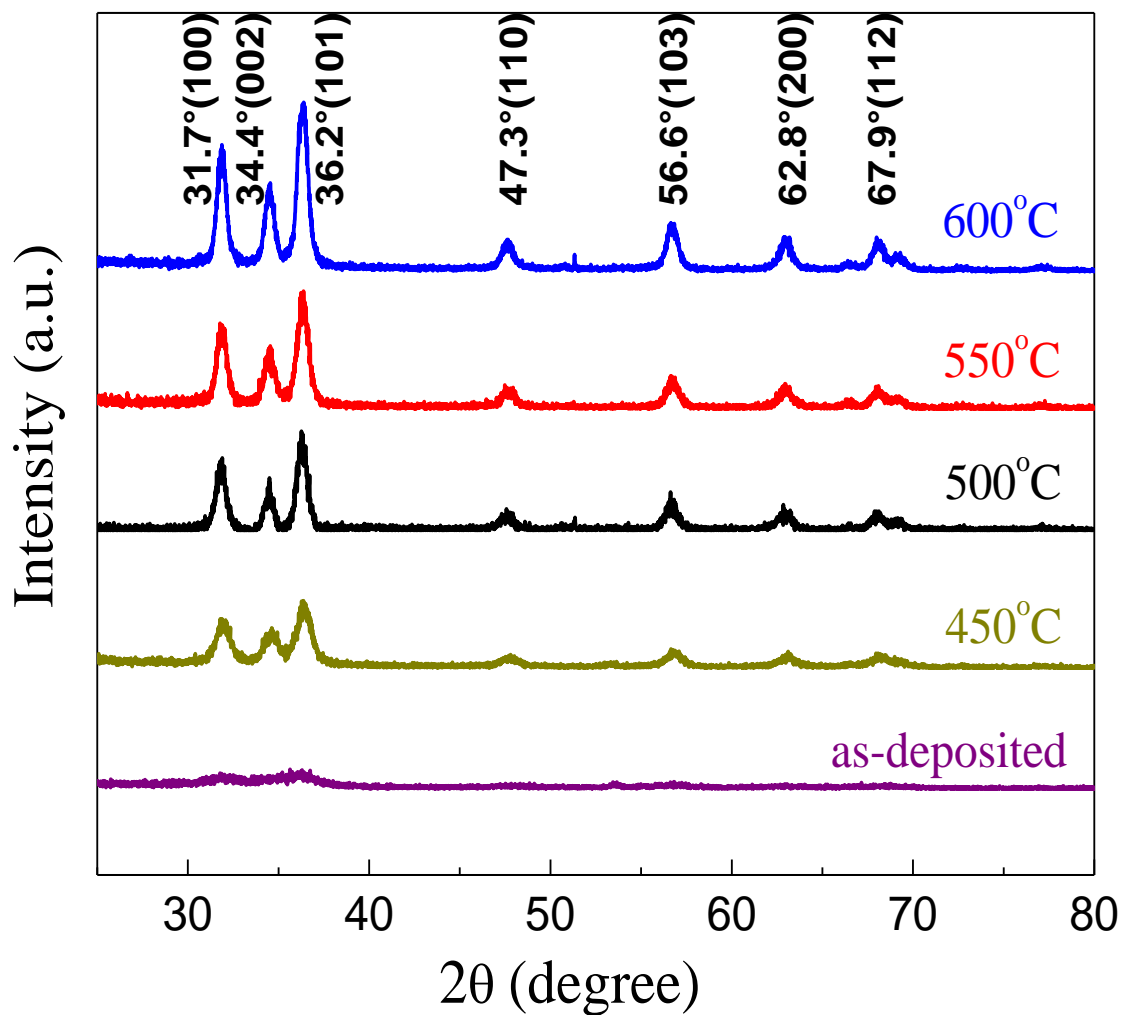


Figure 4.2 XRD spectra of the as-deposited SCBD ZnO film and the film after post-oxidized at 450, 500, 550 and 600°C.



4.1.3 Raman scattering analysis

Figure 4.3 shows the Raman spectra of fused quartz, as-deposited SCBD ZnO film and the film after post-oxidized at 450, 500, 550 and 600°C. The spectrum of fused quartz is the reference. The ZnO film at both as-deposited condition and after post-oxidized at the above temperatures does not show any Raman peak like fused quartz. For this result, we do not use the Raman spectra of the SCBD ZnO film in the structural analysis.

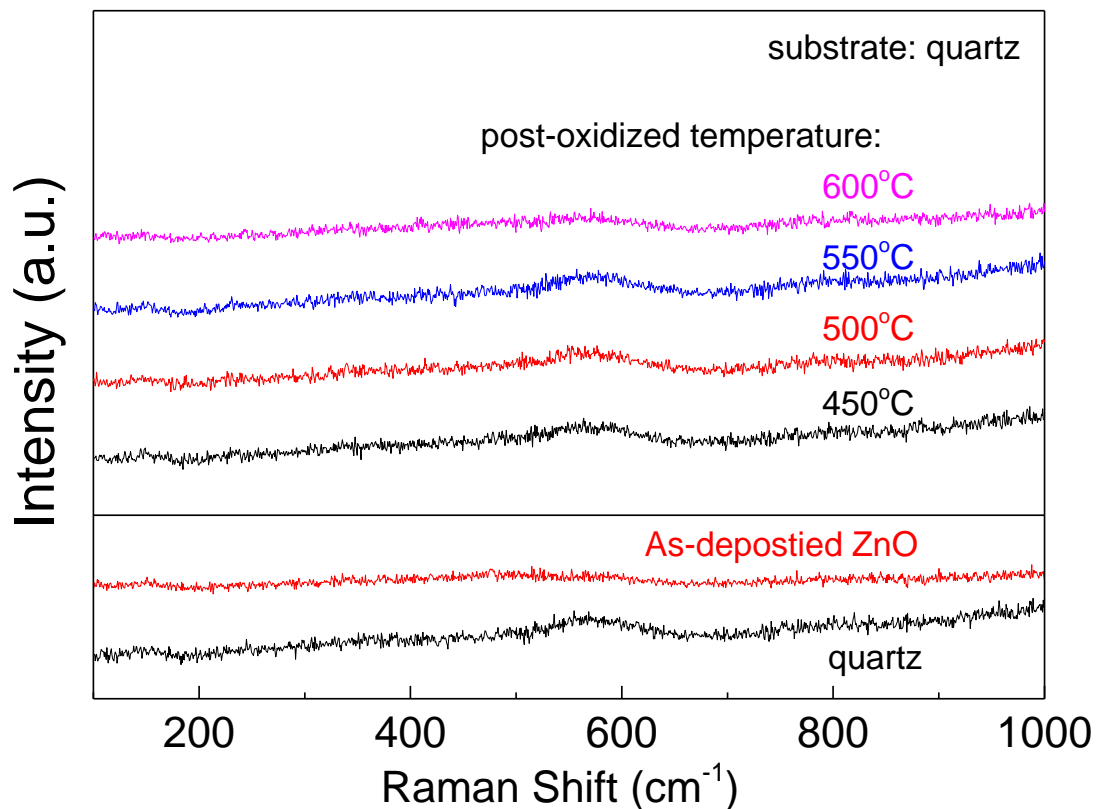


Figure 4.3 Raman spectra of quartz, as-deposited SCBD ZnO film and the film after post-oxidized at 450, 500, 550 and 600°C.



4.1.4 Cross section structure of TEM

The cross section TEM image of the 500°C post-oxidized ns-ZnO film as shown in Figure 4.4a confirms that the film is composed of loosely connected nanoclusters with diameter in the range of 10-15 nm. Nano sized pores and voids are clearly seen in the intra-cluster regions. High resolution TEM image (Figure 4.4b) further reveals the single-crystal structure of the annealed clusters. The lattice spacing is determined to be 0.258 nm, which is consistent with the d-spacing of (0002) lattice planes of hexagonal ZnO and agrees well with the XRD result. Now, we assert that the annealed ns-ZnO film is highly porous and composed loosely connected 13-nm grains. Such a structure is expected to show fast and strong resistive response to gas due to fast diffusion of gas into the film and large surface-to-volume ratio of tiny nanoclusters.

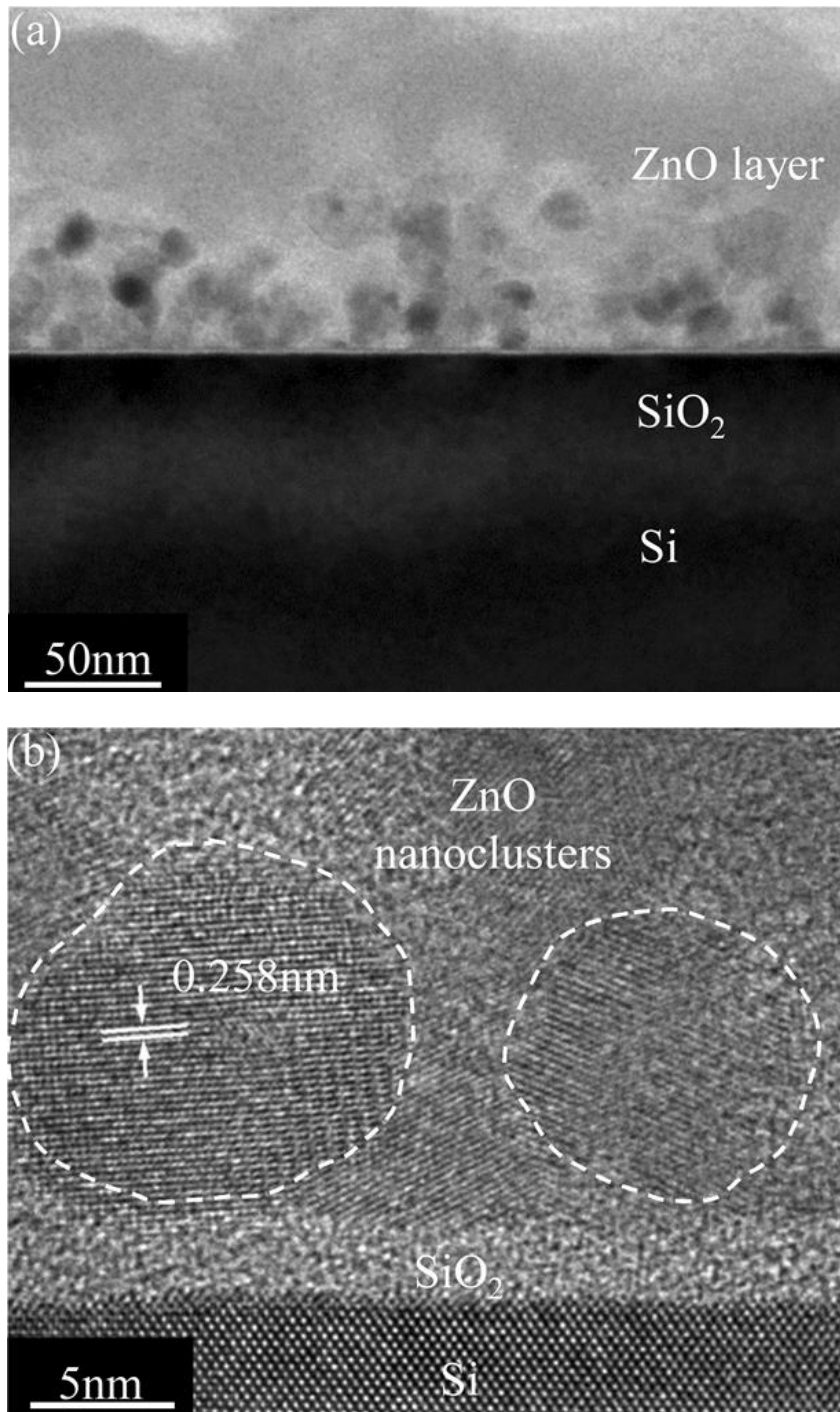


Figure 4.4 Cross sectional TEM images of 500°C annealed SCBD ZnO film.



4.2 Selection of optimum post-oxidizing condition for making O₂ sensors

4.2.1 Dark electrical conductivity of SCBD ZnO films post-oxidized at different temperatures

Before systematic study of the oxygen sensing properties of SCBD ZnO films, we need to determine the optimum post-oxidation temperature for achieving suitable sample for the tests. The selected condition is the one for producing films of largest and repeatable resistive response to oxygen. It would then be used for making more samples for the study of gas sensing. For comparing the gas sensing property of the films, we referred to their real-time dependence of dark and UV-assisted electrical conductivity measured at room-temperature.

Figure 4.5 shows that the room-temperature dark electrical conductivity of SCBD ZnO films post-oxidized at temperatures varied in the range from 450°C to 600°C. Results show that the film resistance does not change when the gaseous environment is switched between vacuum and one atmospheric pressure of O₂-N₂ admixture with the O₂ content varied in the range of 0 to 18%.

All the detected values of electrical conductivity are high enough and readily measured with an electrometer. Their null response to oxygen is attributed to the strong surface sorption of oxygen species, it could be due to the deep traps which compensate the free carrier in the conduction. Their concentration is rather stable and does not change with the variation of the surrounding oxygen concentration. The charge carrier concentration in the solid is fixed. Though the drift mobility may have a little change with the gas concentration, the dark electrical conductivity is stabilized and does not change with the O₂ content.

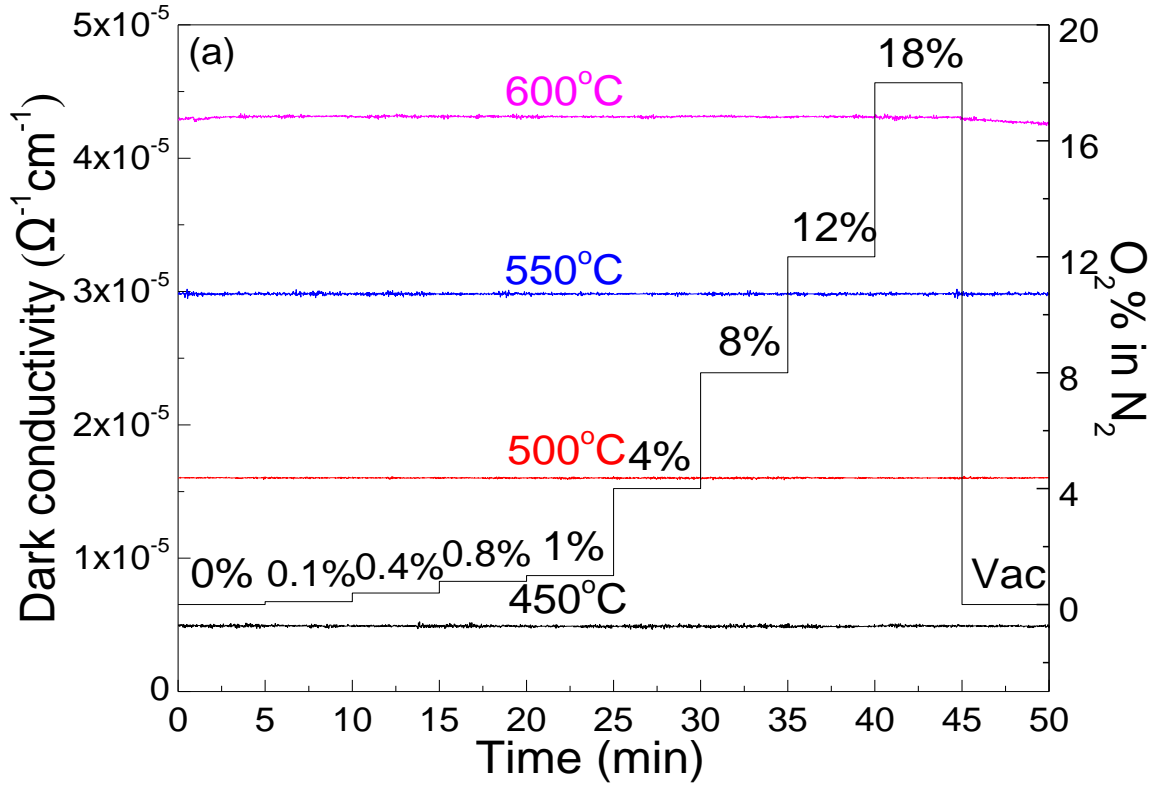


Figure 4.5 Room-temperature dark electrical conductivity of SCBD ZnO films post-oxidized at 450°C to 600°C in 0-18% O₂-N₂ and vacuum.



4.2.2 UV-assisted electrical conductivity of SCBD films post-oxidized at different temperatures

The next step is to investigate real-time dependence of the room-temperature photo assisted electrical conductivity, σ_{photo} , of the film samples in vacuum. The films post-oxidized at 450, 500, 550 and 600°C were measured.

Results are shown in Figure 4.6. One immediately sees that the curves exhibit some common features. Each of the curve rises immediately after UV light is turned on and, keeps rising as if trying to approach some asymptotic value. When the UV light is turned off, the curve starts to drop and tends to return to the dark electrical conductivity. From these features, one can derive a set of parameters by curve fitting. They include the asymptotic value of photo assisted electrical conductivity; response time and decay time. These parameters are useable to specify the photo assisted electrical conductivity of the films.

Importantly, post-oxidation temperature is found to affect the photo-assisted electrical conductivity significantly. For example, the photo-assisted electrical conductivity of the film post-oxidized 450°C (lowest value used) increased by more than 10^5 times compared to the level in dark at the end of the measurement. It still keeps rising just before turning off the light at a time 1400 min after commencement of the measurements. Equilibrium has not been reached at this moment. Immediately after turning off the light, the electrical conductivity starts to drop and experiences a long-lasting decaying process. In fact, the current cannot return to the original value measured in dark even at a time more than 20 hours after turning off the light.



The prolong evolution and recovery of electrical conductivity approaching respective limits are attributed to the poor crystallization of the film. It leads to the presence of a large amount of defect states in the sample. Under light illumination, some amount of photo electrons are generated in the nanoclusters. In vacuum, some of these electrons can transport in the conduction band and contribute to the increase in electrical conductivity. Some of them could be trapped by the defect states, and may be re-excited to the conduction band, or hop across the defect states via tunneling effect, or recombine and annihilate with holes. Due to the low mobility of the charge carries, the distribution of electrons in all the above states requires a considerable long period of time to reach equilibrium. This explains the observed the long-lasting evolution of photo assisted electrical conductivity. The reverse argument associated with the recombination of photo generated charge carriers after turning off the light is used to explain the long-lasting decaying process of electrical conductivity.

With increasing post-oxidization temperature, crystallization of the film material is enhanced. The film structure would have less defects. Charge carriers transport with larger mobilities, and hence equilibrium of distribution in different states can be reached with a faster rate. The real-time dependence of the electrical conductivity would exhibit shorter response and decay times. Because of less defect states, less total electron concentration participates in the transport processes. Particularly, the concentration of defect states becomes small and can only accommodate a less amount of charge carriers. The contribution of hopping to electrical conductivity is



less and hence the electrical conductivity under light assist is expected to saturate at a lower value.

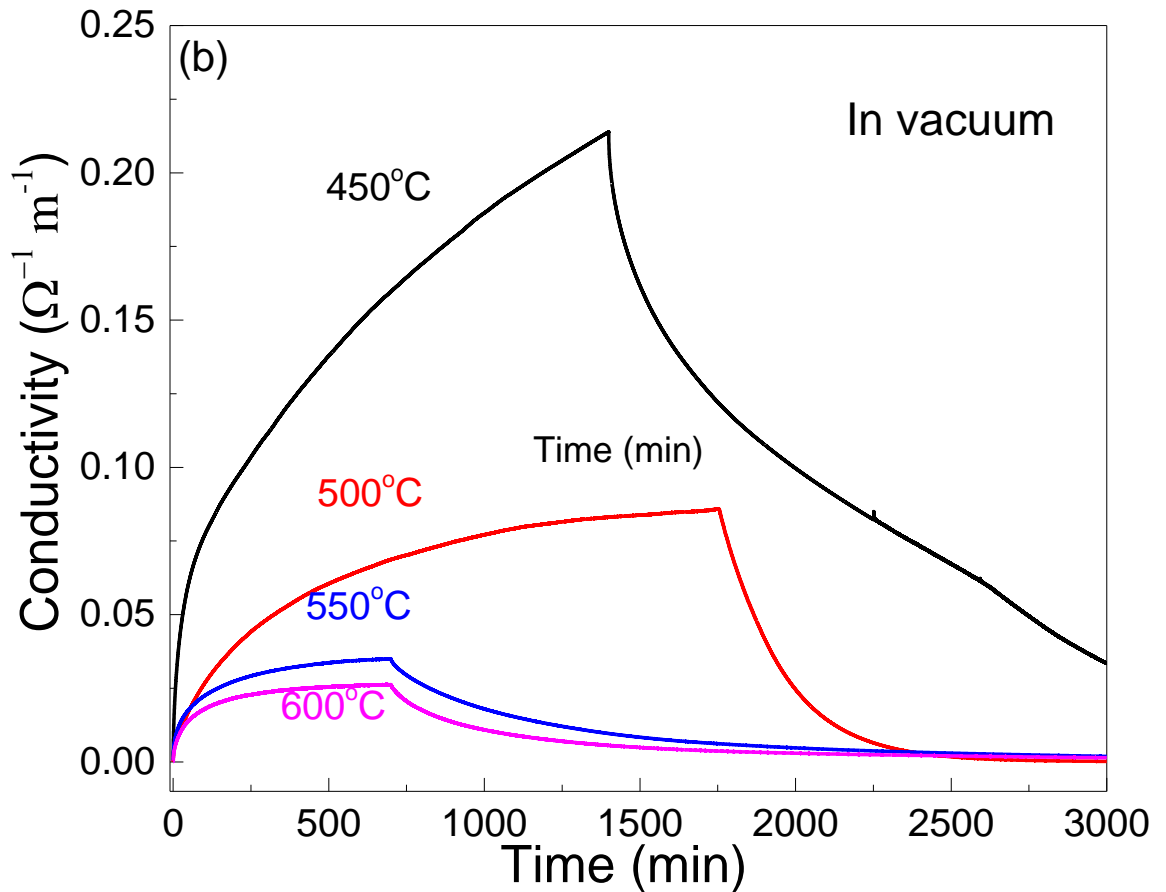


Figure 4.6 Room-temperature photo-assisted electrical conductivity of SCBD ZnO films post-oxidized at 450, 500, 550 and 600°C measured in vacuum.

The next step is to investigate the real-time dependence of light assisted room-temperature electrical conductivity of the film samples measured in dry air with an O_2 concentration of 20.95%. The films are post-oxidized at temperatures varied in the range from 450°C to 600°C.



Results are shown in Figure 4.7. Some important features are found as follows. First, the light-assisted electrical conductivity measured in the presence of oxygen gas is always smaller than that measured in vacuum. The drop is more significant when oxygen content increases. As an example, the asymptotic saturated photo-assisted current of the 450°C-oxidized films measured in vacuum is 10^5 times higher than the dark current; and the value measured in 18%-O₂ in N₂ is 200 times higher than the dark current. This result confirms that the real-time dependence of room-temperature photo assisted electrical conductivity of SCBD ZnO film can be used as an effective physical property for oxygen detection.

Second, the response and decay times become shorter with increasing oxygen content in the environment, confirming that the variation of the shape of the curve contains information on the dynamics of the interaction between the solid and the gas.

Third, the photo assisted response to oxygen inspires us to propose a dynamic model as that published in Refs. 72 and 73. It suggests that above-bandgap photons shining on an MO_x material can generate electron-hole pairs. Some photo generated electrons interact with some oxygen species which are originally chemisorbed on the oxide surface in dark, causing them to desorb. On the other hand, the photo generated electrons can attract some other oxygen molecules from the surrounding. This group of oxygen species has lower adsorption energy and is more dynamic in responding to the variation of the surrounding oxygen concentration. This change occurs at room-temperature, hence the MO_x film becomes an effective oxygen sensing element without using a high operating temperature. The drawbacks of a



conventional MO_x -based oxygen sensor working at a high temperature can be prevented.

Moreover, both in dark and in O_2 -containing environment, the photo assisted current of the sample post-oxidized at the lowest post oxidization temperature of 450°C is the largest. We suggest that this film has not been well crystallized. Hence, the film has a larger defect concentration and lower drift mobility of the charge carriers. It takes a longer time to reach equilibrium in a dynamic process. Consequently, both reaction and recovery times are long. On the other hand, films post-oxidized at higher temperatures, namely above 450°C , are more crystallized. They should have smaller defect concentration and the charge carriers in the films are more mobile. As a result, recombination rate of excessive electrons and holes via band-to-band transition is faster. This imposes some limit to the excessive photo generated electron and hole concentrations. The overall photo assisted electrical response to oxygen becomes less pronounced as seen in Figure 4.7.

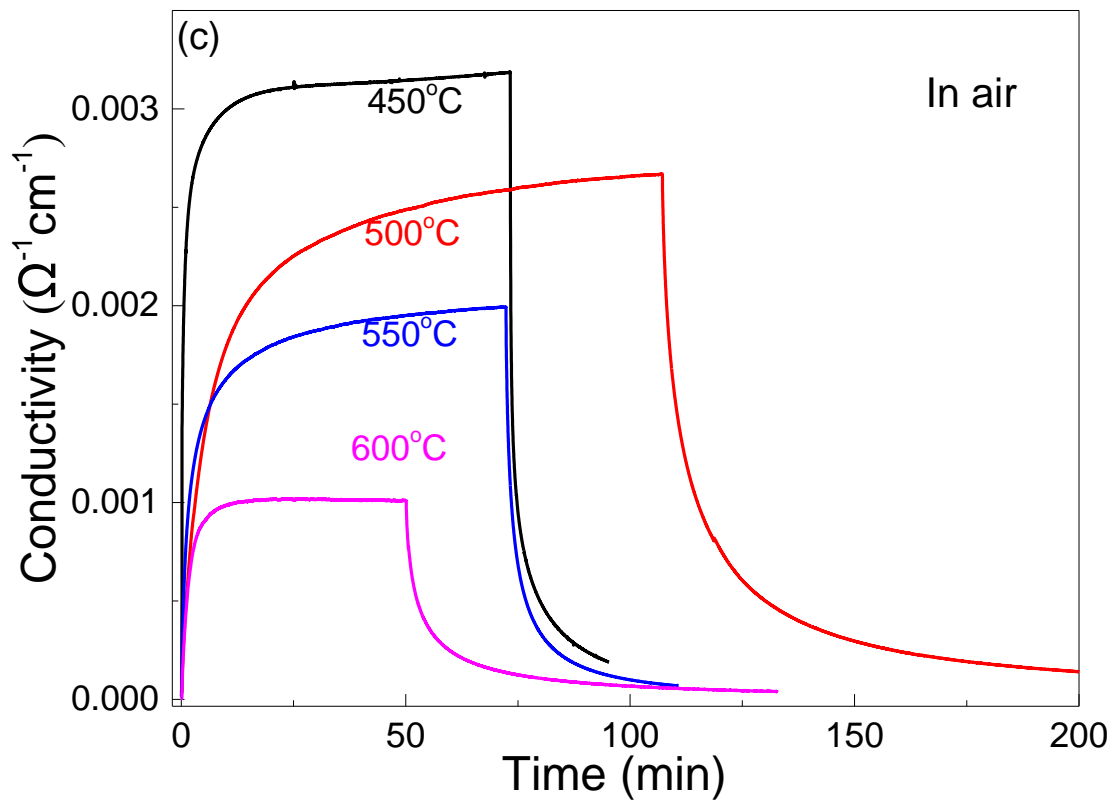


Figure 4.7 Room-temperature photo-assisted electrical conductivity of SCBD ZnO films post-oxidized at 450, 500, 550 and 600°C measured in air.



4.2.3 Determination of optimum post-oxidation temperature based on stability tests

The above results confirm that the films exhibit good photo assisted electrical response to oxygen. We further proceeded to examine the cyclic stability of the oxygen sensing response of the film samples post-oxidized at 450°C and 500°C to see which condition would be more suitable for the use of making oxygen film sensors for more detailed study on the gas sensing effect.

The tests were done in air. It is designed to conduct as follows. With the sample placed in a steady flow of air, UV light was turned on and off for ten cycles. Meanwhile, the real-time dependence of the current passing through the sample under a voltage bias was recorded. Results of the tests are shown in Figure 4.8. One sees that the 450°C-oxidized sample exhibited stronger current response, but the signal was less stable compared to that of the 500°C post-oxidized film. The peak value of the former detected in successive cycles kept increasing slightly. Upon completion of ten cycles, the peak value of electrical conductivity has increased by a total of 24%, showing that the cyclic stability of the 450°C-oxidized sample to oxygen is not quite satisfactory. On the contrary, the peak value of the photo assisted electrical resistivity of the 500°C-oxidized film sample detected in ten cycles only varied by 4%, suggesting that the cycle stability of the gas sensing properties of the film is more stable. Although the films oxidized at even higher temperatures would exhibit similar or even better stability, but the magnitude of sensing response becomes smaller as indicated in Figure 4.7. This result is understandable considering that the film structure after going through a higher temperature treatment should be more stable, and hence the



gas sensing properties is more repeatable in a cyclic operation. The reduction of the resistive response with increasing post-oxidizing temperature may be associated with the enhanced crystallization of the material structure. Based on these observations, we suggest that the 500°C post-oxidized film gives a good compromise between the sensing response and stability for the use in oxygen sensing application.

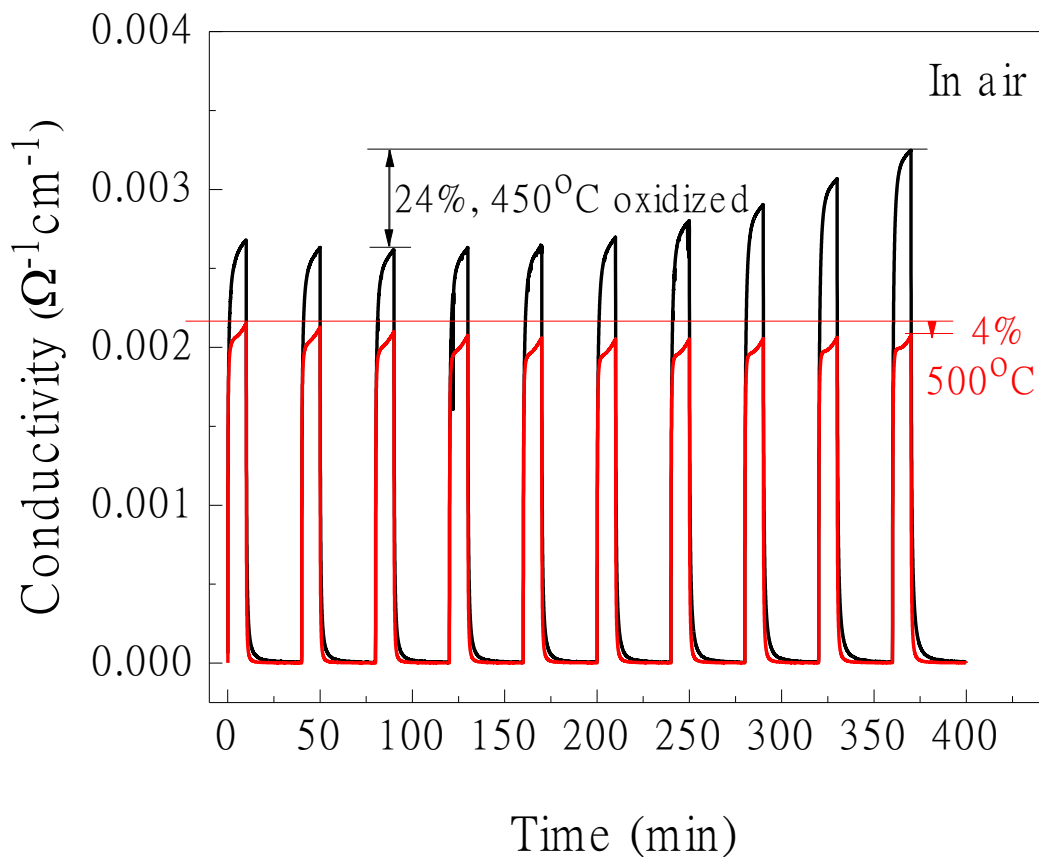


Figure 4.8 Room-temperature photo assisted electrical conductivity of 450°C- and 500°C-post oxidized SCBD ZnO films measured in cyclic tests in air.



4.3 Oxygen sensing effect of uncoated 500°C-post-oxidized SCBD ZnO films in dry gaseous environment

After deciding to use the 500°C-oxidized film sample for detailed study of gas sensing effect, in the first stage we investigated its real-time dependence of room-temperature photo-assisted electrical conductivity in vacuum and dry gaseous environment with the O₂ concentration varied over the range from 0 to 18% balanced in Ar. The test was designed to place the film in a steady gas flow first, and then to switch on the UV light for a predetermined period, and then switch off the UV light. Measurements were done throughout the course.

Results are shown in Figure 4.9. We first notice that though oxygen gas is absence in the measurements conducted in pure N₂ gas and vacuum environment, results obtained are found not exactly the same. However, there should have no significant difference in physiochemical condition in the two cases, and hence they should exhibit some common features mainly originating from UV light illumination. In particular, after UV light is turned on, the electrical conductivity rises monotonically with a faster initial rate, and then slows down as time proceeds. It has not been stabilized even at the last moment of the test. Their asymptotic limits at equilibrium can only be estimated from curve fitting for comparison. The only difference between two cases is the total ambient pressure. It is low in the vacuum-background case and is about one atmospheric pressure in the N₂-background case. In the former case, the original surface sorbed oxygen species keep being detached and removed by vacuum pump, and hence the number of charge carriers released by this group of oxygen species keeps increasing. The photo assisted electrical conductivity at all the time is



therefore higher than that of the latter case. The latter case, the detached oxygen species are not removed from the chamber and some of have the chance of being recaptured at the film surface. The change of the number of surface sorbed oxygen species is thereby partly compensated. The increase of conduction charge carriers is also less, resulting in a less comparative increase in electrical conductivity.

Now, we look at the effect of incorporating O_2 in the steady gas flow. Compared with the results obtained in vacuum background and N_2 background, after turning on the UV light, the electrical conductivity still increases monotonically, but it approaches some asymptotic limit more quickly. With increasing O_2 concentration, the time required to stabilize the response is shorter, and the asymptotic value is smaller. To interpret this result in a more physical manner, we propose that some oxygen molecules in the detected region are captured at the film surface when interacting with photo generated electrons. They replace some originally more firmly adsorbed oxygen species and adhere to the film surface with a small adsorption energy. Their concentration can vary more rapidly with the change in the O_2 concentration in the gas phase. This effect is more pronounced with the increase in the O_2 concentration in the environment. One is thereby inspired to correlate the saturated photo-assisted electrical conductivity on the O_2 gas concentration, and to use the functional relationship as the gas sensing response curve. The SCBD ZnO film is thereby an effective O_2 gas sensor workable at room temperature.

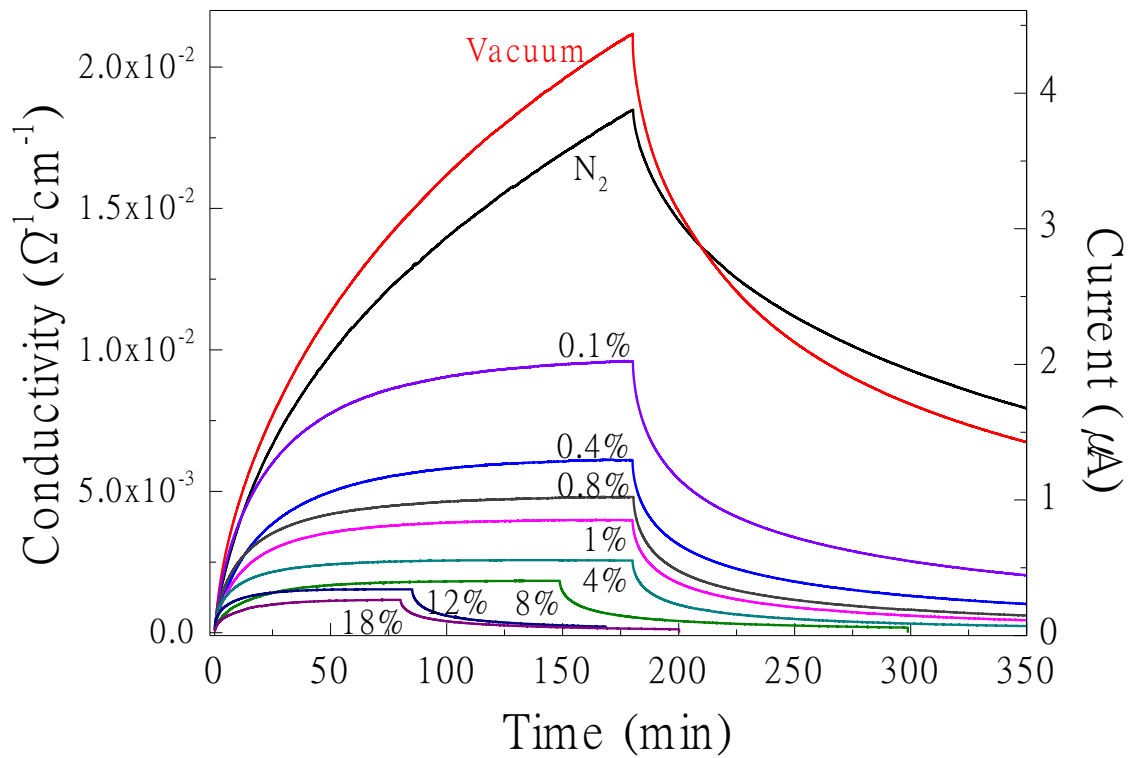


Figure 4.9 Real-time dependence of room-temperature photo assisted electrical conductivity and photocurrent of a 500°C-post oxidized SCBD ZnO film measured at O₂ concentration varied over a range from 0.1 to 18% (balanced in dry N₂).



4.4 Oxygen sensing effect of polymer-coated 500°C-post-oxidized SCBD ZnO films in dry gaseous environment

In the second stage of the gas sensing study, we investigated the real-time dependence of the room-temperature photo assisted electrical conductivity of a 500°C-post oxidized SCBD ZnO film, covered with a superhydrophobic polymer coating, placed in a dry gas flow.

We first consider the tests conducted in the absence of O₂. Two conditions were applied, namely in vacuum and N₂ background, respectively. As shown in Figure 4.10 (a), the main feature is consistent with that obtained from the tests on an uncoated film as displayed in Figure 4.9. Most of the time the value measured in vacuum is higher than that measured in N₂, though no O₂ participates in all cases. An explanation has been given in Section 4.1. However, after adding the polymer coating, the electrical conductivity is lowered by one order of magnitude.

We then consider the results of the tests obtained with the presence of O₂. In the measurements for this kind, the polymer-coated film sample was placed in a steady gas flow of O₂ content varied over a range of 0.1 and 18% balanced in dry N₂. UV light was turned on for a specific period and then turned off. The time dependence of the electrical conductivity was recorded. Results are shown in Figure 4.10 (b). Some general features are analogous to those observed for the uncoated samples. In summary, after the UV light is turned off, the photo assisted electrical conductivity rises with a faster initial rate and gradually slows down as time proceeds. It approaches an asymptotic limit with a relatively short response time, and returns to the dark value in a fairly short recovery time after the light is turned off. Moreover,



the asymptotic value is smaller as the oxygen content in the gas increases.

Though of these similarities, since the film is coated with a polymer film, additional important conclusions can be drawn. Referring to the systematic change of the response to O_2 concentration in gas, we assert that oxygen molecules can be able to permeate through the polymer coating. Also, the UV light from an LED can penetrate through the polymer coating to reach the film surface, and then generates photo induced charge carriers in the SCBD ZnO film. These properties render the SCBD film to be usable as an O_2 gas sensor based on the change of its real-time photo-assisted electrical conductivity, though the magnitude of the sensor response is usually 10 times weaker than that of an uncoated film. However, the rising rate of photo assisted electrical conductivity of the polymer-coated film is much faster, and the photocurrent is saturated in a much shorter response time, usually below 10 min.

It should be noticed that the polymer coating on the ZnO film surface is fabricated with a spraying process conducted in air. In the process, some oxygen molecules are inevitably enclosed at the interface between the SCBD ZnO film surface and the polymer coating. These excessive oxygen species also contribute to interact with the conduction electrons from the SCBD ZnO film. The presence of the polymer coating is a diffusion barrier which can significantly prohibit the trapped oxygen species to escape from the interfacial region to surrounding gaseous environment and vice versa. These trapped oxygen species can influence the response of the photocurrent as if there is a non-ignorable oxygen background. This explains why the magnitude of the photo assisted electrical conductivity of the polymer-coated sample is in general much smaller than that of a film without a polymer coating, and the sensor response



is also much lower.

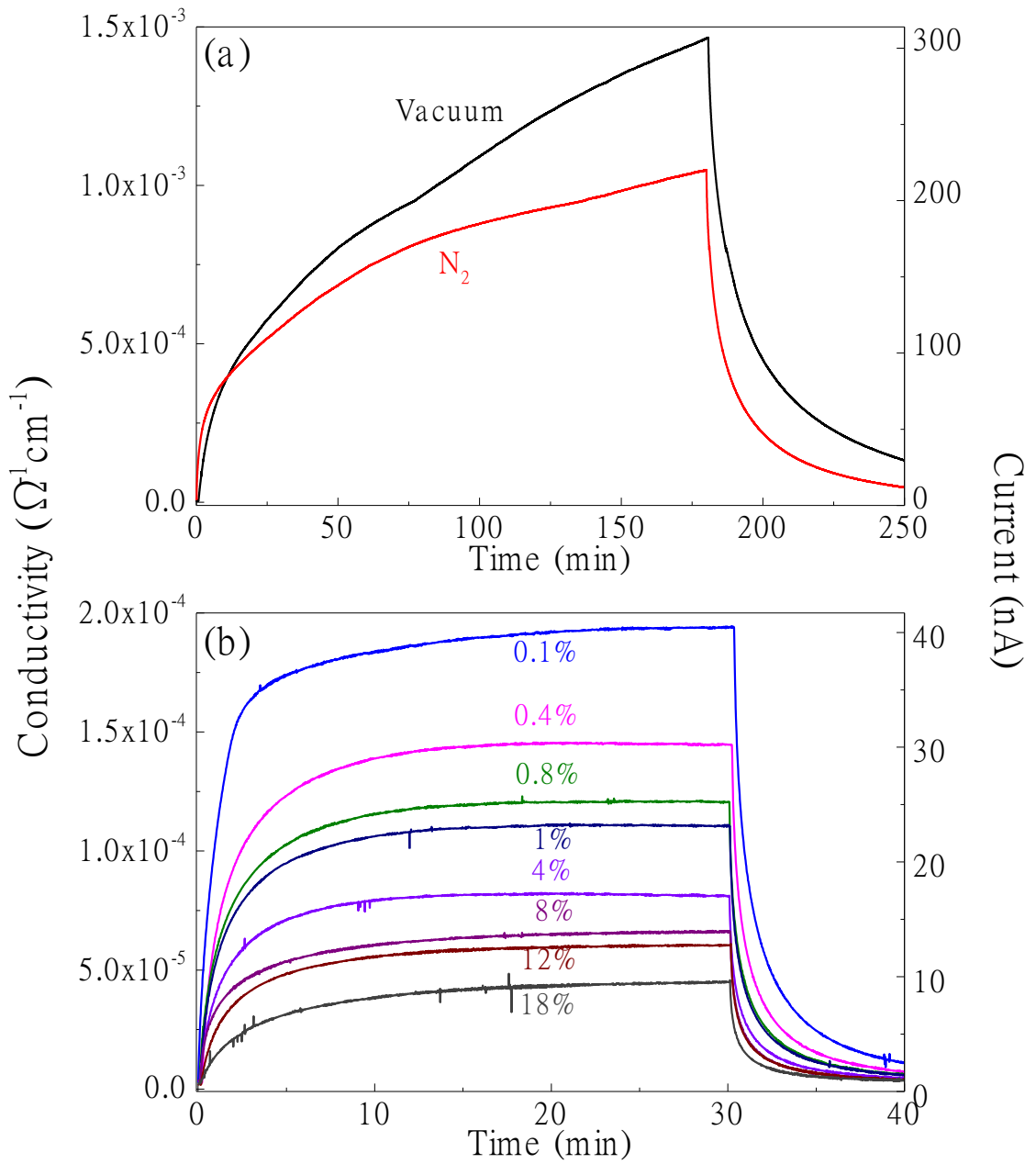


Figure 4.10 Room-temperature real-time dependence of photo assisted electrical conductivity of 500°C post-oxidized SCBD ZnO film with a superhydrophobic polymer coating in dry gas of O_2 content varied over a range from 0 to 18%.



4.5 Oxygen gas sensing effect of polymer-coated 500°C-post-oxidized SCBD ZnO films in humid gaseous environment

In the third stage of this study, we investigated the room-temperature oxygen sensing properties of the polymer-coated 500°C-post-oxidized SCBD ZnO films in humid gaseous environment. The design of the measurement process is similar to those described in the two previous stages, except that the sample gas is forced to bubble through a water tank, such that the relative humidity of the gas flow is increased to over 95%. The sample gas is a mixture of O₂ and N₂, with the oxygen concentration adjusted to vary over a range from 0.1 to 18%. With the sample placed in this steady gas flow, the UV light is turned on for a predetermined period and then turned off. Meanwhile, the time dependence of the electrical conductivity is recorded throughout the course. The focus of this part of study is to see how the film sensor response looks like if a water-proof polymer coating is added to separate the film material and a humid gas flow containing the detected component.

Results are shown in Figure 4.11. The main features of the photo-assisted electrical conductivity are similar to those observed in dry gaseous environment. It first increases with a faster initial rate and then gradually slows down to approach an asymptotic level. Compared with the same polymer-coated SBCD ZnO film operated in dry gaseous environment, this asymptotic level is around 10 times lower, and the response time required to reach this equilibrium state is about the same.

Furthermore, the saturated value of the electrical conductivity decreases monotonically with increasing O₂ concentration in the humid gaseous environment.



This suggests that O_2 can permeate through the polymer coating and causes the ZnO film to generate an electrical response to surrounding oxygen molecules.

We conclude that the polymer coating made of the NeverWet spraying product is effective in protecting the SCBD ZnO film from being deteriorated by the moisture. However, the water molecules appearing around the film surface can increase the difficulty for oxygen molecules to diffuse through the polymer coating and reach the oxygen-sensitive ZnO film. The magnitude of the electrical gas sensor response becomes weaker (compared to the case of dry gaseous environment) as a consequence.

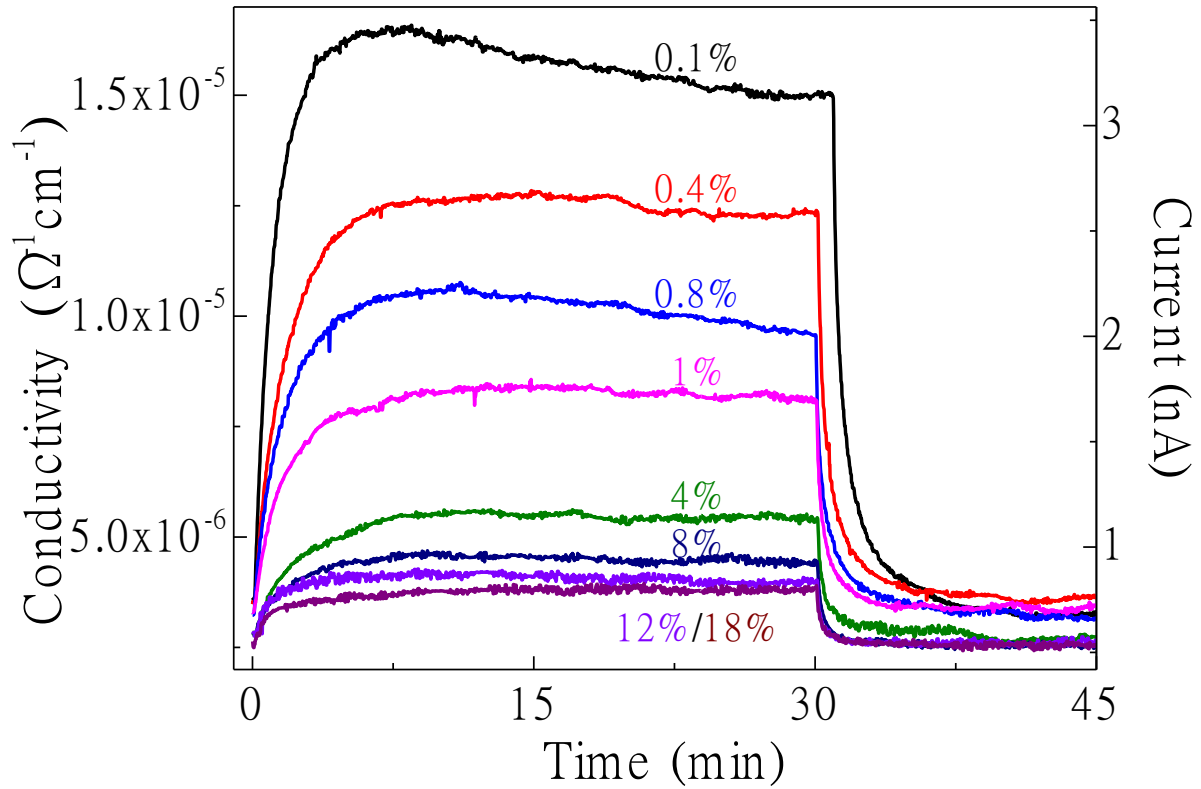


Figure 4.11 Real-time room-temperature photo-assisted electrical conductivity of an 500°C post-oxidized SCBD ZnO film covered with a superhydrophobic polymer layer measured in 95%-humid gaseous environment with O_2 concentration varied over a range of 0 to 18% balanced in N_2 .



4.6 Dissolved oxygen sensing properties of the sensors made of polymer-coated

500°C-post-oxidized SCBD ZnO films

In the fourth stage of this part of study, we fabricated an immersed O₂ sensor prototype with a structure as depicted in Figure 4.12 for examining the feasibility of applying SCBD ZnO film for detecting dissolved oxygen in water. The device has a cavity housing a UV-LED. The bottom of the cavity is sealed with a polymer-coated 500°C-post oxidized SCBD film on a fused quartz substrate. Two wires for collecting electrical response are connected to the electrodes, which are hermitically sealed with epoxy. UV light passes through the uncoated side of the substrate and reaches the film, in which photocurrent is excited. The polymer-coated film surface is in contact with water. Some O₂ molecules dissolved in the water sample pass through the polymer coating and react with the film material. An electrical response is expected to be generated.

Two pictures are captured to illustrate the important of sealing of any conducting parts and the electrodes as well from water. This is accomplished by the sealants and the polymer coating together. Good sealing prevents short circuit through water for the device to remain intact throughout the measurement process. Otherwise, the bias voltage applied across the electrodes can generate a leakage current which is large enough to damage the sensor's structure.

To carry out measurements, the device is first immersed in water inside an enclosed chamber. The polymer-coated film is in contact with water. After stabilized, the UV LED is switched on to excite a photocurrent in the SCBD ZnO film. The room-temperature real-time dependence of photo-assisted electrical conductivity of the



film is recorded, with the dissolved oxygen content in water adjusted to 0, 25, 50, 75 and 100% of the solubility of oxygen in water at 25°C. The adjustments are accomplished by bubbling an Ar gas stream through the water and releasing it to the atmosphere. The drop of the dissolved oxygen content in water is controlled according to the duration of the gas flow with the aid of an inlet valve and an outlet valve installed at the ends of the pipeline. In particular, 100% dissolved oxygen content corresponds to 258 μmol in one liter of water at room temperature. The above settings of percentages of dissolved oxygen content in water correspond to respective absolute numbers of moles of oxygen molecules in water, which when converted into oxygen content in gas phase at room temperature and one atmospheric pressure are equal to 0, 0.13, 0.27, 0.4 and 0.53% respectively. The conversion chart is also presented in the table inserted in Figure 4.12. One sees that the range of dissolved oxygen content used in this part of the study only covers a very narrow range at the lower end of the range of oxygen content conducted in gas phase involved in previous stages.

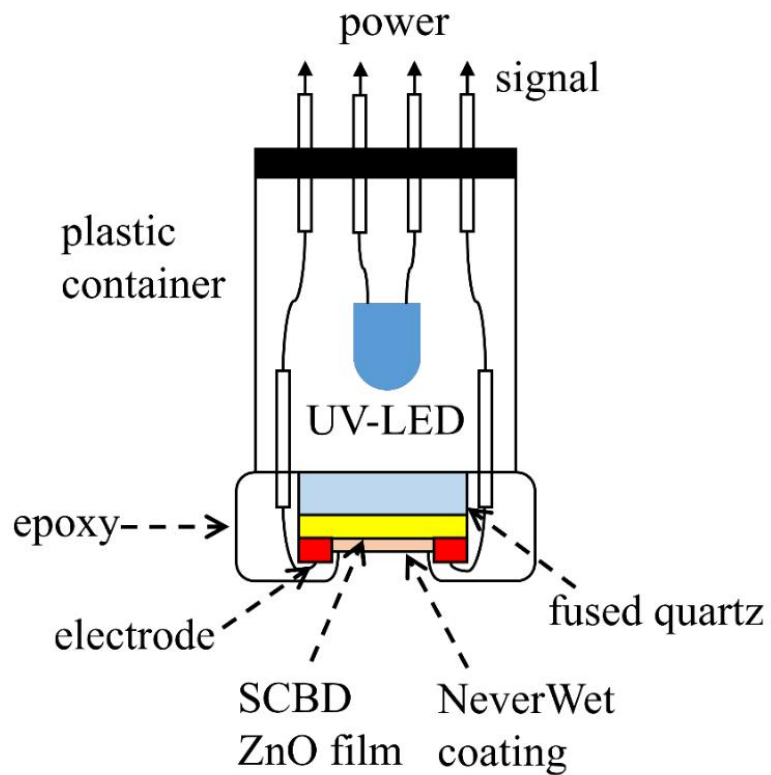


Figure 4.12 Immersion dissolved oxygen sensor prototype made of a 500°C post-oxidized SCBD ZnO film. Left and right bottom: pictures of well and poorly protected immersion sensor taken after measurements in water.



Figure 4.13 shows the results of measurements. The first observed result is that for all the settings of dissolved oxygen content in water, the photo assisted electrical conductivity starts to rise immediately after the UV light is turned on. The rising rate is the largest at the initial moment but drops subsequently as time proceeds. The main difference from that obtained in gas phase is that the time dependences of all the curves detected under UV light over the range of dissolved oxygen content, though not exactly overlap, do not deviate significantly from each other. However, when UV light is turned off, the electrical conductivity of the film drops. The curve detected at different setting of dissolved oxygen content is found to drop with different rate. The one measured at a higher dissolved oxygen content drops faster. This effect is consistent with the previous result that more oxygen in the surrounding help to capture photo generated excessive charge carriers such that the photocurrent extinguishes with a faster rate in an environment of richer oxygen concentration. This feature allows one to establish a relationship among the electrical response of the film and content of dissolved oxygen in water. The potential of the device to be used as a dissolved oxygen sensor is thereby justified.

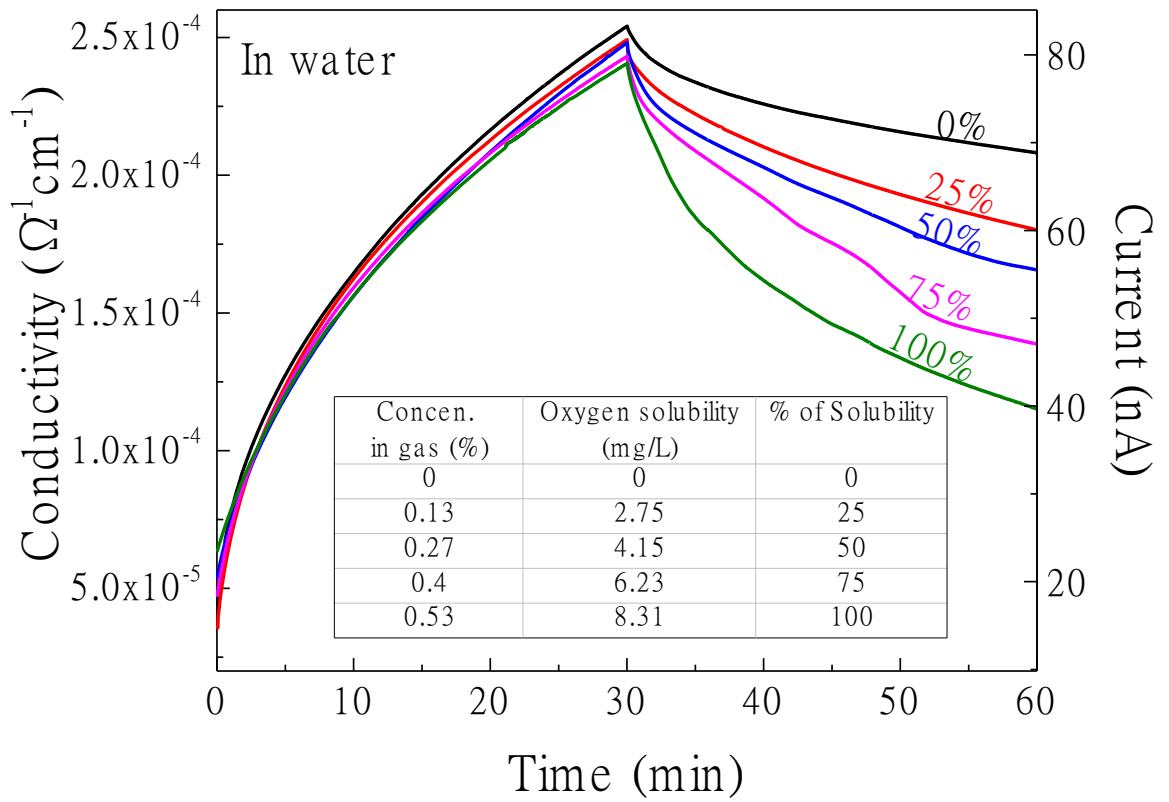
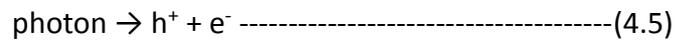


Figure 4.13 Real-time room-temperature photo assisted electrical conductivity of a 500°C post-oxidized SCBD ZnO films covered with a superhydrophobic polymer layer measured at various dissolved oxygen concentrations from 0% and 100%.



4.7 Modeling of oxygen concentration dependence of photo assisted electrical conductivity of SCBD ZnO films and its potential applications

We propose a model to explain the observed photo assisted electrical response to the change of oxygen concentration. First, above-bandgap light illumination on the ZnO film generates photo induced electron-hole pairs. This process is presented with a formula



This reaction occurs to maintain a non-ignorable pollution of conduction charge carriers. These charged particles are responsible for the generation of a photocurrent in the oxide at room temperature. At the same time, some oxygen molecules from the detected region reach the oxide surface. If the film is polymer-coated, they need to diffuse across the polymer coating in order to reach the ZnO film surface.

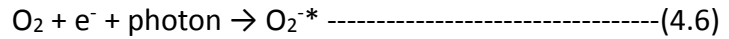
These oxygen species could be adsorbed on the ZnO film surface by combining with conduction electrons from the film. Adsorption states involved can be classified into different categories according to the results reported by Yamazoe et al [72]. They analyzed the data of chromatogram analysis for a typical metal oxide. Desorption of oxygen over a broad range of temperature was realized. On the other hand, they identified the type of adsorption states using electron spin resonance technique. Results show that at temperature < 150°C, the surface sorbed species are in the form of singly charged O_2^- ions based on chemisorption reaction. The reaction is generally described as:



This argument is widely claimed to explain the gas sensing effect of an MO_x material.



When UV light is turned on to shine on the film surface, some surface sorbed oxygen species are in an excited state,



where O_2^{-*} is such an ion in the photo-induced chemisorbed ion state. The oxygen species in this state are more active than the one in the state formed in dark, denoted as an $\text{O}_2^{-(\text{ad})}$. With a higher energy of state, they are more readily desorbed from the oxide surface and return to the environment [73-75]. It is also claimed that an $\text{O}_2^{-(\text{ad})}$ ion is most likely desorbed at around 150°C [72], while an O_2^{-*} ion can be desorbed at a much lower temperature. These two reactions are presented as:



Both processes require the participation of a hole, which all lead to a drop of resistance of the MO_x material. Such a difference of the two reactions is the fundamental origin responsible for the different gas sensing response of MO_x associated with the use of above-bandgap light illumination.

We further propose the model as follows. Let n to be the electron concentration and $[\text{O}_2]$ to be the oxygen concentration in the detected area. The reaction is:

$$dn = G dt - n R_1 dt - [\text{O}_2] n R_2 dt \text{-----(4.9)}$$

The three terms on the right side of the equation represent the change of electron concentration due to light illumination, recombination effect and trapping by surface sorbed oxygen species, respectively. G , R_1 and R_2 in the formula are constants associated with the respective mechanisms. Eq. (4.9) is integrated to obtain



the conduction charge carrier concentration. If n_d is the base charge carrier concentration in dark, the overall induced current is obtained by integration,

$$dn = Gdt - nRdt$$

$$dt = (1/G)(1 - nR/G)dn$$

$$t = -(1/R) \ln(1 - R/G) \quad \text{by integration}$$

$$-Rt = \ln(-Rn/G+1)$$

$$\exp(-Rt) = -Rn/G+1$$

$$G/R(1 - \exp(-Rt)) = n$$

$$I = (V_a A/L) e\mu[n_d + (G/R)[1 - \exp(-Rt)]] = I_d + I_1 [1 - \exp(-Rt)] \quad \text{-----(4.10)}$$

In the formula, V_a is the applied voltage across the electrodes, A the cross-section area = film thickness \times width of the electrodes, L the length of the measured region and μ the carrier drift mobility. Furthermore, a quantity $R \equiv R_1 + [O_2] \cdot R_2$ is introduced.

Eq. (4.10) is then used to fit the real-time dependence of photo-assisted electrical conductivity recorded in the measurements. The parameters I_1 and R are adjusted to achieve the best fits. The optimum value of I_1 , combined with the measured dark current I_d , is used to calculate the saturated current $I_{\text{sat}} = I_d + I_1$.

The best fit parameters associated with different settings of oxygen concentration are then used to establish some functional relationships. These relationships are claimed to be useable afterwards for determining the oxygen content in a quantitative manner based on the best fit parameters to the whole time dependence of electrical conductivity observed in a specific test.

A useful relationship of this kind is the one correlating the oxygen concentration and the saturated photo assisted electrical conductivity (or saturated current I_{sat})



obtained from fitting Eq. (4-10) to the curves in Figure 4.9. The function is plotted and shown in Figure 4.14 (a). It is expected to be usable in determining the oxygen concentration in a dry gaseous environment by using an uncoated SCBD ZnO film sensor.

Another useful relationship is the one correlating the oxygen concentration and the saturated photo assisted electrical conductivity (or saturated current I_{sat}) obtained from fitting Eq. (4.10) to the curves presented in Figure 4.11. The functional relationship thus obtained is plotted and shown in Figure 4.14 (b). It is claimed to be usable in determining the oxygen concentration in a highly humid gaseous environment by using a superhydrophobic polymer coated SCBD ZnO film sensor.

The last example is the relationship correlating the dissolved oxygen concentration in water with the decaying time of the current detected after turning off the UV light as shown in Figure 4.13. The relationship is plotted and shown in Figure 4.14 (c). We further claim that it can be used to determine the dissolved oxygen content in water at room temperature according using our specially designed immersion oxygen sensor.

The common advantage of the above proposed approaches for oxygen concentration detection based on curve fitting is that an estimate of the answer can be derived just according to part of the time-dependent curve of the measured quantity, but there is no need to wait for a very long period of time for the measured quantity to reach the real equilibrium state. As it is not uncommon for a chemical sensor to exhibit prolonged response time and recovery time in gas detection, the approach may give a general meaning in extending the applicability of the materials



of this kind in gas sensing applications.

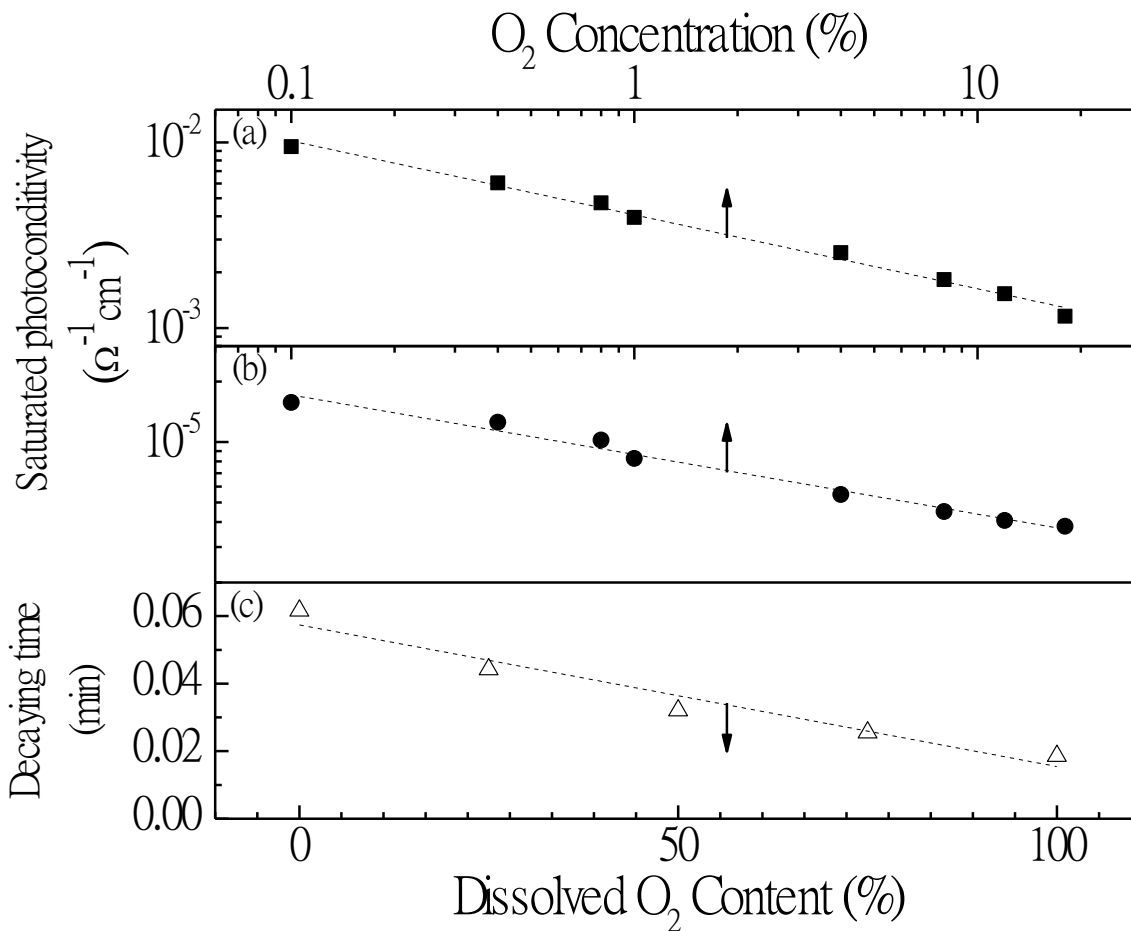


Figure 4.14 Three relationships correlating the O₂ concentration in the detected area and a fitting parameter to the time dependence of photocurrent using a 500°C-post oxidized SCBD ZnO film. (a) I_{sat} of an uncoated film sensor versus O₂ concentration in dry O₂-N₂ mixture; (b) I_{sat} of a polymer-coated film sensor versus O₂ concentration in 95% humid O₂-N₂ mixture; and (c) decay time of current after turning off UV light versus dissolved oxygen content in water.



Chapter 5 Results and Discussions for H₂ Gas Detection

5.1 About the palladium-coated SCBD ZnO films for the study of H₂ sensing

We selected 500°C to post oxidize the as-deposited SCBD ZnO films for the study of H₂ sensing. It is the same temperature used to post oxidize film samples for oxygen sensing as described in the Chapter 4. The film structure, according to the results of structural characterization experiments as described in Section 4.1, was reconfirmed to be composed of partly crystallized nanoclusters, and was highly porous.

Differently, in this part of the study, the films used in this part of study were decorated with a 5-nm thick palladium (Pd) coating using sputtering method. Samples of such a structure are designated as nano sponge ZnO (ns-ZnO) films. The surface Pd coating is a catalyst, known to be effective in assisting dissociation of H₂ molecules into atoms. It lowers the activation energy to facilitate ensuing chemical reactions and subsequently the generation of H₂ sensing signal [58]. Furthermore, each film sample was made to have two silver paste electrodes separated with a distance of 5 mm on the surface. The film is placed in a measurement chamber for doing the tests.

5.2 Basic features of H₂ sensing properties of Pd-coated ns-ZnO films

We first investigated the room-temperature real-time dependence of electrical conductivity of Pd-decorated ns-ZnO films in 2% H₂ gas balanced in air. No UV assist was applied.

In a test, a flow of sample gas was admitted into the measurement chamber for it to react with the film sample. The time dependence of the electrical resistivity of the film sample was recorded. As seen in Figure 5.1a, the film resistance drops from



very quickly from $3.41 \times 10^9 \Omega$ to $3.7 \times 10^8 \Omega$ within 1 s, and further drops to stabilize at a level around $4 \times 10^7 \Omega$. The gas flow was kept steady for 15 s. The measurement chamber was then evacuated and filled up with air. The film resistance rises afterwards and returns to its initial value in a period of around 1 min. The response time was estimated to be around 47 s. It is noticed that the response time of our Pd/ns-ZnO film is fairly short, such that the response rate is superior to those of many other MO_x-based H₂ sensors working at room temperature usually in the range of a few minute [76-80]. These findings disclose the fact that our Pd-coated ns-ZnO films have potential use in H₂ sensing applications.

In order to examine the effect of rising the operation temperature on the sensor's performance, particularly the effect on remedying the interference caused by adhesion of moisture on the sensor's surface, we also investigated the H₂ sensor response at 80°C. Figure 5.1b shows the comparison of the results acquired at 20°C and 80°C respectively, for 2% H₂ balanced in air. Furthermore, the sensor response, S , response time t_{res} and recovery time t_{rec} extracted from the data for both cases are tabulated in Table 5.1. It is found that the sensing properties attained at 80°C are superior to those obtained at 20°C in all aspects. At the higher operation temperature of 80°C, (i) S increases from 82 to 3537, namely an enhancement of 43 times; (ii) t_{res} and t_{rec} decrease from 1 s and 47 s to 0.3 s and 18 s respectively, namely 3 times shorter. The improvements are attributed to the faster dissociation rate of H₂ on the Pd coating, the faster migration speed of H species crossing the Pd layer to reach the ZnO film surface, are the faster reaction rate between H species and surface sorbed O₂⁻ species.

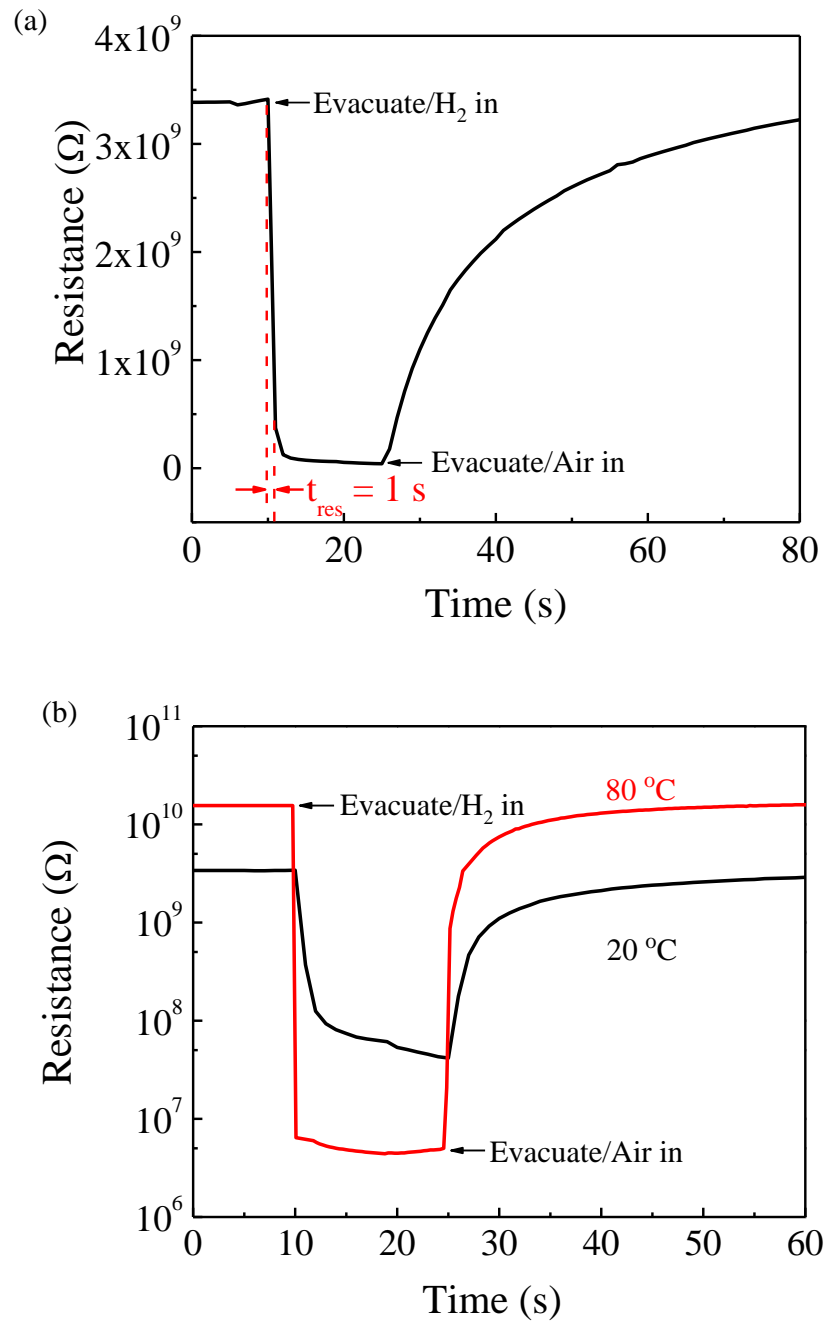


Figure 5.1 (a) Resistive response of Pd-coated ns-ZnO film to 2% H₂ balanced in air.

(b) Comparison of results obtained at 20°C and 80°C.



Table 5.1 Comparison of sensing parameters measured at 20°C and 80°C, with and without UV assist respectively.

Test condition	R _{air} (GΩ)	R _{H₂} (MΩ)	I _{air} (nA)	I _{H₂} (nA)	S	t _{res} (s)	t _{rec} (s)
UV Off, 80°C	15.6	4.41	0.06	227	3537	0.3	18
UV On, 80°C	1.11	1.91	0.90	523	581	0.3	22
UV Off, 20°C	3.41	41.6	0.29	24.0	82	1	52
UV On, 20°C	0.77	8.99	1.30	111	85	2	---

5.3 Influence of relative humidity on the H₂ sensing properties of Pd-coated ns-ZnO films

Although one of the aims of this project is to look for the possibility of operating an MO_x-based gas sensor at ambient temperature, we still proceeded to examine how a Pd-coated ns-ZnO film behaved at a temperature slightly above room temperature. The intention was to remedy the influence of adhesion of moisture from the detected area on the film sensor's surface. The temperature selected for the study was 80°C. The sample gas was made to have a rather high relative humidity (RH).

Figure 5.2 shows the results of measurements conducted at 80°C. With the increase of RH in air, the real-time dependence of the electrical resistance is almost unaffected by the change of RH from 0 to 50%, and just decreases slightly when RH is further increased to 90%. Furthermore, with the presence of 2% H₂ in air, the film resistance is basically unaffected for all settings of RH. The influence of RH at 80°C is



so minute, suggesting that such a low operation temperature works good enough to remedy the interference of moisture in the detected environment. One reasonable explanation is that at this temperature, most of the H₂O molecules on the film surface are physisorbed. They are readily detached by gaining a small amount of thermal energy [81, 82]. On the other hand, chemisorbed H₂O molecules have not formed, and cannot give significant contribution to the gas sensing process at this temperature [83]. Furthermore, such an operation temperature is rather close to room temperature, and hence would not result in substantial annealing of the sensor material and instability of output, like thermal drift or unrepeatable sensor response associated with the structural change of material properties.

Based on the above observations, we confirm that 80°C was a preferred operation temperature for a Pd-coated ns-ZnO film sensor to work for detecting H₂ gas. This condition gives a compromise of sensing properties and stability, degree of complication of device design and the cost of production. A sensor can be equipped with a low-power heater for providing feedback signal and stabilizing the sensor temperature. The influence of the fluctuation of ambient temperature is relatively little. The overall performance of the sensor should be superior to that achieved at room temperature.

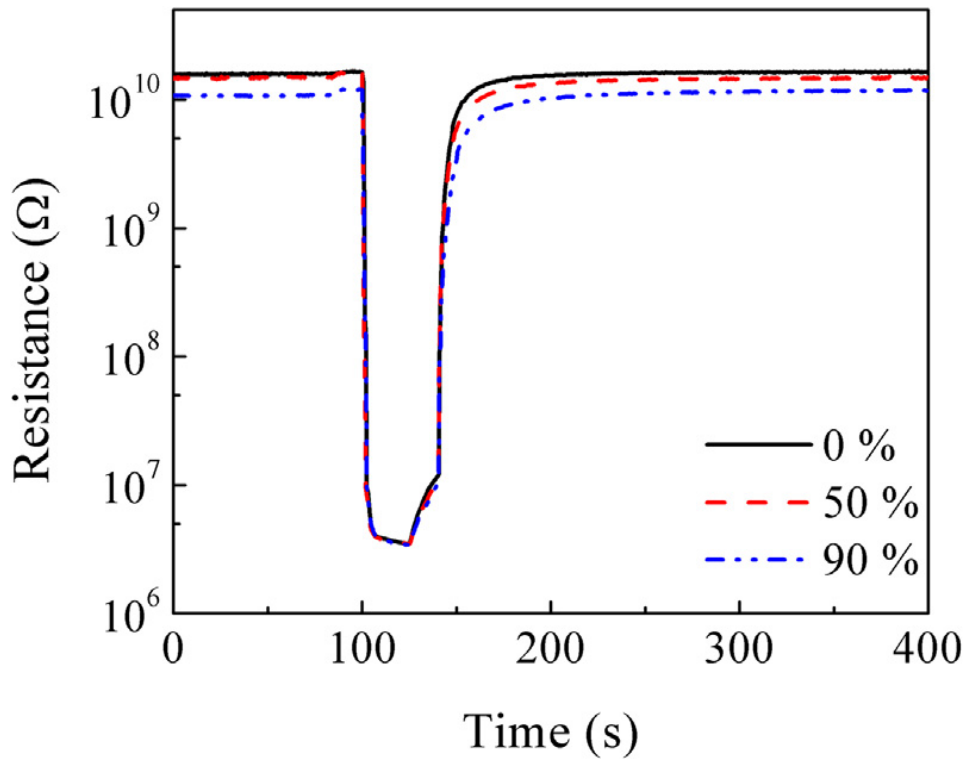


Figure 5.2 Real-time dependence of resistive response of a Pd-coated ns-ZnO film to 2% H₂ in air measured at 0, 50% and 90% relative humidity at an operation temperature of 80°C.

5.4 H₂ concentration dependence of the sensor response

We further investigated how the resistance of the film sensor at 80°C responded to the change of H₂ concentration. Figure 5.3 shows the results measured at different H₂ concentrations varied from 0.1 to 2%. Both the sensor response and response rate were found to increase with increasing H₂ concentration. The correlation between the film resistance and H₂ concentration gives a functional relationship, which is usable for quantitative determination of the gas concentration in an environment. The potential of the Pd-coated ns-ZnO film in the application in H₂ sensing is justified.

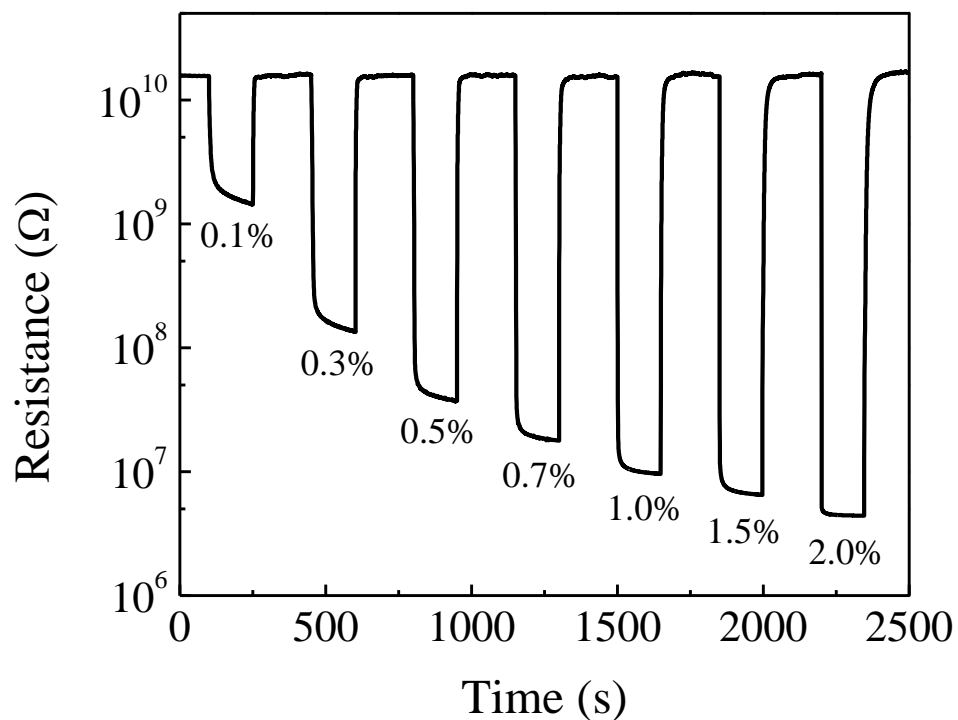


Figure 5.3 Real-time dependence of resistive response of Pd-coated ns-ZnO film to 0.1–2% H₂ in air measured at 80°C.



5.5 Effect of using UV assist on H₂ sensing properties

The effect of UV assist on H₂ sensing properties was examined by comparing the data acquired at 20°C and 80°C, respectively. Results are shown in Figure 5.4 (a) and (b). The values of sensor response S , response time t_{res} and recovery time t_{rec} derived from the data for the two cases are tabulated in Table 5.1 for analysis.

We first look at the results obtained at 80°C as shown in Figure 5.4 (a). The sensor response S measured in dark is 3537. However, it drops significantly to 581 after employing UV assist. On the other hand, t_{res} observed in the two cases are close. t_{rec} measured at 80°C is slightly longer (Table 5.1). All these results indicate that UV assist does not give effective improvement of the gas sensing properties of the sensor operating at 80°C.

Next, consider the results obtained at 20°C. One still cannot see improvement of the sensor response using photo assist. However, the response time seems to be longer. In both cases of having and without photo assist, the recovery of resistance is not complete within the period of measurements. We further conclude that the use of photo assist does not give any advantages in the sensor response, and the rates of response and recovery.

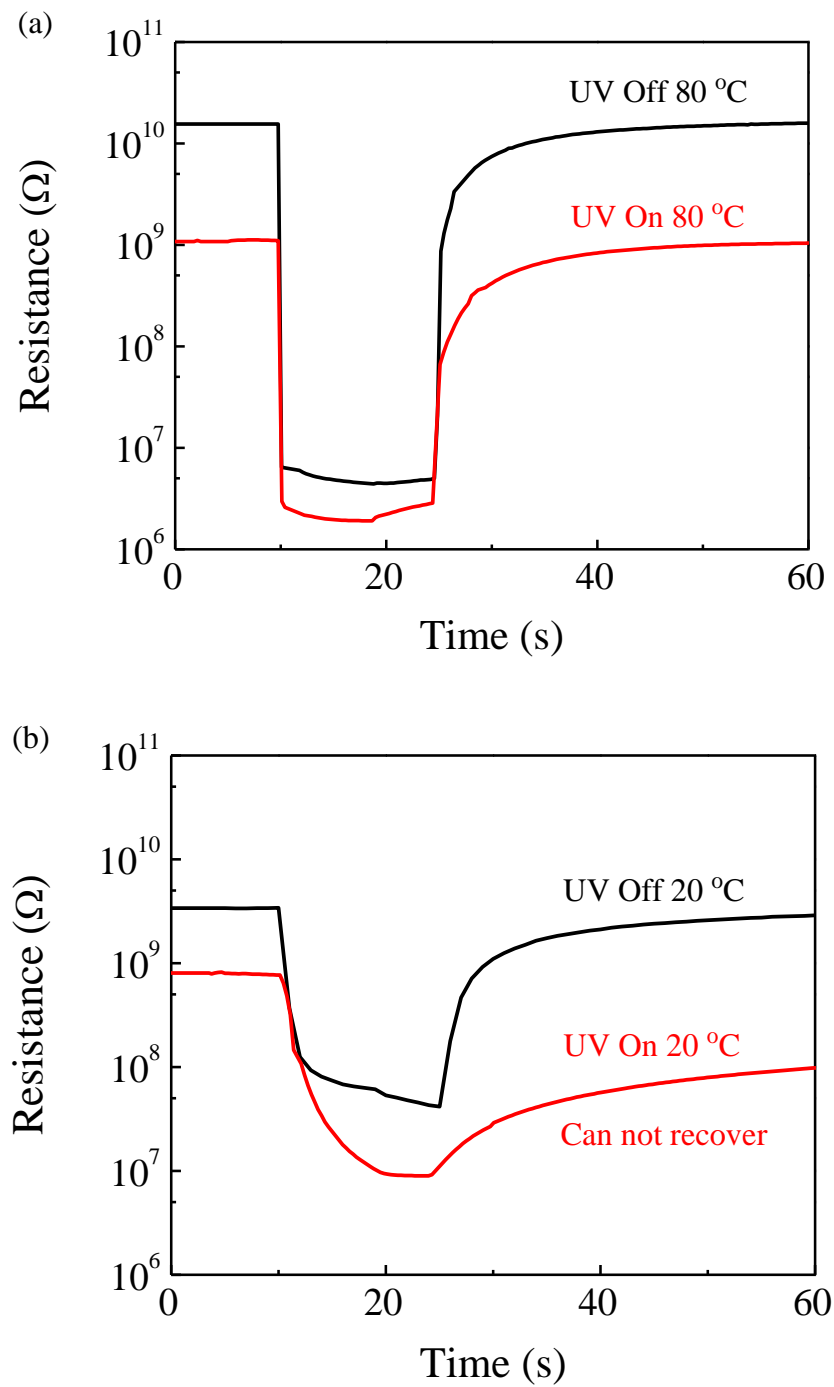


Figure 5.4 Comparison of time dependence of resistive response of Pd-coated ns-ZnO film to 2% H₂ in air with and without using UV irradiation measured at (a) 80 and (b) 20°C.



We then examined the influence of using photo assist on the stability of sensor response of the film sensors operating in cyclic mode. Results of measurements in two cases of using and without using UV illumination are shown in Figure 5.5 (a) and (b) respectively. In a typical test, 2% H₂ in dry air was admitted into the measurement chamber for a predetermined period of time. The chamber was then evacuated with a rotary pump. Dry air was then admitted to fill up the chamber. The processes were repeated by many times in a cyclic manner. The real-time dependence of the film resistance was recorded throughout the course.

Look at the data without UV assist as shown in Figure 5.5 (a). The cyclic resistive response of the film varies with increasing number of cycles. The instability mainly comes from successive increase of the film resistance detected in air, whereas that measured in 2% H₂ remains unchanged. This phenomenon is explained by assuming that the Pd coating is conducting and should have some contribution in affecting the overall resistance of the sensor. The Pd film is hydrogenated when reacting with H₂ and subsequent undergoes a notable volume expansion. During unloading of hydrogen, the film volume contracts to return to the original status. Volumetric breathing occurs in cycle tests, such that cracks are formed in the Pd layer. The overall resistance of the film thus increases the test proceeds.

Figure 5.5 (b) shows the results after the use of UV assist. One sees that the output of the sensor is much consistent and stable with the increase of the number of loading-unloading cycles. In particular, the drift of film resistance in air (unloading state) remains stable and does not exhibit noticeable shift as that observed in the case without using photo assist. This is explained as the fact that under UV light



illumination, the film resistance is dominated by photocurrent, but becomes less affected by the Pd coating. Though the Pd coating still experiences volume breath effect and cracks are thus produced in the test, the film resistance at the unloading state in air is capped at $\sim 1\text{ G}\Omega$, which is about one order of magnitude lower than the corresponding quantity measured without the use of photo assist. Importantly, the cyclic sensor response of the Pd-coated ns-ZnO film becomes more stable. This is regarded as an advantage of using UV assist when operating the gas sensor.

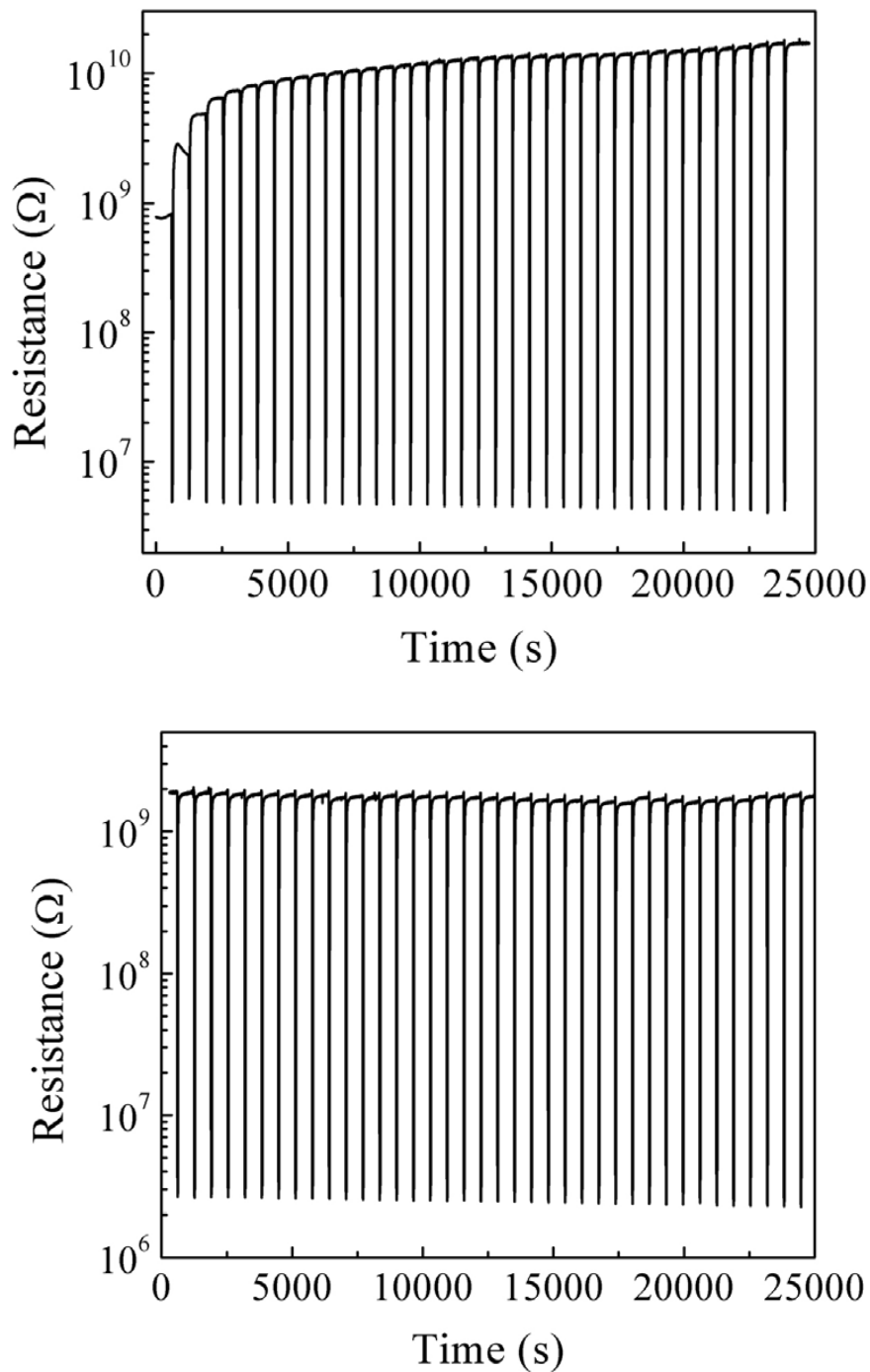


Figure 5.5 Cyclic stability tests of the resistive response of a Pd-coated ns-ZnO film exposed alternatively to 2% H₂ in air and dry air at 80°C (a) without using and (b) using UV illumination. The power density of light is 10 mW/cm².



5.6 Comparison of H₂ sensing properties of our sensors with the published results

The values of S and t_{rec} of our samples are plotted in Figure 5.6 as functions of H₂ concentration. Published data obtained by many other authors based on their own sensors are plotted in the figure for comparison. The published data associated with the use of nanocluster-based material and 1-dimensional-based nanomaterials are labeled with solid and hollow symbols, respectively. All of them are reported to be measured at temperatures $> 200^{\circ}\text{C}$.

One sees that the sensor response of S of our Pd-coated ns-ZnO film is higher than most of the published ones measured at H₂ concentration in the range of 0.1 – 2%. Exceptions are the Pt activated TiO₂:WO₃ nanocrystalline film working at 200°C and Pd activated WO₃ nanocrystalline film working at 300°C. These two cases exhibit larger S values. However, the values of t_{res} of these cases are at least 5 times longer than our result.

Comparison also shows that the values of t_{res} of our Pd/ns-ZnO film is shorter than most of the published values measured at temperatures $> 200^{\circ}\text{C}$. Exceptions are the results of the single wall carbon nanotube and tin oxide nanoparticles hybrid thin films (CNT-SnO₂) working at 250°C, for which the values of S are only 1/10 of that of our sample. The superiority of the H₂ sensing properties of our Pd/ns-ZnO film is clearly justified.

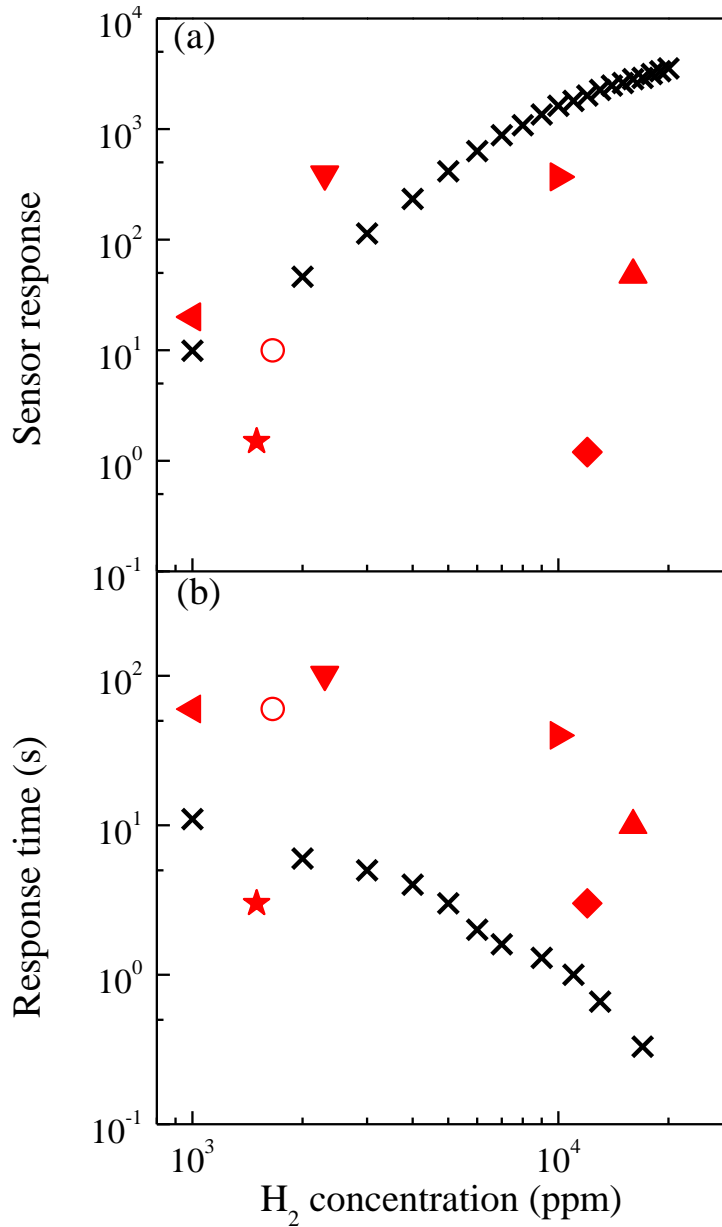


Figure 5.6 Comparison of (a) S and (b) t_{res} of a Pd-coated ns-ZnO film measured at 80°C with the published data of various H₂ sensors composed of MO_x nanoclusters (solid symbols) and 1-dimensional MO_x nano particles (hollow symbols) measured at temperatures > 200°C.

× our sample at 80°C ▲ Pt-WO₃/ZrO₂ [84] ◄ Pt-WO₃-TiO₂ [85] ★ SnO₂-CNT [86]

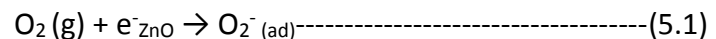
▼ Pd/WO₃ [87] ▶ Au/WO₃ [88] ◆ CNT-WO₃ [89] ○ MgZnFe₂O₄ [90]



5.7 Modelling of H₂ sensing process for MO_x-based gas sensor

For gaining more physical insights on the gas sensing properties of an MO_x-based sensor, we proposed a model involving the following processes which may be used to explain the phenomena observed in our H₂ sensing experiments. A picture shown in Figure 5.7 is depicted to help explanation.

In this model, a gas sensing process starts with O₂ adsorption in a dark H₂-free air environment (before turning on UV light). Oxygen molecules may physisorbed or chemisorbed on the ZnO surface. They combine with conduction electrons from the MO_x material and become O₂⁻ ions as expressed in Eq. (5.1), or Reaction ① in Figure 5.7.

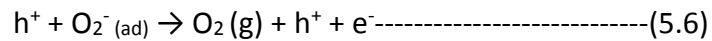
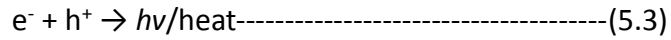
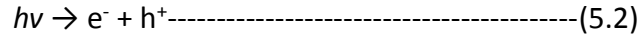


An electric field is generated near the MO_x grain surface along the normal of the grain surface. It sweeps away most mobile charge carriers in this region to leave a highly resistive depletion region on the nanocluster's surface. The resistance of the Pd-coated ns-ZnO film at this stage is high.

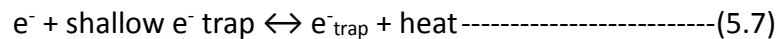
The next stage of the sensing process starts when UV light is turned on. Photo electrons (e⁻) and holes (h⁺) are generated (Eq. (5.2), Reaction ②). Part of them are recombined via band-to-band transitions (Eq. (5.3), Reaction ③). Other electrons and holes are separated by the electric field near the grain surface. Holes tend to migrate towards the grain surface. When they fall into recombination centers, they may recombine with electrons at the region close to the film surface (Eqs.(5.4) and (5.5), Reaction ④ and ⑤). These oxygen species involved in the interactions would be detached and leave the film surface (Eq.(5.6), Reaction ⑥). The electrons released



after the reaction return to the film and contribute to electrical conductivity. The resistance of the film drops as a consequence. These processes could be expressed by the formulas,



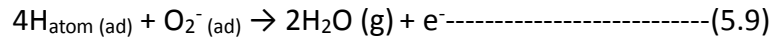
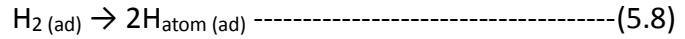
It is noted that the MO_x may have shallow electron traps located closely to the bottom of the conduction band. They like to join and form a storehouse to accommodate conduction electrons. The captured electrons are less mobile, but can still be able to transport via tunneling from a trap state to another, or be re-excited to enter the conduction band. These processes are conducting to build up a dynamic equilibrium (Eq.(5.7), Reaction ⑦), where the distribution of charge carriers in different states are steady. When the assist light is turned off, the condition of equilibrium is broken, and the charge carriers must be redistributed among different group of states to return to the original status. The is a prolonged process, expressed as



The third stage commences when hydrogen appears and starts to react with the film material. The gas molecules first in contact with the surface Pd layer. They are catalytically dissociated into H atoms (Eq.(5.8), Reaction ⑧). The H atoms diffuse onto the ZnO surface and interact with the surface sorbed O₂⁻ ions (Eq. (5.9), Reaction ⑨). Conduction electrons are released to the nanocluster via Reaction ⑨, and enter



the conduction band of the oxide. The depletion layer becomes thinner. The volume of the depletion region on the grain surface is reduced. The film resistance drops as a consequence. The reactions are expressed as



Now we explain why the photo assisted sensor response S to H₂ is lower than that observed in dark. S is defined as $R_{\text{air}}/R_{\text{H}_2}$, where R_{air} and R_{H_2} are the film resistance in air and hydrogen-containing atmosphere respectively. It is known that R_{air} detected under light assist is 1/14 of that detected in dark (dominated by Reaction ② and ⑥). If the values of R_{H_2} (dominated by Reactions ⑧ and ⑨) measured in dark and under light assist are of the same order of magnitude, the value of S with photo assist would be smaller than that measured in dark.

We further explain why the recovery time t_{rec} observed after turning off the assist light is longer than that observed in dark. One notices that Reaction ⑦ takes place in the gas detection process. It presents the scenario that the UV illumination generates photo electrons, whereas some of them drop into the shallow electron trap states. These electrons need some time to escape from these states and continue to contribute in maintaining a current after the UV light is turned off. The escape rate is controlled by the temperature of the environment from which the thermal energy is absorbed. At a near room-temperature environment, the escape rate is low and hence a long t_{rec} is achieved.

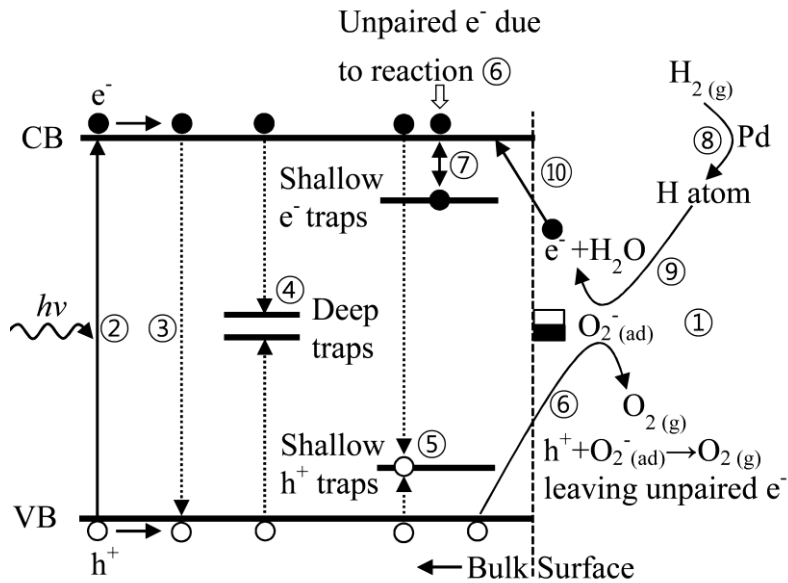


Figure 5.7 Simplified model for explaining the photo assisted H₂ sensing process of a Pd-coated ns-ZnO film. Reaction (1): chemisorption of oxygen and formation of O_2^- ion, Reaction (2): photogeneration of e^- - h^+ pairs, Reaction (3): band-to-band recombination, Reaction (4): recombination at deep traps, Reaction (5): recombination at shallow hole traps, Reaction (6): reaction of h^+ with chemisorbed O_2^- ions, Reaction (7): extraction and release of free electrons by surface e^- traps, Reaction (8): catalytic dissociation of H_2 at Pd surface, Reaction (9): reaction of dissociated H atom with chemisorbed O_2^- ions, and Reaction (10): release of free e^- produced by Reaction (9) to conduction band.



Chapter 6 Conclusions

6.1 Summary of findings

The purposes of this project are to

- (i) fabricate highly porous ZnO thin films using the Supersonic Cluster Beam Deposition (SCBD) technique;
- (ii) investigate the ambient temperature (room temperature and 80°C) photo-assist O₂ gas sensing properties of SCBD ZnO films without and with hydrophobic polymer coating in dry gas and humid gas environments;
- (iii) investigate the room-temperature photo-assist dissolved oxygen sensing properties in water with a device made of a hydrophobic polymer coated SCBD ZnO film, and
- (iv) investigate the H₂ gas sensing properties of Pd-coated ns-ZnO films at room-temperature and 80°C without and with photo assist.

In the first part of the study, we successfully fabricated highly porous ZnO film using SCBD method. The films were post oxidized at different temperatures from 450 to 600°C, and the film structure was found to be considerably improved in terms of being better crystallized and more stable. However, the film structure remains to be highly porous and is composed of nanoclusters. XRD data verify that the nanoclusters are mainly in the ZnO phase.

In the second part of the study, we first determined the optimum post-oxidizing temperature to be used for making film samples for detailed gas sensing experiments. Results were found as follows.



- (i) The film post-oxidized at 450°C exhibited the strongest photo-assisted electrical conductivity. However, the output signal is not easily stabilized, and is still increasing with gradually decreasing rate over the time period used in the measurement. It also takes a very long time to return to the original status after the light is turned off, namely more than 1400 min. It is believed that the film structure formed at this post-oxidized temperature is rather defective. Considerable amount of defect states are present, which contribute to accommodate conduction electrons. Electrons can hop through these defect states or be re-excited to the conduction band and contribute to electrical conduction. The photo-assisted electrical conductivity response to oxygen is thereby relatively strong but very long time is required to stabilize the distribution of electrons in different groups of energy states. The use of a higher post-oxidizing temperature results in faster response rate, but the sensor response becomes weaker. The reason is that the film structure is better crystallized, such that the concentration of defect states is reduced. Hopping conduction becomes less significant and gives less contribution to the sensor response. On the other hand, the drift mobility of charge carriers is increased to facilitate electrons to reach equilibrium state in a shorter period of time whenever the ambient gas concentration is altered.
- (ii) Results of the measurement of cyclic electrical response to oxygen show that the 500°C post-annealed sample exhibits good repeatability. Combining all the observed results, we determined to use 500°C as the post-oxidation temperature for preparing samples to be used in ensuing gas sensing study.



- (iii) An uncoated SCBD ZnO film was used to detect O₂ balanced N₂ in dry gaseous environment. The film was confirmed to be effective in generating electrical signal for oxygen detection. Importantly, the sensor response was found to drop systematic with the rise in O₂ content. A functional relationship can be established. The feasibility of using SCBD ZnO in quantitative oxygen detection is justified.
- (iv) A super-hydrophobic polymer coating made of a commercial spraying product, NeverWet, was added to the surface of a 500°C-post oxidized SCBD ZnO film. It was further used to detect O₂ in dry O₂-N₂ gaseous environment. It was found that the presence of the polymer coating reduces the sensing response considerably by more than 10 times. However, the response time is considerably shortened.
- (v) The polymer coated film sample was also used to detect O₂ in 95% humid O₂-N₂ gaseous environment. The sensor response was further reduced. However, the polymer coating was found to be effective in protecting the ZnO film against the interference induced by the moisture in detected gaseous environment.

In the third part of the study, an immersion oxygen sensor made of a polymer coated film was designed and fabricated. It is constructed of a small water-proof cylinder in which an UV LED is housed. The light from the LED penetrates through the uncoated side of the glass substrate and to shine on the SCBD ZnO film from the side of the substrate-film interface. The other side of the film is protected by the polymer coating, and is immersed in water. The water was made to contain known amount of dissolved oxygen concentration varying from 0 to 100% of the saturated level. The



photo assisted electrical conductivity monitored as the output signal against the change of dissolved oxygen content in water. Important findings are as follows.

- (i) The parts of the curves of electrical conductivity observed after turning on the UV light at various dissolved oxygen contents are similar, and hence the change of the magnitude of the sensor response alone is not sufficient in reflecting the change of dissolved oxygen content in water.
- (ii) The decay rate of the electrical conductivity observed after turning off the UV light was found to vary with the change of dissolved oxygen concentration. This finding shed light on the feasibility of using the relationship for determining the dissolved oxygen content in a quantitative manner.
- (iii) We proposed a method for quantitative determination of the oxygen content in an area (including the cases of gaseous environment and water). The method is based on the concept of deriving some fitting parameters giving the best fit to part of the real-time dependence of the electrical conductivity acquired from measurements. This method has the advantage of having no need of waiting the measured quantity to reach real equilibrium and hence the time of detection can be shortened considerably.
- (iv) We also proposed a model for describing possible physiochemical reactions involved in the gas sensing process. The model combines the effects of surface sorption of the oxygen species, photo generation and recombination of electron-hole pairs, and stabilization of electrical conductivity. We also pointed out the influence of defects states in the recovery of residual current after turning off the excitation light.



In the fourth part of the study, we demonstrated the feasibility of using a Pd-coated ns-ZnO film for sensing H₂ gas. The main results are as follows.

- (i) At 20°C, a Pd-coated ns-ZnO film showed a sensor response of 82 and a response time as short as 1 s to 2% H₂ balanced in air.
- (ii) At 80°C, the sensor response increases to ~3540 and response time drops to 0.3s. The use of 80°C operation temperature helps to stabilize the sensor's output signal against the influence of ambient temperature fluctuation and water vapor.
- (iii) The use of UV assist degrades the sensor response and does not have discernible improvement on the response time. However, it has the advantage of enhancing the cyclic repeatability of the sensor response.

6.2 Further work

Based on the above findings, we propose some topics as listed in the following which are meaningful for further investigations.

6.2.1 Mechanism of gas adsorption to photoconductivity

We found in this study that the photo-assist electrical conductivity of different materials exhibits some similar features. For example, some period of time is needed for the measured quantity to reach equilibrium after turning on the assist light. This means that some common mechanisms are involved in determining the trend. In the present work, we only employed a simplified theory to model the decay of the photo electrical conductivity after the light was turned off. The model was based on some simple assumptions. We believed that there are more rooms for one to investigate in



more detail on the physiochemical reactions actually happening in the process, and give a more complete fitting to the real-time curve of photo assisted electrical conductivity. Meanwhile, some of other more well-known adsorption theories, like Elovich equation or Brunauer-Emmet-Teller (BET) theory including considerations of chemisorption can be introduced to enrich the discussion. A better approach for fitting the measured time dependence of the sensor output could be achieved by incorporating these advanced factors. A more convincing functional relationship can be obtained for better determination of the gas concentration in the detected environment.

6.2.2 Effect of defects in MO_x materials on photo assisted gas sensing response

The study on SCBD ZnO film illustrates an interesting phenomenon that a more structural defective MO_x material achieved by post-annealing at lower temperature can exhibit very strong photo assisted electrical conductivity to a gas. The strong sensing response is frequently accompanied by very long response time and recovery time. This leads us to suspect that the presence of defects play an important role in enhancing the photo-assisted electrical response and prolonging the process approaching equilibrium. Some literatures also reported that functionalized reduced graphene oxide [59,67] or the presence of disordered grain boundaries in a material [68] can exhibit gas sensing effect. We think that more work can be done to gain insights on the role of the defects on gas sensing effect by further controlling the type and concentration of surface defects in an oxide material.



6.2.3 Influence of material selection

This study is mainly focused on one material, namely ZnO. However, there are much more other choices of materials to be used for similar studies. For example, SnO₂ is a good potential candidate to be investigated. We propose to the use SCBD method to fabricate porous SnO₂ films and repeat the measurements as that carried out in this project. One will be able to find out common phenomena as that observed with the use of SCBD ZnO. More information can be achieved to enrich the discussion about the fundamental mechanisms governing the gas sensing properties common to some other oxide materials.

6.2.4 Effect of excitation source in photo-assisted gas sensing performance

Photo excitation plays an important role in creating an active and dynamic surface to facilitate gas sensing effect. Yet, the effects of light intensity and wavelength of the excitation source were little reported in literature. We thereby propose to perform some tests on finding out the optimum condition of photo assist for attaining the best result of gas sensor response of an oxide material. We also propose to emphasize the investigation on the fundamental principle underlying the phenomenon.

For example, photo assist with a higher intensity of light involved a denser flow of photons, which is believed to generate more charge carriers in a test. However, only part of the photo generated excessive charge carriers is involved in generating the gas detection signal, but quite a considerable part of them would contribute to increase the base level of the electrical conductivity of the film sensor. Consequently,



the fractional change of electrical conductivity induced by the detected gas becomes less pronounced. In another words, the magnitude of gas sensor response achieved after the use of photo assist becomes smaller if the intensity of light increases to exceed some threshold. It would be interesting to verify the presence of such a threshold and further to determine its value in a quantitative manner.

Another example of further research topic of interest is inspired by the finding of irreversible change of gas sensor response observed after prolonged illumination on a film sample. There may have some reasons responsible for this phenomenon. They could involve alternation of the material structure by energetic photons, such as the change of crystallization of the material or bond breaking etc. These effects may lead to instability of the material properties. On the other hand, photons with energy much higher than the bandgap may generate “hot charge carriers”. This effect on a solid is still not clearly understood and is worth to study through observing the gas sensing properties of a material under illumination of light of different wavelengths.

6.2.5 Design of new gas sensors

New gas sensors of improved properties can be achieved by using new materials of different compositions and/or surface morphology or applying different operation modes. One expects that deficient or excessive coverage of the sensor surface by oxygen is unfavorable for obtaining a strong gas sensor response. The ideal condition for detecting a reducing gas is to pre-adsorb one monolayer of oxygen on the sensor surface. This can be achieved by using more defective surface to increase the detect states. One method is to add catalyst to increase the adsorption speed. On the other



hand, excessive adsorption can be alleviated by rising the operation temperature or illuminating the sensor's surface with a higher-power light beam. All these ideas can be incorporated in creating new designs of gas sensors using the same material for enhancing the gas sensing performance. This imposes great rooms in the field of engineering to further extend the achievements obtained from this study.



References

- [1] Y.J. Zhao, Y.B. Wei, Y.F. Li, T.T. Zhang, W.S. Zhao, L. Lv, T.Y. Liu, C. Wang, 'Application of optical fiber oxygen sensor in coal mines', *Progress in Mine Safety Science and Engineering II*, 2014, 1109-1111.
- [2] S. Akbar, P. Dutta, C.H. Lee, 'High-temperature ceramic gas sensors: A review', *Int. J. Appl. Ceram. Tec.* 3, 2006, 302-311.
- [3] H.A. Smithline, N. Rudnitzky, S. Macomber, F.S.J. Blank, 'Pulse oximetry using a disposable finger sensor placed on the forehead in hypoxic patients', *J. Emerg. Med.* 39, 2010, 121-125.
- [4] P. Medelius, 'Sensors for monitoring air quality in earth and space environments', *Sensors for Environment, Health and Security: Advanced Materials and Technologies*, 2009, 431-442.
- [5] L.L. Zhao, D.L. Li, D.K. Ma, Q.S. Ding, 'An portable intelligent measurement instrument for dissolved oxygen in aquaculture', *Sensor Lett.* 8, 2010, 102-108.
- [6] S. Anastasova, M. Milanova, D. Todorovsky, 'Photoluminescence response of Ru(II) complex immobilized in SiO₂-based matrix to dissolved oxygen in beer', *J. Biochem. Biophys. Methods* 70, 2008, 1292-1296.
- [7] P. Villalobos, C.A. Acevedo, F. Albornoz, E. Sanchez, E. Valdes, R. Galindo, M.E. Young, 'A BOD monitoring disposable reactor with alginate-entrapped bacteria', *Bioprocess Biosyst. Eng.* 33, 2010, 961-970.
- [8] S. Kara, B. Keskinler, E. Erhan, 'A novel microbial BOD biosensor developed by the immobilization of *P. syringae* in micro-cellular polymers', *J. Chem. Technol. Biotechnol.*



84, 2009, 511-518.

[9] C.M. Clark, K. Hancke, A. Xydes, K. Hall, F. Schreiber, J. Klemme, J. Lehr, M. Moline, 'Estimation of volumetric oxygen concentration in a marine environment with an autonomous underwater vehicle', *J. Field Robot.* 30, 2013, 1-16.

[10] B. Edwards, D. Murphy, C. Janzen, N. Larson, 'Calibration, response, and hysteresis in deep-sea dissolved oxygen measurements', *J. Atmos. Ocean. Technol.* 27, 2010, 920-931.

[11] V. Aroutiounian, 'Metal oxide hydrogen, oxygen, and carbon monoxide sensors for hydrogen setups and cells', *Int. J. Hydrogen Energy* 32, 2007, 1145-1158.

[12] J. Tollefson, 'Fuel of the future?', *Nature* 464, 2010, 1262-1264.

[13] K. Mazloomi, C. Gomes, 'Hydrogen as an energy carrier: prospects and challenges', *Renew. Sust. Energy Rev.* 16, 2012, 3024-3033.

[14] L. Boon-Brett, J. Bousek, G. Black, P. Moretto, P. Castello, T. Hubert, U. Banach, 'Identifying performance gaps in hydrogen safety sensor technology for automotive and stationary applications', *Int. J. Hydrogen Energy* 35, 2010, 373-384.

[15] F. Yang, D.K. Taggart, R.M. Penner, 'Joule heating a palladium nanowire sensor for accelerated response and recovery to hydrogen gas', *Small* 6, 2010, 1422-1429.

[16] T. Hubert, L. Boon-Brett, G. Black, U. Banach, 'Hydrogen sensors – a review', *Sens. Actuators B* 157, 2011, 329-352.

[17] W.J. Buttner, M.B. Post, R. Burgess, C. Rivkin, 'An overview of hydrogen safety sensors and requirements', *Int. J. Hydrogen Energy* 36, 2011, 2462-2470.



- [18] EPA. 'Channel Processes: Bedload Transport. In Water: Science & Technology', 2012, Retrieved from <http://water.epa.gov/scitech/datait/tools/warsss/bedload.cfm> [Accessed: 23- Jun- 2018]
- [19] Osmond, D.L., D.E. Line, J.A. Gale, R.W. Gannon, C.B. Knott, K.A. Bartenhagen, M.H. Turner, S.W. Coffey, J. Spooner, J. Wells, J.C. Walker, L.L. Hargrove, M.A. Foster, P.D. Robillard, and D.W. Lehning. Turbidity., 'In WATERSHEDSS: Water, Soil and Hydro-Environmental Decision Support System', 1995. Retrieved from <http://www.water.ncsu.edu/watershedss/info/turbid.html> [Accessed: 23- Jun- 2018]
- [20] Furukawa, K., Wolanski, E., & Mueller, H. 'Currents and Sediment Transport in Mangrove Forests', *Estuarine, Coastal and Shelf Science* 44, 1997, 301-310
- [21] EPA. 'What are Suspended and Bedded Sediments (SABS)? In Water: WARSSS', 2012, Retrieved from <http://water.epa.gov/scitech/datait/tools/warsss/sabs.cfm> [Accessed: 23- Jun- 2018]
- [22] Fink, J. C., 'CHAPTER 4 – ESTABLISHING A RELATIONSHIP BETWEEN SEDIMENT CONCENTRATIONS AND TURBIDITY', 2005, Retrieved from http://www.uwgb.edu/watershed/fink/Fink_Thesis_Chap4.pdf [Accessed: 23- Jun- 2018]
- [23] Griffiths, P. G., Hereford, R., & Webb, R. H. 'Sediment yield and runoff frequency of small drainage basins in the Mojave Desert', *Geomorphology* 74, 2006, 232-244
- [24] Gao, Q. 'Correlation of Total Suspended Solids (TSS) and Suspended Sediment Concentration (SSC) Test Methods', 2006, Retrieved from <http://www.state.nj.us/dep/dsr/soils/tss%20vs%20ssc%20test%20methods.pdf> [Accessed: 23- Jun- 2018]



- [25] Odebrecht, K. 'Sediment Transport and Deposition', n.d., Retrieved from <http://www.oregon.gov/dsl/SSNERR/docs/EFS/EFS32sediment.pdf> [Accessed: 11-Jun- 2018]
- [26] MDDNR, 'A Brief Explanation of the Data Available for Viewing', n.d., Retrieved from <http://mddnr.chesapeakebay.net/eyesonthebay/whatsitmean.cfm> [Accessed: 23- Jun- 2018]
- [27] Langland, M., & Cronin, T. (Eds.), A Summary Report of Sediment Processes in Chesapeake Bay and Watershed, 2003, Retrieved from: <http://pa.water.usgs.gov/reports/wrir03-4123.pdf> [Accessed: 23- Jun- 2018]
- [28] J. Tauc, 'Optical properties and electronic structure of amorphous Ge and Si', Materials Research Bulletin 3, 1968, 37-46.
- [29] Crone, T. 'The Basic Sediment Transport Equations Made Ridiculously Simple', 2004, Retrieved from: http://www.ocean.washington.edu/courses/oc410/reading/sedtrans_2004.pdf [Accessed: 23- Jun- 2018]



- [30] F.A. Lewis, 'The palladium hydrogen system', Academic Press, 1967, 3.
- [31] H.S. Nalwa, 'Nanoclusters and nanocrystals', American Scientific Publisher, 2003, 53.
- [32] E.A. Owen, J.I. Jones, 'The effect of pressure and temperature on the occlusion of hydrogen by palladium', Proceedings of the Physical Society 49, 1937, 587-602.
- [33] J.C. Barton, F.A. Lewis, I. Woodward, 'Hysteresis of the relationships between electrical resistance and the hydrogen content of palladium', Trans. Faraday Soc. 59, 1963, 1201-1207.
- [34] Y. Sakamoto, I. Takashima, 'Hysteresis behaviour of electrical resistance of the Pd-H system measured by a gas-phase method', J. Phys. Condens. Mater. 8, 1996, 10511-10520.
- [35] M. Wang, Y. Feng, 'Palladium-silver thin film for hydrogen sensing', Sensor. Actuat. B: Chem. 123, 2007, 101-106.
- [36] S. Akbar, P. Dutta, C.H. Lee, 'High-temperature ceramic gas sensors: a review', Int. J. Appl. Ceram. Tec. 3, 2006, 302-311.
- [37] N. Barsan, D. Koziej, U. Weimar, 'Metal oxide-based gas sensor research: how to', Sensor. Actuat. B: Chem. 121, 2007, 18-35.
- [38] N. Barsan, U. Weimar, 'Conduction model of metal oxide gas sensors', J. Electroceram. 7, 2001, 143-167.
- [39] M.E. Franke, T.J. Koplín, U. Simon, 'Metal and metal oxide nanoparticles in chemiresistors: does the nanoscale matter', Small, 2, 2006, 36-50.
- [40] N. Yamazoe, 'New approaches for improving semiconductor gas sensors, Sensor'. Actuat. B: Chem. 5, 1991, 7-19.



- [41] G. Korotcenkov, 'Gas response control through structural and chemical modification of metal oxide films: state of the art and approaches', *Sensor. Actuat. B: Chem.* 107, 2005, 209-232.
- [42] E. Comini, C. Baratto, G. Faglia, M. Ferroni, A. Vomiero, G. Sberveglieri, 'Quasi-one dimensional metal oxide semiconductors: preparation, characterization and application as chemical sensors', *Prog. Mater. Sci.* 54, 2009, 1-67.
- [43] G. Eranna, B.C. Joshi, D.P. Runthala, R.P. Gupta, 'Oxide materials for development of integrated gas sensors - a comprehensive review', *Crit. Rev. Solid State.* 29 2004, 111-188.
- [44] X.J. Huang, Y.K. Choi, 'Chemical sensors based on nanostructured materials, *Sensor*'. *Actuat. B: Chem.* 122, 2007, 659-671.
- [45] A. Kolmakov, M. Moskovits, 'Chemical sensing and catalysis by one-dimensional metal-oxide nanostructures', *Annu. Rev. Mater. Res.* 34, 2004, 151-180.
- [46] G. Korotcenkov, 'Metal oxides for solid-state gas sensors: what determines our choice', *Mater. Sci. Eng. B: Solid*, 139, 2007, 1-23.
- [47] G. Korotcenkov, B.K. Cho, 'Instability of metal oxide-based conductometric gas sensors and approaches to stability improvement', *Sensor. Actuat. B: Chem.* 156, 2011, 527-538.
- [48] J.G. Lu, P.C. Chang, Z.Y. Fan, 'Quasi-one-dimensional metal oxide materials - synthesis, properties and applications', *Mater. Sci. Eng. R*, 52, 2006, 49-91.
- [49] A.C. Romain, J. Nicolas, 'Long term stability of metal oxide-based gas sensors for e-nose environmental applications: an overview', *Sensor. Actuat. B: Chem.* 146, 2010, 502-506.



- [50] K. Sahner, H.L. Tuller, 'Novel deposition techniques for metal oxide: prospects for gas sensing', *J. Electroceram.* 24, 2010, 177-199.
- [51] Y. Shimizu, T. Maekawa, Y. Nakamura, M. Egashira, 'Effects of gas diffusivity and reactivity on sensing properties of thick film SnO₂-based sensors', *Sensor. Actuat. B: Chem.* 46, 1998, 163-168.
- [52] C.X. Wang, L.W. Yin, L.Y. Zhang, D. Xiang, R. Gao, 'Metal oxide gas sensors: sensitivity and influencing factors', *Sensors-Basel*, 10, 2010, 2088-2106.
- [53] N. Yamazoe, G. Sakai, K. Shimano, 'Oxide semiconductor gas sensors', *Catal. Surv. Asia.* 7, 2003, 63-75.
- [54] Y.T. Chao, S. Yao, W.J. Buttner, J.R. Stetter, 'Amperometric sensor for selective and stable hydrogen measurement', *Sensor. Actuat. B: Chem.* 106, 2005, 784-790.
- [55] G. Korotcenkov, S. Do Han, J.R. Stetter, 'Review of electrochemical hydrogen sensors', *Chem. Rev.* 109, 2009, 1402-1433.
- [56] X.B. Lu, S.G. Wu, L. Wang, Z.X. Su, 'Solid-state amperometric hydrogen sensor based on polymer electrolyte membrane fuel cell', *Sensor. Actuat. B: Chem.* 107, 2005, 812-817.
- [57] C.H. Han, D.W. Hong, S.D. Han, J. Gwak, K.C. Singh, 'Catalytic combustion type hydrogen gas sensor using TiO₂ and UV-LED', *Sensor. Actuat. B: Chem.* 125, 2007, 224-228.
- [58] M. Zhao, J.X. Huang, C.W. Ong, 'Diffusion-controlled H₂sensors composed of Pd-coated highly porous WO₃nanocluster films', *Sens. Actuators B* 191, 2014, 711-718.
- [59] H.G. Na, Y.J. Kwon, H.Y. Cho, S.Y. Kang, T.K. Jung, H.S. Lee, H.W. Kim, 'Improved Sensing Behaviors in Reduced Graphene Oxide Functionalized with Ni(OH)₂



- Nanoparticles', *Journal of nanoscience and nanotechnology* 15, 2015, 9002-9008.
- [60] I. Simon, M. Arndt, 'Thermal and gas-sensing properties of a micromachined thermal conductivity sensor for the detection of hydrogen in automotive applications', *Sensor. Actuat. A: Phys.* 97, 2002, 104-108.
- [61] National Geographic Society. (n.d.). 'Encyclopedic Entry: Sediment. In *National Geographic: Education*', 2011, Retrieved from http://education.nationalgeographic.com/education/encyclopedia/sediment/?ar_a=1, [Accessed: 23- Jun- 2018].
- [62] L. Boon-Brett, J. Bousek, P. Castello, O. Salyk, F. Harskamp, L. Aldea, F. Tinaut, 'Reliability of commercially available hydrogen sensors for detection of hydrogen at critical concentrations: Part I - Testing facility and methodologies', *Int. J. Hydrogen Energ.* 33, 2008, 7648-7657.
- [63] L. Boon-Brett, J. Bousek, P. Moretto, 'Reliability of commercially available hydrogen sensors for detection of hydrogen at critical concentrations: Part II - selected sensor test results', *Int. J. Hydrogen Energ.* 34, 2009, 562-571.
- [64] T. Hubert, L. Boon-Brett, G. Black, U. Banach, 'Hydrogen sensors - a review', *Sens. Actuators B*, 157, 2011, 329-352.
- [65] L. Boon-Brett, J. Bousek, G. Black, P. Moretto, P. Castello, T. Hubert, U. Banach, 'Identifying performance gaps in hydrogen safety sensor technology for automotive and stationary applications', *Int. J. Hydrogen Energ.* 35, 2010, 373-384.
- [66] V.M. Aroutiounian, 'Hydrogen detectors', *Int. Sci. J. Alter. Energ. and Ecolog.* 23, 2005, 21-31.
- [67] H.G. Na, H.Y. Cho, Y.J. Kwon, S.Y. Kang, C. Lee, T.K. Jung, H.S. Lee, H.W. Kim,



'Reduced graphene oxide functionalized with Cu nanoparticles: Fabrication, structure, and sensing properties', *Thin Solid Films* 588, 2015, 11-18.

[68] P. Yasaei, B. Kumar, R. Hantehzadeh, M. Kayyalha, A. Baskin, N. Reppin, C. Wang, R.F. Klie, Y.P. Chen, P. Král, 'Chemical sensing with switchable transport channels in graphene grain boundaries', *Nature communications* 5, 2014

[69] M. Zhao, J. Huang, M. Wong, Y. Tang, C. Ong, 'Versatile computer-controlled system for characterization of gas sensing materials', *Review of scientific instruments* 82, 2011, 105001.

[70] Seiyama, T.; Kagawa, S. 'Study on a Detector for Gaseous Components Using Semiconductive Thin Films', *Analytical chemistry* 38, 1966, 1069.

[71] Madel, M.; Huber, F.; Mueller, R.; Amann, B.; Dickel, M.; Xie, Y.; Thonke, K., 'Persistent conductivity in ZnO nanowires: Influence of oxygen and argon ambient'. *Journal of Applied Physics* 12, 2017, 124301.

[72] M. Cho, I. Park, 'Recent Trends of Light-enhanced Metal Oxide Gas Sensors: Review', *J. Sensor Sci. & Tech.* 25, 2016, 103-109.

[73] Q. Geng, Z. He, X. Chen, W. Dai, X. Wang, 'Gas sensing property of ZnO under visible light irradiation at room temperature', *Sens. Actuators B* 188, 2013, 293– 297.

[74] N. Yamazoe, J. Fuchigami, M Kishikawa, T. Seiyama, 'Interactions of tin oxide surface with O₂', H₂O and H₂, *Surf. Sci.* 86 ,1979, 335-344.

[75] X. Li, X. Li, J. Wang, S. Lin, 'Highly sensitive and selective room-temperature formaldehyde sensors using hollow TiO₂ microspheres', *Sens. Actuators B* 219, 2015, 158-163.

[76] Z. Wang, Y.M. Hu, W. Wang, X. Zhang, B.X. Wang, H.Y. Tian, Y. Wang, J.G.



Guan, H.S. Gu, 'Fast and highly-sensitive hydrogen sensing of Nb₂O₅ nanowires at room temperature', *Int. J. Hydrogen Energy* 37, 2012, 4526–4532.

[77] J.J. Hassan, M.A. Mahdi, C.W. Chin, H. Abu-Hassan, Z. Hassan, 'Room temperature hydrogen gas sensor based on ZnO nanorod arrays grown on aSiO₂/Si substrate via a microwave-assisted chemical solution method', *J. Alloys Compd.* 546, 2013, 107–111.

[78] J.J. Hassan, M.A. Mahdi, C.W. Chin, H. Abu-Hassan, Z. Hassan, 'A high-sensitivity room-temperature hydrogen gas sensor based on oblique and vertical ZnO nanorod arrays', *Sens. Actuators B* 176, 2013, 360–367.

[79] Y. Wang, B. Liu, D. Cai, H. Li, Y. Liu, D. Wang, L. Wang, Q. Li, T. Wang, 'Room-temperature hydrogen sensor based on grain-boundary controlled Pt decorated In₂O₃ nanocubes', *Sens. Actuators B* 201, 2014, 351–359.

[80] C. Xiang, Z. She, Y. Zou, J. Cheng, H. Chu, S. Qiu, H. Zhang, L. Sun, F. Xu, 'A room-temperature hydrogen sensor based on Pd nanoparticles doped TiO₂ nanotubes', *Ceram. Int.* 40, 2014, 16343–16348.

[81] M. Zhao, C.W. Ong, 'Improved H₂-sensing performance of nanocluster-based highly porous tungsten oxide films operating at moderate temperature', *Sens. Actuators B* 174, 2012, 65–73.

[82] S.P. Zhang, T. Lei, D. Li, G.Z. Zhang, C.S. Xie, 'UV light activation of TiO₂ for sensing formaldehyde: how to be sensitive, recovering fast, and humidity less sensitive', *Sens. Actuators B* 202, 2014, 964–970.

[83] N. Barsan, U. Weimar, 'Conduction model of metal oxide gas sensors', *J. Electroceram.* 7, 2001, 143–167.

[84] Hadjiivanov, K., P. Lukinskas, and H. Knözinger, Detection of Reduced Wⁿ⁺ Sites



on $\text{WO}_3\text{-ZrO}_2$ and $\text{Pt/WO}_3\text{-ZrO}_2$ Catalysts by Infrared Spectroscopy of Adsorbed NO . *Catalysis Letters* 82, 2002, 73-77.

[85] G.N. Chaudhari, A.M. Bende, A.B. Bodade, S.S. Patil, V.S. Sapkal, 'Structural and gas sensing properties of nanocrystalline $\text{TiO}_2\text{:WO}_3$ -based hydrogen sensors', *Sens. Actuators B* 115, 2006, 297-302.

[86] E. Ghadiri, A. Irajizad, F. Razi, 'Hydrogen sensing properties of pure and Pd activated WO_3 nanostructured films', *Synth. React. Inorg. Met.* 37, 2007, 453-456.

[87] J.W. Gong, J.R. Sun, Q.F. Chen, 'Micromachined sol-gel carbon nanotube/ SnO_2 nanocomposite hydrogen sensor', *Sens. Actuators B* 130, 2008, 829-835.

[88] S.J. Ippolito, S. Kandasamy, K. Kalantar-zadeh, W. Wlodarski, 'Hydrogen sensing characteristics of WO_3 thin film conductometric sensors activated by Pt and Au catalysts', *Sens. Actuators B* 108, 2005, 154-158

[89] R. Ghasempour, A. Irajizad, 'Hybrid multiwalled carbon nanotubes and trioxide tungsten nanoparticles for hydrogen gas sensing', *J. Phys. D Appl. Phys.* 42, 2009, 165105.

[90] K. Mukherjee, S.B. Majumder, 'Hydrogen sensing characteristics of wet chemical synthesized tailored $\text{Mg}_{0.5}\text{Zn}_{0.5}\text{Fe}_2\text{O}_4$ nanostructures', *Nanotechnology* 21 2010, 255504.

[91] Fondriest Environmental INC., 'Measuring Dissolved Oxygen', 2016. Retrieved from: <https://www.fondriest.com/environmental-measurements/equipment/measuring-water-quality/dissolved-oxygen-sensors-and-methods>. [Accessed: 23- Jun- 2018].